March 2018

Search for long-lived, massive particles decaying into dimuon vertices in pp collisions at 13 TeV with the ATLAS detector at the LHC

Nathan Bernard

SEARCH FOR LONG-LIVED, MASSIVE PARTICLES DECAYING INTO $\mu^+\mu^-$ IN PP COLLISIONS AT $\sqrt{S} = 13$ TeV WITH THE ATLAS DETECTOR AT THE LHC

A Dissertation Presented

by

NATHAN ROGERS BERNARD

Submitted to the Graduate School of the
University of Massachusetts Amherst in partial fulfillment
of the requirements for the degree of

DOCTOR OF PHILOSOPHY

February 2018

Department of Physics

SEARCH FOR LONG-LIVED, MASSIVE PARTICLES DECAYING INTO $\mu^+\mu^-$ IN PP COLLISIONS AT $\sqrt{S} = 13$ TeV WITH THE ATLAS DETECTOR AT THE LHC

A Dissertation Presented

by

NATHAN ROGERS BERNARD

Approved as to style and content by:

Carlo Dallapiccola, Chair

Ben Brau, Member

Michael Ramsey-Musolf, Member

Grant Wilson, Member

Narayanan Menon, Chair
Department of Physics

ACKNOWLEDGMENTS

My advisor Carlo Dallapiccola; my thesis committee; Dan Ventura, Rozmin Daya, Ed Moyse, Nora Pettersson, and Guy Rosin who all contributed to the analysis within ATLAS; our editorial board (EB), particularly Ahmimed Ouraou, as well as the exotics UEH group conveners Emma Torro Pastor and Will Buttinger; Ben Brau and Stephane Willocq, as well as the rest of the UMASS ATLAS group; Max Bellomo, Jochen Meyer, Niels van Eldik, and the ATLAS muon software group; the US DOE for funding the research; my loving wife, Diana Bernard; my parents Bill Bernard, Cherie Bernard-Frobish, and Matt Frobish; my siblings Hannah and Ben Bernard, and the rest of my family; my in-laws, particularly Paul and Tila Ovalle; Salem Al-Mosleh, Ramesh Adhikari, Brian Griffin and all my UMass friends; anyone else I might have forgot...

ABSTRACT

SEARCH FOR LONG-LIVED, MASSIVE PARTICLES DECAYING INTO $\mu^+\mu^-$ IN PP COLLISIONS AT $\sqrt{S} = 13$ TeV WITH THE ATLAS DETECTOR AT THE LHC

FEBRUARY 2018

NATHAN ROGERS BERNARD

B.Sc., UNIVERSITY OF CALIFORNIA LOS ANGELES

Ph.D., UNIVERSITY OF MASSACHUSETTS AMHERST

Directed by: Professor Carlo Dallapiccola

A search for long-lived, massive particles decaying into dimuon pairs, in 32.9 fb^{-1} of data analyzed from the ATLAS detector is presented. Two signal models are considered: GGM SUSY, where the long lived particle mass is between 300-1000 GeV, and the dark photon model, where the Z_D mass is between 20-60 GeV. An excess over the predicted background is observed in the GGM channel, however the angular/kinematic distributions of the excess vertices are consistent with a detector/conditions related issue. A modified selection is used for the GGM channel which increases the signal sensitivity. 95% confidence level (CL) upper limits on the signal cross sections times branching fraction are set as a function of $c\tau$ for both benchmark models. The $c\tau$ limits for the GGM channel extend from 2.57-1050 cm, and the $c\tau$ limit for the Z_D channel extends from 0.32-1572 cm. 95% CL upper limits on the Z_D cross section are also set in the coupling-$c\tau$ plane, for a range of BF($\text{H}\rightarrow \text{Z}_\text{D}\text{Z}_\text{D}$).

TABLE OF CONTENTS

LIST OF TABLES

LIST OF FIGURES

CHAPTER 1

INTRODUCTION

The primary goals of the ATLAS and CMS experiments [1, 2] at the Large Hadron Collider (LHC) are to gain a better understanding of physics at the electroweak scale [3–5]. Not only how well the Standard Model (SM) of particle physics performs under testing, but to search for signs of beyond standard model (BSM) physics. The discovery of a Higgs boson [6, 7] with quantum numbers and couplings to other particles consistent with those predicted by the SM is, at the time of this writing, the crowning achievement of the LHC physics program. While a Higgs boson explains how the masses of the quarks and leptons, as well as gauge bosons, are generated, it also raises questions [8]. What stabilizes the electroweak scale against quantum corrections that would push it to the highest known energy scale, the Planck scale? Is there a natural way of understanding the tuning of the SM parameters?

The most popular class of BSM theories that provide answers to these questions is Supersymmetry (SUSY) [9], an extension of spacetime symmetry, that relates bosons to fermions and vice versa. SUSY is favorable in the particle physics community since many instances naturally contain a dark matter candidate [10], however after Run 1 of the LHC there has been no evidence of SUSY [11, 12]. As a result, there is an increasing emphasis on the exploration of unusual final state signatures that would elude the searches based on the standard algorithms that reconstruct objects such as tracks, jets, muons, electrons, etc.

Long-lived ($c\tau \gtrsim 1$ cm) massive particles (LLPs) that decay to SM particles often have unsual final state signatures and are featured in a number of proposed BSM

models [13, 14]. The mass of the LLP will impact the final state topologies, and so when searching for such models it is useful to break them in to two categories: low and high mass LLPs. Models featuring low mass LLPs include dark photons [14, 15], hidden-valleys [16], and stealth SUSY [17]. Models with high mass LLPs include general gauge mediated SUSY [18], R-parity violating SUSY [19], and split SUSY [20].

The difficulty in searching for LLPs lies with the standard ATLAS tracking algorithms [21, 22]. They assume that particles originate from interactions relatively close to the beamline and make use of this as a constraint in discriminating against combinatoric, cosmic, and beam-related backgrounds. Inner detector (ID) tracks with transverse impact parameter, d_0, larger than about 1 cm are effectively rejected, as displayed in Fig. 1.1 (a). Note that the small but non-zero efficiency for combined muons above 1 cm is due to how the "true" d_0 is calculated. It assumes a straight line extrapolation from the displaced vertex back towards the IP. Furthermore, most analyses consider only those tracks that originate from a reconstructed "primary vertex," as a means to suppress background from multiple pp interactions ("pileup") [23]. Fortunately, muon candidate tracks are reconstructed independently in the muon spectrometer, without imposing the requirement that there be an associated ID track (stand-alone muon (MuSA) tracks). Though track reconstruction in the MS does reject candidates that do not extrapolate back to a region near the IP, there remains significant efficiency even for muons with transverse impact parameters as large as 400 cm, as can be seen in Fig. 1.1(b).

For the purposes of this analysis, an *approximate* classification of particle decays into "prompt," "long lived" (or metastable) and "stable" is as follows, based on the particle's mean proper lifetime, $c\tau$:

- Prompt: $c\tau < 1$ cm ($c\tau < 30$ps for $\beta \sim 1$ particles);
- Long lived: 1 cm $< c\tau <$ 100m;

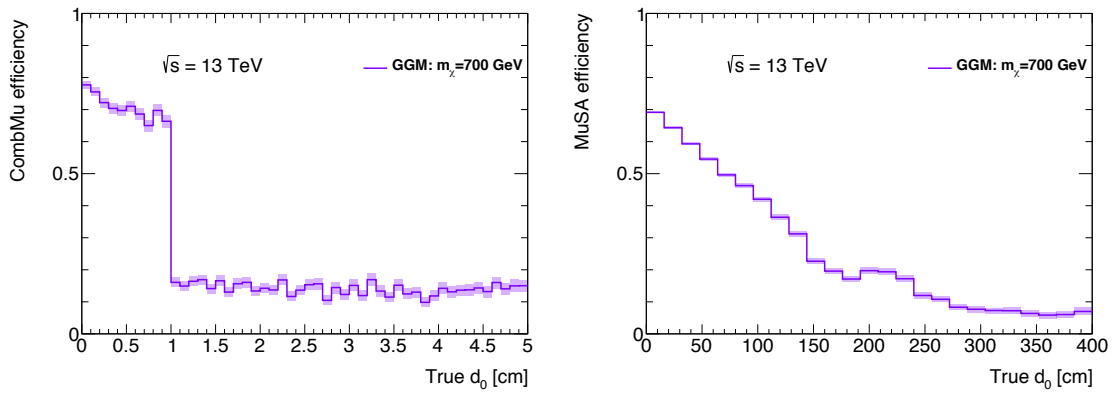

(a) Combined muons (b) Stand-alone muons

Figure 1.1: The distribution of true transverse impact parameter, d_0, for (a) combined muon tracks and (b) stand-alone muon spectrometer tracks, that have been truth-matched to a muon in simulated events. The muons tracks are reconstructed in events with a BSM long-lived neutralinos, $\tilde{\chi}_1^0$ ($m_{\tilde{\chi}_1^0} = 700$ GeV and $c\tau_T = 1$m) decaying to a Z boson (with $Z \to \mu^+\mu^-$) and a gravitino. Note that the non-zero efficiency for combined muons above 1 cm is due to simple analytic calculation of the "truth" d_0. The shaded bands represent the statistical uncertainty only.

- Stable: $c\tau > 100$m.

The categorization of a prompt decay is driven by the standard ID track reconstruction algorithm, which assumes that particles originate from the interaction point (IP) and discards tracks with large d_0, as described above. A stable particle is defined as one that decays predominantly outside of the detector fiducial volume. Generically, a particle decay is non-prompt for one (or, more commonly, a combination) of the following reasons:

- The available phase space for decays is very constrained (e.g. neutrons);
- Small coupling parameters are involved (e.g. weak coupling constant);
- A conserved (or nearly-conserved) quantum number suppresses the decay (e.g. protons, neutrinos).

In most models of BSM physics there are a number of free parameters (masses of particles, coupling parameters, etc.) that influence the lifetimes of the new particle states, according to the schemes described above, with no strong motivation for assuming that all of the particles are either promptly decaying (leading to final states with tracks found by the standard reconstruction software), or very stable (leading to $E_{\mathrm{T}}^{\mathrm{miss}}$ signatures). Particle lifetimes in the SM, for instance, span roughly 66 orders of magnitude.

Members of the ATLAS collaboration have performed numerous searches for LLPs with a wide range of experimental signatures. The SM decay products will primarily feature hadrons, due to the large number of degrees of freedom in the color sector. The displaced jets [24] and multitrack displaced vertex (DV) searches [25] exploit these large hadronic branching fractions to enhance signal sensitivity, however accurate modeling of interactions with detector material are needed. The branching fractions for LLPs to decay to leptonic final states are smaller, but leptonic final states are much cleaner. The displaced lepton-jet [26] and displaced dilepton [25] analyses exploit the minimal background contamination to effectively increase signal sensitivity. All of these searches have used various methods of circumventing the pointing requirements of the nominal ATLAS track reconstruction. The primary method being the reprocessing of raw ATLAS data with looser pointing requirements [27]. Of course this increases the detector acceptance for LLP signals over the nominal reconstruction, however any analysis utilizing the ID will eventually be limited by the physical dimensions of the ID itself.

The unique design of the ATLAS muon detector allows for a very striking and compelling detection of the $\mu^+\mu^- + X$ final state within an unusually large decay volume. An excess of a few events over expected background in a topological multitrack displaced vertex search, for instance, would have to be very carefully scrutinized in order to provide confidence that it constituted a signal of new physics. A handful

of $\mu^+\mu^-$ vertices highly displaced from the IP would, on the other hand, be nearly unexplainable except as evidence of new physics.

1.1 Analysis overview

A search for beyond Standard Model physics in the form of massive ($\gtrsim 15$ GeV), long-lived ($c\tau \gtrsim 1$ cm) particles is described. The search is performed using pp collision data collected by ATLAS at $\sqrt{s} = 13$ TeV in 2016, equivalent to 32.9 fb^{-1}. The essential element of the analysis is the exploitation of the unique capabilities of the ATLAS muon spectrometer (MS) by reconstructing final states that include pairs of oppositely-charged muons originating from a common vertex significantly displaced from the IP. By not requiring that muon candidates be combined with an inner detector track, we successfully reconstruct dimuon vertices nearly all the way out to the inner layer of the MS, as far as 4 (6)m from the IP for the barrel (endcap) region. The analysis strategy consists of selecting events with one or more displaced $\mu^+\mu^-$ vertices and minimal requirements on other aspects of the event (to retain the greatest possible model independence).

In order to maintain high efficiency for finding dimuon vertices displaced from the IP as far out as the inner radius of the muon spectrometer, while also ensuring the best possible resolution on the vertex position and mass, the following techniques (described in detail in Sect. 5) are employed:

Displaced dimuon selection

1. *MS only muons:* Muon spectrometer tracks that are not associated with an ID track (denoted here as "MuSA" tracks) are considered as muon candidates for use in the displaced vertex search. Track quality criteria are employed to ensure that the track parameters are well-measured. The veto of MS tracks that are associated with an MS-ID combined muon is a critical component of

the analysis as otherwise one would be overwhelmed by SM backgrounds that feature prompt muons.

2. *Vertexing:* Pairs of muon candidates with $p_{\mathrm{T}} > 10$ GeV selected in the previous step are passed to a vertexing algorithm that determines the location of the point of closest approach (vertex) of the two muons and its distance from the IP, L_{vtx}.

3. *Statistical analysis:* A simple cut-and-count analysis is performed, whereby the number of events observed in data, after the selection criteria has been applied, is compared with the predicted number of events from background. In the event that a significant excess over background is observed, the dimuon invariant mass distribution and L_{vtx} distribution will be studied in order to determine the mass and lifetime of the state. Otherwise, the CL_S technique will be used to set upper limits on the product of production cross section and dimuon branching fractions for the selection of signal models under consideration.

Triggers

The algorithm described above is a candidate-driven approach to finding suitable dimuon vertices, irrespective of whether or not other tracks originate from the same vertex or of any other activity in the event (number of jets, additional leptons, missing energy, etc.). In this way, we ensure the best possible model independence of the search, as noted above. We are, however, limited by the set of triggers employed to identify and save events of interest [28]. Fortunately, a number of trigger algorithms in the menu exhibit relatively high efficiency for most BSM signal events of interest, without unduly compromising the model independence of the search.

Signal events targeted by this analysis feature muons with large d_0 and moderate to large p_{T}, which in connection to prompt hadronic activity often contribute to significant jet transverse momentum imbalance, $\not{H}_T$. For signal events with *pair*

production of long-lived particles, there may be additional sources of $\not{H}_T$ associated with the other BSM particle (the one not identified with the dimuon pair) – it may e.g. decay far enough away from the IP that the jet reconstruction fails, to some extent, and therefore contributes to the $\not{H}_T$. The triggers used in this analysis are based on either muon tracks reconstructed solely in the MS or on jet transverse momentum imbalance.

Signal Models

Two benchmark models are used to guide decisions on optimal selection criteria and to translate observed yields in data to BSM cross sections, via efficiencies and acceptances obtained from MC-simulated samples. The chosen models represent both a variety of BSM physics possibilities, as well as final state topologies and kinematics, to which the analysis may be sensitive. A brief summary is provided here, and further details can be found in Sect. 6.

- *Dark gauge bosons*: This is a class of Higgs-portal models in which the SM Higgs boson mixes with a new scalar S associated with a "dark" sector. The Higgs boson will then have an exotic decay mode to a pair of dark photons: $H \to Z_\mathrm{D} Z_\mathrm{D}$. Assuming small kinetic mixing between the Z_D and the SM Z, the Z_D will be long-lived and decay into kinematically-allowed pairs of SM particles, including $\mu^+\mu^-$. Events of this type feature only moderately-large $E_\mathrm{T}^\mathrm{miss}$ and little jet activity [14, 15].

- *Gauge-mediated SUSY breaking*: Similar to the SUSY model described above, except that the $\tilde{\chi}_1^0$ is the next-to-lightest SUSY particle (NLSP), and it decays to a very light (sub- GeV) gravitino LSP and a gauge or Higgs boson: $\tilde{\chi}_1^0 \to \tilde{G}\,\gamma/Z/H$. These events feature large $\not{H}_T$, a number of prompt high-p_T jets and a displaced $Z \to \mu^+\mu^-$ vertex [18].

Backgrounds

The dominant sources of background are:

- SM processes with relatively large cross sections that produce isolated muons in the final state (most importantly Drell-Yan and Z + jets production)
- QCD Multijet
- cosmic muons

The methods used to predict the contribution of each background to the analysis are detailed in Sect. 6.

Systematics

The data-driven background prediction techniques used in this analysis reduce the sources of systematic uncertainty in this analysis, however the following sources remain:

- Luminosity
- Pileup reweighting (PRW)
- Trigger and MuSA reconstruction efficiency
- Fake vertices
- ABCD region size

Further description of how each of these systematic uncertainties are evaluated in the analysis are given in Sect. 8. The systematics are used as nuisance parameters in the profile likelihood used for the statistical analysis.

Results

The results of this analysis are given in Sect. 9 and their interpretation in terms of our bench mark models is given in Sect. 10.

CHAPTER 2

THEORY

2.1 Higgs Portal

The Higgs mechanism for spontaneous symmetry breaking was first postulated in 1964 [29–31] as a way of generating mass for the gauge bosons. The mechanism functions as follows [32]:

- Standard mass terms for gauge bosons violate local gauge symmetry and require the gauge bosons be massless.
- One can introduce a complex scalar SU(2) doublet that couples to itself, via the potential $V(\phi) = \mu^2\phi^\dagger\phi + \lambda(\phi^\dagger\phi)^2$, and to gauge bosons and leaves the SM lagrangian invariant under gauge transformations.
- When $\mu^2 > 0$, the state of lowest energy is the vacuum, $\phi = 0$. If $\mu^2 < 0$, however, the higgs picks up a vacuum expectation value (VEV) of $< \phi >= \sqrt{-\frac{\mu^2}{2\lambda}}$, and breaks the global $SU(2)_L \times U(1)_Y$ symmetry down to $U(1)_{EM}$.
- A redefinition of fields can be performed to describe the complex scalar doublet instead as four real scalar fields. Gauge transformations are used to remove the dependence of the langrangian on three of the four components of the higgs field. This is typically described as the fields being "eaten" by the massless gauge bosons, since the transformations result in mass terms for the gauge bosons. Only the W+,W-, and Z fields gain a mass the photon remains massless.

- The result is a model with three massive gauge fields, one massless gauge field, and one real scalar higgs field.

- In the SM left and right handed fermions transform differently under $SU(2)_L$ and $U(1)_Y$, and so gauge invariance doesn't allow for standard mass terms.

- The Higgs mechanism introduces Yukawa couplings between left and right handed fermions and the higgs field, which are interpreted as generating gauge invariant mass terms for fermions.

The 2012 discovery of a SM Higgs boson at the LHC by the ATLAS and CMS experiments [6, 7] opened a whole new sector of the SM to study. The most exciting aspect of the new Higgs sector, is whether it couples to BSM physics in a directly observable manner.

2.1.1 Dark gauge bosons

A number of BSM theories feature a "hidden" or "dark" sector of matter that is SM-neutral but may nevertheless interact, weakly, with SM matter via coupling to the Higgs field. These are so-called "Higgs portal"[33] models that address the dark matter problem, electroweak baryogenesis, etc. The model we consider, relevant for this analysis, is one in which there exists a $U(1)_{\mathrm{D}}$ symmetry in the dark sector, and the dark vector gauge boson Z_{D}, often called a "dark photon," is given mass via a singlet scalar field S that breaks the symmetry and is analogous to the Higgs field in the visible, SM sector [14, 15]. The BSM terms in the Lagrangian density are as follows:

$$L_{\mathrm{BSM}} = -\frac{1}{4}\hat{Z}_{\mathrm{D}\,\mu\nu}\, Z_{\mathrm{D}}^{\mu\nu} + \frac{1}{2}\frac{\epsilon}{\cos\theta_W}\hat{B}_{\mu\nu}\,\hat{Z}_{\mathrm{D}}^{\mu\nu} - \mu_{\mathrm{D}}^2|S|^2 + \lambda_{\mathrm{D}}|S|^4 + \zeta|S|^2|H|^2\,. \qquad (2.1)$$

Included are both a Higgs portal (last term above) and hypercharge portal (second term above), providing for kinetic Z-Z_{D} mixing (i.e. mixing between $U(1)_Y$ and

$U(1)_{\mathrm{D}}$) and H-S mixing, regulated by the small coupling parameters ϵ and ζ, respectively. There are two vector-boson mass eigenstates, one that is dominantly Z_{D} and another that is dominantly SM Z, as well as two scalar mass eigenstates, one that is dominantly S and another that is dominantly H. For simplicity, the physical (mass) states will be denoted H, S, Z and Z_{D}.

Considering the scenario where the singlet scalar S is heavier than the SM H, which means that the process $H \to SS$ is kinematically forbidden, and Z_{D} is lighter than half the H mass, events with a displaced dimuon vertex signature would be observable in experiments at the LHC, via the process given in Fig. 2.1, wherein the Z_{D} are produced on-shell and decay to SM fermions due to their induced couplings to the electroweak current. A small value of ϵ ($\lesssim 10^{-5}$) would result in a long-lived Z_{D} state, and for even small, $\mathcal{O}(1\%)$, exotic branching fractions for $H \to Z_{\mathrm{D}} Z_{\mathrm{D}}$, not yet ruled out by constraints from Higgs couplings fits, enough events would be produced in Run 2 of the LHC to be observable:

$$\Gamma\left(H \to Z_D Z_D\right) = \frac{\zeta^2 \sqrt{M_H^2 - 4M_{Z_D}^2}\left(-4M_H^2 M_{Z_D}^2 + 12M_{Z_D}^4 + M_H^4\right)}{64\pi\lambda\left(M_H^2 - M_S^2\right)^2} \tag{2.2}$$

$$\Gamma\left(Z_D \to f\bar{f}\right) = \frac{N_c}{24\pi M_{Z_D}}\sqrt{1 - \frac{4m_f^2}{M_{Z_D}^2}}\left(M_{Z_D}^2\left(g_L^2 + g_R^2\right) - m_f^2\left(-6g_L g_R + g_L^2 + g_R^2\right)\right) \tag{2.3}$$

$$g_{L,R} = g_{Z_D f_{L,R} \bar{f}_{L,R}} = \frac{\epsilon g'\left(c_w^2 M_Z^2\left(T3 + Y\right) - Y M_{Z_D}^2\right)}{c_w\left(M_Z^2 - M_{Z_D}^2\right)} \tag{2.4}$$

$$\mathrm{BF}\left(H \to Z_\mathrm{D} Z_\mathrm{D}\right) \propto \zeta \frac{m_H^2}{|m_S^2 - m_H^2|} \tag{2.5}$$

$$c\tau_{Z_D} = \frac{\hbar c}{\Gamma_{Z_D}} = \frac{M_{Z_D}}{\epsilon^2} f\left(M_{Z_D}\right) \tag{2.6}$$

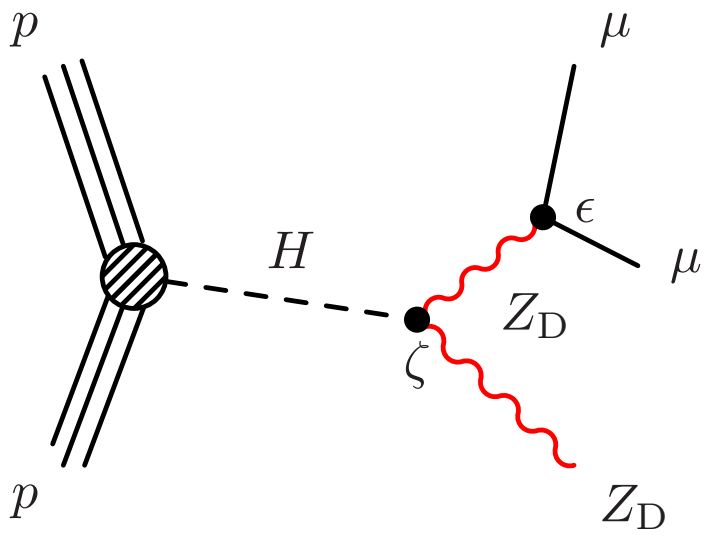

Figure 2.1: Feynman diagram for the dark sector model considered as possible signal in this analysis.

2.2 Supersymmetry

The coupling of the Higgs boson to SM fields explains how particle masses are generated, but it also raises questions [9]. In quantum field theory (QFT) the couplings between fields receive higher order corrections due to virtual interactions. For example, the correction to m_H^2 from a loop containing a Dirac fermion f with mass m_f will be:

$$\Delta m_H^2 = -\frac{|\lambda_f|^2}{8\pi^2}\Lambda_{UV}^2 + ... \tag{2.7}$$

Where λ_f is the Yukawa coupling and Λ_{UV} is the ultraviolet momentum cutoff used to regulate the loop integral. If the ultraviolet cutoff is at the planck scale, M_P, then the quantum corrections to m_H^2 will be 30 orders of magnitude larger than the mass itself. One possibility is that there is a whole sector of new particles that also couple to the Higgs and whose contributions to Δm_H^2 cancel those of the SM fermions. Systematic cancellations often occur in physics as the result of symmetry. The problem at hand requires symmetry between fermions and bosons because of the relative minus sign between fermion and boson loop contributions to Δm_H^2. Such a symmmetry is called "supersymmetry" and its study has resulted in a strikingly large number of BSM models over the last 50 years.

2.2.1 General Gauge-mediated (GGM) SUSY

In RP-conserving SUSY models where gauge interactions mediate the breaking of the supersymmetry, the gravitino acquires its mass from a "super-Higgs" mechanism [34] and is very light ($m_{\tilde{G}}\ell^+\ell^-1$ GeV), as indicated by the formula:

$$m_{\tilde{G}} = \frac{F_0}{\sqrt{3}M_{\rm Pl}} = \left(\frac{\sqrt{F_0}}{100\ \text{TeV}}\right)^2 \cdot 2.4\ \text{eV}\,, \tag{2.8}$$

where $\sqrt{F_0}$ is the fundamental scale of supersymmetry breaking (typically $\gtrsim 100$ TeV) and $M_{\rm Pl}$ is the gravitational scale (the Planck mass). Hence, the gravitino is the

LSP. All supersymmetric particles decay promptly through cascades leading to the NLSP, which then decays into the LSP gravitino via an interaction with a $1/F_0$ suppression. The NLSP, depending on model choices, is either the lightest slepton or lightest neutralino, $\tilde{\chi}_1^0$. For the latter case, described in more detail in [18], if $\tilde{\chi}_1^0$ has a signficant Wino or Higgsino component the branching fraction for the decay $\tilde{\chi}_1^0 \to Z\tilde{G}$ can be $\mathcal{O}(1)$. For example, for $\tan\beta = 2$ and $\mu > 0$, the branching fraction is approximately 90%. The lifetime of $\tilde{\chi}_1^0$ is determined by F_0 (or, alternatively, by $m_{\tilde{G}}$, according to Eqn. 2.8) and $m_{\tilde{\chi}_1^0}$,

$$c\tau_{\tilde{\chi}_1^0} = \frac{1}{\Gamma_{\tilde{\chi}_1^0}} = \frac{16\pi F_0^2}{m_{\tilde{\chi}_1^0}^5} \approx \left(\frac{100\text{ GeV}}{m_{\tilde{\chi}_1^0}}\right)^5 \left(\frac{\sqrt{F_0}}{300\text{ TeV}}\right)^4 \cdot 10\text{mm}\,, \tag{2.9}$$

and hence $\tilde{\chi}_1^0$ is long-lived (i.e. non-prompt) for natural values of the parameters.

The Feynman diagram for pair production of gluinos, followed by a cascade of decays leading to $\tilde{\chi}_1^0 \to Z\tilde{G}$ is shown in Fig. 2.2 (note that a simplified model is used whereby the cascade of decays of SUSY particles is reduced to a single vertex: $\tilde{g} \to qq'\tilde{\chi}_1^0$).

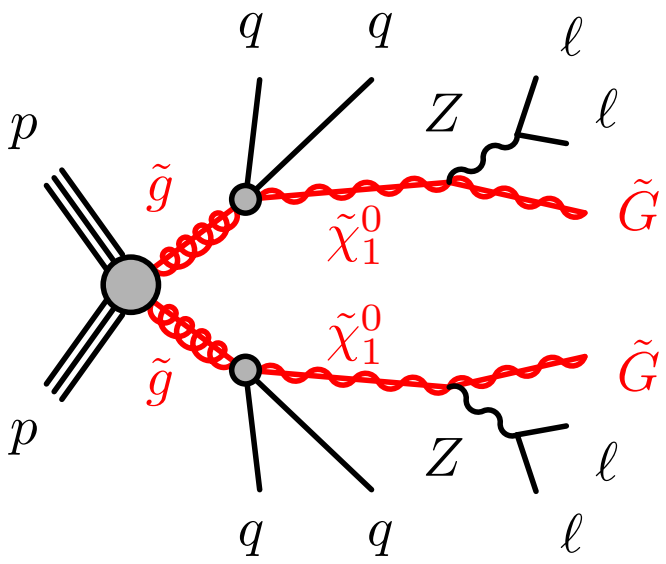

Figure 2.2: Feynman diagram for the GGM SUSY model considered as a possible signal in this analysis.

CHAPTER 3

DETECTOR

The ATLAS (A toroidal LHC ApparatuS) Detector is a general purpose particle detector located at CERN's Large Hadron Collider (LHC) [35]. It is the largest of the seven detectors located at the LHC, measuring roughly 46 meters in length, 25 meters in diameter, and weighing about 7,000 tons. A more detailed description of the detector is available in [1, 36–39].

3.1 Coordinate system

The ATLAS coordinate system has its origin at the nominal interaction point, which is located at the center of the detector. The x-axis points towards the center of the LHC ring, and the y-axis points upward, normal to the plane of the LHC ring. A right handed coordinate system, the z-axis points parallel to the beamline in the anti-clockwise direction (w.r.t. LHC ring).

Cylindrical coordinates are used to describe the detector given its cylindrical shape. The radial and azimuthal (ϕ) directions are defined in the x-y plane with the azimuthal angle originating from the x-axis and increasing clockwise w.r.t. the positive z direction.

Physics analyses often assume particles originate from the IP, and as a result only require two angles to describe their location within the detector. The azimuthal angle is the same as in the cylindrical parameterization, however instead of the typical polar angle (θ) formed w.r.t. the positive z-axis, pseudorapdity is used for the second

coordinate. Pseudorapidity is defined as $\eta = -\log(\tan(\frac{\theta}{2}))$. The choice of η over θ is due to particle multiplicity being approximately constant as a function of η.

The described analysis studies particles not originating from the IP and therefore typically requires coordinate transformations in order to make comparisons between objects.

3.2 Inner detector

The Inner detector (ID) [40, 41] surrounds the beampipe and is the first set of detectors particles traverse leaving the interaction point (IP). The layout of the ID is shown in Fig. 3.1, profiled in both r and z.

A 2 Tesla solenoid magnet [42] encases the ID and delivers a field along the z-axis of the ATLAS coordinate system. The magnetic field causes charged particles to travel in helical trajectories whose curvature depend on the particles momentum. By recording the trajectory of charged particles using the ID, their momentum can be determined. Following is a description of the detector technologies used in the ID.

3.2.1 pixel detector

The pixel detector [43, 44] is located closest to the beam pipe, and therefore needs to be resilient against radiation with a fine enough granularity to distinguish the large flux of traversing particles. Semiconductor pixels are the only technology available that is capable of meeting these needs. Pixels are layered onto rectangular modules which are then stacked paralell to the beampipe, staved in the azimuthal direction. Each module holds 46,080 of the 50 μm by 400 μm pixels. There are four layers of pixel modules in the radial direction and three disks of modules in the z direction (on each side of the IP). The inner most radial cylinder is called the Insertable B-Layer (IBL) [45] and was installed in 2014 to improve the granularity of the pixel system.

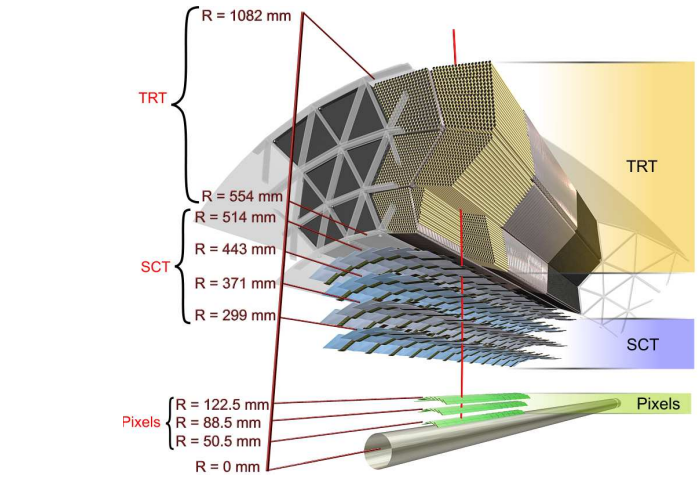

(a)

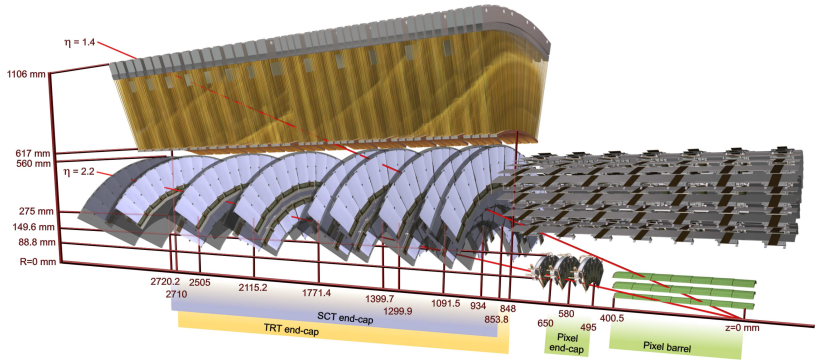

(b)

Figure 3.1: The layout of the inner tracking system profiled in (a) r and (b) z. Note: the diagrams do not show the Insertable B Layer (IBL) which is a fourth layer of pixel detector that sits closest to the beam pipe.

3.2.2 semiconductor tracker (SCT)

The SCT [46–48] also uses semiconductor (silicon) to detect charged particles, with a coarser granularity than the pixel detector. There are four layers of SCT in the radial direction and nine disks of modules in the z direction (on each side of the IP).

3.2.3 transition radiation tracker (TRT)

The TRT [49–51] consists of Polyimide drift tubes of 4 mm diameter. The tubes are 144 cm in the barrel and 37 cm in the end-caps. A Xe-based gas mixture is

used for the TRT. The tubes are packed into three radial sections and twenty endcap sections (on each side of the IP).

3.3 Calorimetry

The calorimetry of the ATLAS detector [52] surrounds the ID and is used to measure of the energy of traversing particles. The layout is shown in Fig. 3.2.

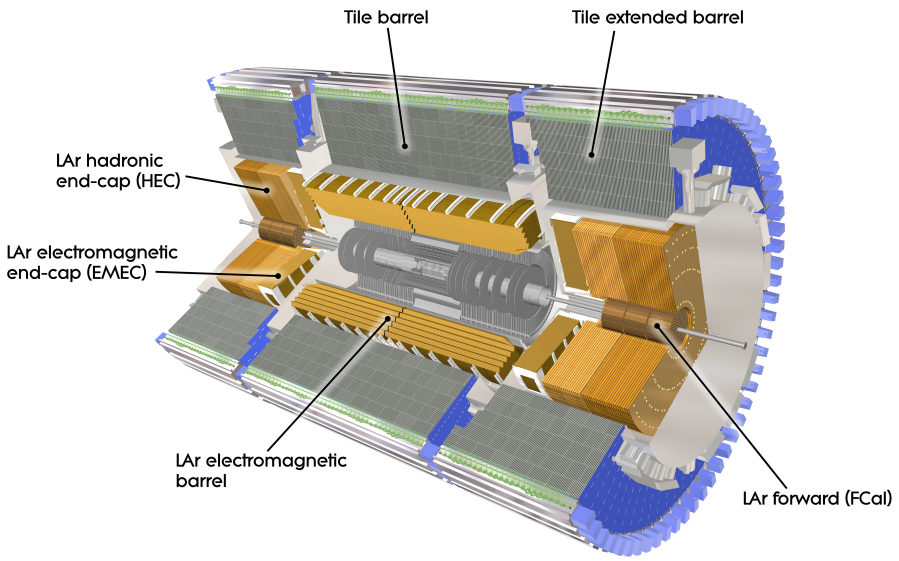

(a)

Figure 3.2: The layout of the ATLAS calorimetry, including both the inner electromagnetic component (yellow) and the outer hadronic component (gray).

Calorimeters function by interleaving absorbing and sensing layers. The absorbing layer is made of dense material that induces showering of the incident particle, while the sensing layers are used to measure the energy profile of the shower as it develops. The material used for the abosrbing layer has a characteristic radiation length which determines how much energy incident particles lose per unit depth into the calorimeter. The choice of abosrbing and sensing material as well as number of layers of each is determined from the expected energy spectra of particles arising from

LHC collisions, i.e. knowing how many radiation lengths the calorimeter must be to contain the vast majority of showers.

3.3.1 Electromagnetic

The electromagnetic calorimeter (ECAL) [53] is used for measuring the energy of incident electrons/positrons and photons. It has an accordian geometry to provide full coverage in the azimutal angle. The absorbing material is lead, and the sensing material liquid argon (LAr). LAr is used for its intrinsic linear behavior and radiation-hardness, as well as the stability of response over time. Using LAr however requires that the calorimeter be housed within a cryostat to keep the detector sufficiently cool. Three cryostats are needed: one to house the barrel ECAL, and one for each of the endcap ECAL systems. The endcap cryostats also hold components of the HCAL system described in the next section.

3.3.2 Hadronic

The hadronic calorimeter (HCAL) [54] is used for the measuring the energy of incident hadronic particles ranging from baryons (i.e. protons/neutrons) to mesons (pions/kaons). The absorbing and sensing materials are different for the various components of the HCAL. The barrel uses steel for absorber and scintillator tiles for the sensing material. This is broken into three sections, one central, and one "extended barrel" section per endcap. The Hadronic endcap calorimeter (HEC) is made of copper/LAr and the forward calorimeter (FCal) of copper-tungsten/LAr. Both of these components are mounted inside the endcap cryostats and extend the HCAL pseudorapidity coverage to 4.9.

3.4 Muon spectrometer

The Muon spectrometer (MS) [55] is the outermost system of the ATLAS detector. The MS tracks charged particles traversing its volume similar to the ID however with

coaser granularity. The primary purpose of the MS is to identify muons. Since muons are much more massive than electrons they do not shower inside calorimeters, and will therefore pass through with minimal energy loss (roughly 3 GeV on average). The granularity of the ID provides superior momentum measurements, however associating MS measurements with ID tracks allows analyzers to identify ID tracks as originating from a muon. In order to measure the momentum of charged particles a magnetic field is required. The MS field is supplied by three superconducting toridal magnets (one in the barrel and one in each endcap) [56, 57]. The magnets are each 4 T and provide a field in the azimutal direction (and hence bending in the r-z plane). There are two main classes of detector used in the MS, precision chambers, named for their precision in bending plane, and trigger chambers, used for triggering and providing reliable *phi* measurements. The MS consists of three layers (stations) in the barrel and three in the endcap, each containing a mixture of the two classes of MS detector. The r-z profile of the MS is shown in Fig. 3.3.

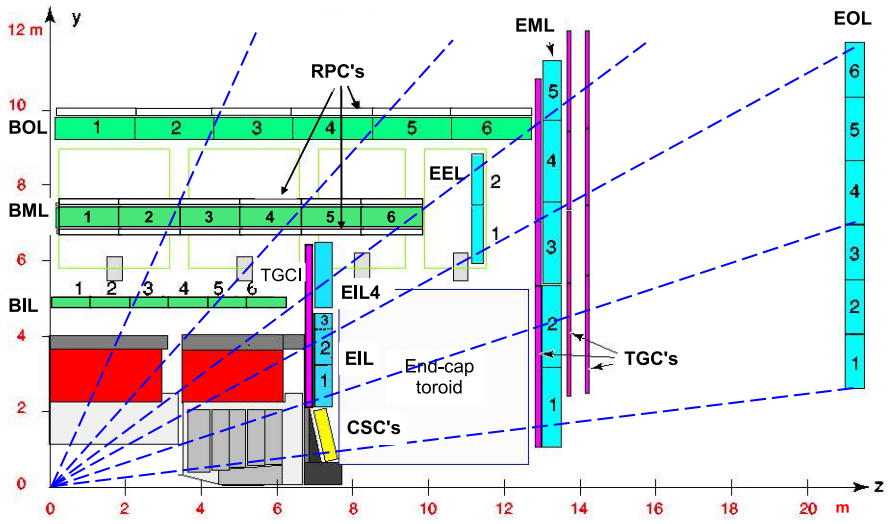

(a)

Figure 3.3: The r-z profile of the ATLAS muon system showing the three barrel stations in green and the three endcap stations in cyan.

3.4.1 Precision chambers

The primary precision chamber is the monitored drift tube (MDT) [58]. MDTs are roughly 3 cm in diameter and filled with an $ArCO_2$ gas mixture. The cross section of an MDT tube is shown in Fig. 3.4.

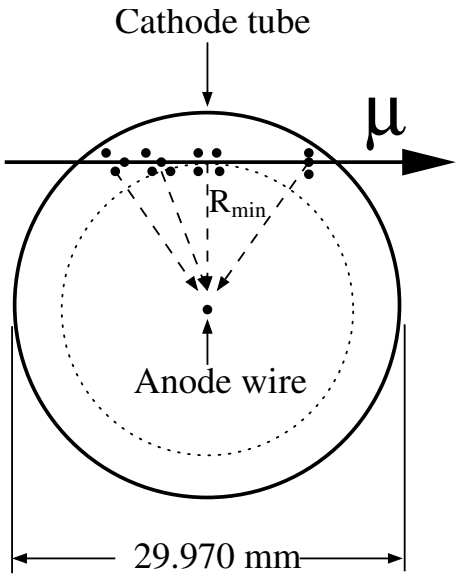

(a)

Figure 3.4: Cross section of MDT tube.

The relation between the minimum radius of a traversing particle, and the drift time of electrons towards the anode wire is refered to as the R-T relation and provides a very precise radial measurement of where the particle passed through the tube (hence precision chambers). The MDT tubes are used in all three stations of both the barrel and endcap MS systems. In both cases the tubes are oriented with the tube length along the azimuthal direction. This orientation allows for precise tracking in the bending plane, while in the azimuthal direction the tracking resolution is only as good as the tube length.

Cathode strip chambers (CSCs) [59] are the other type of precision tracking chamber used in the MS. The high track occupancy in the forward region ($|\eta| > 2$) is not

suitable for the MDT chambers. The CSC can handle the higher rate as well as provide precision measurements compable to the MDT technology.

3.4.2 Trigger chambers

The Resistive plate chamber (RPC) [60] and thin gap chamber (TGC) [61] technologies are used for muon triggering in the barrel and endcap respectively. The bending of particles in a magnetic field is inversely proportional to their total momentum. This means that for a fixed p_{T} the bending of a particle is dependent on *eta*. To maintain consistent p_{T}-resolution in both the barrel and endcap different technologies must be used.

The barrel has three trigger layers. Two on the middle station and one on the outer station. The two layers in the middle station are used for the low p_{T} trigger, while the large lever arm of the third layer on the outer station is used for the high p_{T} trigger. All three layers are positioned inside the barrel toroid's field. The RPC is a gaseous parallel electrode-plate detector. Each RPC layer has two indepedent detector layers measuring both η and ϕ, giving a total of six (η, ϕ) measurements for each track crossing all three MS barrel stations.

The endcap has four trigger layers. Three on the middle station and one on the inner station. The two closest layers in the middle station are used for the low p_{T} trigger, while the two furthest layers in the middle station are used for the high p_{T} trigger. All four layers are positioned outside of the endcap toroid's field. The TGC is a gaseous multi-wire proportional detector with strips and wires oriented perpendicular to one another in the local plane of the chamber. The strips measure the azimuthal coordinate while the wires measure the radial coordinate. Each TGC layer is considered a doublet or triplet depending on whether it has two or three layers of strips/wires. There is one triplet in the middle station and two doublets. The inner station's trigger layer holds a doublet.

3.5 Trigger

The ATLAS trigger system [62] has two main components called the Level 1 (L1) trigger and Higher level trigger (HLT). The L1 trigger is hardware based while the HLT is completely software based. An diagram of the ATLAS trigger logic is shown in Fig. 3.5.

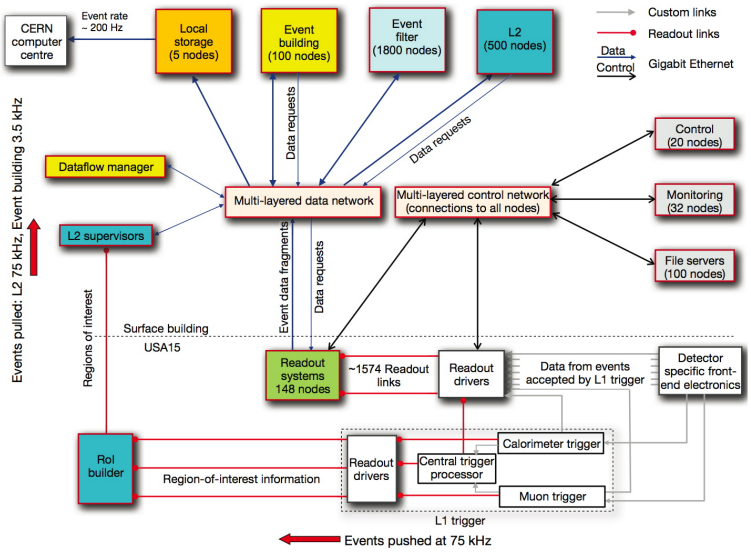

(a)

Figure 3.5: Diagram of the ATLAS trigger logic.

The L1 trigger can handle an accept rate of 75 kHz and processes reduced-granularity information from the MS (muons) and calorimetry (electron,photon,jets,τ,$E_{\mathrm{T}}^{\mathrm{miss}}$).

The HLT reduces the event rate to 200 Hz and utilizes the full granularity of the MS and calorimetry as well as ID data. The HLT trigger objects are similar (and in some cases identical) to the physics objects reconstructed by the nominal ATLAS offline reconstruction software.

CHAPTER 4

DATA AND MONTE CARLO SIMULATION SAMPLES

4.1 Data

Proton-proton collision data collected during 2016, in Run 2 of the LHC, at $\sqrt{s} = 13$ TeV, were analyzed. The requirement that the data were collected during stable beam conditions, and that all relevant detector components were sufficiently functional, results in a total integrated luminosity of 32.9 fb^{-1} for the analyzed sample. The uncertainty on the integrated luminosity is 2.2%. It is derived, following a methodology similar to that detailed in [63], from a preliminary calibration of the luminsoity scale using x-y beam-separation scans performed in May 2016. Events are required to contain at least one reconstructed pp collision vertex candidate with at least two associated ID tracks, each with $p_{\mathrm{T}} > 400$ MeV. The vertex with the largest sum of p_{T}^2 of tracks is considered the primary vertex.

4.2 MC-simulated samples

All simulated samples were processed through the full ATLAS detector simulation [64] based on Geant4 [65]. Multiple overlaid pp collisions are simulated with the soft QCD processes of Pythia 8.186 [66] using tune A2 [67] and the MSTW2008LO PDF set[68]. MC simulations are then reweighted so that the distribution of the average number of interactions per bunch crossing matches what is found in data. MC simulated samples from the two benchmark signal models considered in this analysis are used to tune selection criteria and to evaluate signal efficiencies for use in converting signal yields into cross sections.

4.2.1 Signal samples

Signal events for both benchmark models are generated with MadGraph5_aMC@NLO [69] using the NNPDF23LO PDF set [68] and Pythia8 [66] for parton showering and hadronization. The EvtGen generator [70] is used for weak decays of heavy mesons. The hadronization and underlying-event parameters were set according to the A14 tune [67]. The signal samples are normalized to their predicted cross sections times branching ratio.

A total of 10 signal samples have been produced for the Z_D model with Z_{D} masses and lifetimes taking on the values given in Tab. 4.1. A total of 6 signal samples have been produced for the GGM SUSY model with $m_{\tilde{g}} = 1.1$ TeV and $\tilde{\chi}_1^0$ masses and lifetimes taking on the values given in Tab. 4.2.

$m_{Z_{\mathrm{D}}}$ [GeV]	$c\tau_{Z_{\mathrm{D}}}$ [m]	BF $(Z_{\mathrm{D}} \to \mu^+\mu^-)$	$\sigma \times$ BF [fb]	$\#dimuonvtx$
20	0.5	0.1475	1300.36	>= 1
20	0.5	0.1475	95.90	2
40	0.5	0.1370	1207.79	>= 1
40	0.5	0.1370	82.73	2
40	5	0.1370	1207.79	>= 1
40	5	0.1370	82.73	2
60	0.5	0.1066	939.79	>= 1
60	0.5	0.1066	50.09	2
60	5	0.1066	939.79	>= 1
60	5	0.1066	50.09	2

Table 4.1: MC signal samples for the dark sector interpretation. For all samples, $m_S = 300$ GeV, $\sigma\,(pp \to H) = 44080$ fb, BF $(H \to Z_{\mathrm{D}} Z_{\mathrm{D}}) = 0.10$.

4.2.2 SM background samples

Many of the variables used in selecting vertices are tracking based and difficult to simulate which leads to disagreement between data and MC simulation. For this reason MC simulations are used sparingly in this analysis, and the background is predicted from data-driven techniques. When comparisons are made, the MC simu-

$m_{\tilde{\chi}_1^0}$ [GeV]	$c\tau_{\tilde{\chi}_1^0}$ [m]	$\sigma \times$ BF [fb]
300	1	11.12
300	5	11.12
700	1	11.12
700	5	11.12
1000	1	11.12
1000	5	11.12

Table 4.2: MC signal samples for the GGM SUSY interpretation. For a given $m_{\tilde{\chi}_1^0}$, the gravitino mass is chosen to give the desired lifetime. For all samples, $m_{\tilde{g}} = 1100$ GeV, $\sigma\left(pp \to \tilde{g}\tilde{g}\right) = 163.5$ fb, BF $\left(\tilde{\chi}_1^0 \to Z\tilde{G}\right) = 1.0$, BF $\left(Z \to \mu\mu\right) = 0.034$

lations are normalized to data as described in App. B. The MC generators [71, 72], hadronization and showering software packages [66, 73], underlying event simulation [67], choice of PDF [68], cross section and effective integrated luminosity L_{int} are given in Tab. 4.3 for all the samples considered in this analysis.

Sample	DSID	MC Generator	Hadronization and Showering	tune/PDF	Filter	σ_{prod} [pb]	$\mathcal{L}_{\text{int}}$ [fb^{-1}]
Z+jets	361107	Powheg	Pythia8	AZNLOCTEQ6L1	$Z \to \mu\mu$	1950.63	19.28
DY	361666	Powheg	Pythia8	AZNLOCTEQ6L1	$DY \to \mu\mu$; 6 GeV $< m_{ll} <$ 10 GeV	717.45	9.72
DY	361667	Powheg	Pythia8	AZNLOCTEQ6L1	$DY \to \mu\mu$; 10 GeV $< m_{ll} <$ 60 GeV	1763.35	5.98
$t\bar{t}$	410000	Powheg	Pythia8	P2012	semileptonic	451.69	131.95
W+jets	361101	Powheg	Pythia8	AZNLOCTEQ6L1	$W^+ \to \mu\nu$	11500.91	2.59
W+jets	361104	Powheg	Pythia8	AZNLOCTEQ6L1	$W^- \to \mu\nu$	8579.0	2.32
ZZ	361603	Powheg	Pythia8	CT10/AZNLOCTEQ6L1	$ZZ \to llll$	1.2673	3140.53
ZZ	361604	Powheg	Pythia8	CT10/AZNLOCTEQ6L1	$ZZ \to vvll$	0.918	1083.94
WW	361600	Powheg	Pythia8	CT10/AZNLOCTEQ6L1	$WW \to lvlv$	10.64	558.01
WZ	361601	Powheg	Pythia8	CT10/AZNLOCTEQ6L1	$WZ \to lvll$	4.51	1084.07
single top	410011	Powheg	Pythia	P2012	leptonic; t channel; t	44.15	114.31
single top	410012	Powheg	Pythia	P2012	leptonic; t channel; $\bar{t}$	26.28	193.96
single top	410015	Powheg	Pythia	P2012	leptonic; wt channel; t	3.78	279.06
single top	410016	Powheg	Pythia	P2012	leptonic; wt channel; $\bar{t}$	3.78	279.22
single top	410025	Powheg	Pythia	P2012	leptonic; s channel; t	2.06	487.4
single top	410026	Powheg	Pythia	P2012	leptonic; s channel; $\bar{t}$	1.29	792.71
Upsilon	424102	Pythia8B	–	A14/CTEQ6L1	$\Upsilon(1S) \to \mu\mu$; $\mu\ p_T > 4$ GeV	–	–
Upsilon	424105	Pythia8B	–	A14/CTEQ6L1	$\Upsilon(2S) \to \mu\mu$; $\mu\ p_T > 4$ GeV	–	–
Upsilon	424106	Pythia8B	–	A14/CTEQ6L1	$\Upsilon(3S) \to \mu\mu$; $\mu\ p_T > 4$ GeV	–	–
QCD Multijet	427000	Pythia8	–	A14NNPDF23LO	μ filter	–	–
DY	361476	Sherpa	–	CT10	$DY \to \mu\mu$; 10 GeV $< m_{ll} <$ 40 GeV	–	–

Table 4.3: The MC generators, hadronization and showering software package, underlying event simulation, PDF sets, cross section σ_{prod} and effective integrated luminosity $\mathcal{L}_{\text{int}}$ used for the nominal simulated samples described in this document.

4.3 Object Reconstruction

Reconstruction is the process of taking the raw data collected by the various subsystems of the ATLAS detector and constructing physics objects (i.e. muons, jets, photons...) to be used by analyzers. Physics objects are formed by either connecting hits together in one of the tracking systems to form a particle trajectory, or clustering nearby energy deposits together in the calorimeters.

4.3.1 Tracking

The presence of a non-uniform magnetic field throughout the volume of the ATLAS geometry [74] requires a localized parameterization of particle trajectories. The perigee parameterization is defined by $(d_0, z_0, \phi, \theta, \frac{q}{|P|})$, where d_0 is the transverse impact parameter, z_0 is the longitudinal impact parameter, ϕ and θ are the typical spherical coordinates given at the perigee point, and finally $\frac{q}{|P|}$ holds the charge and momentum information. As a local description these 5 track parameters (TPs) describing the perigee point must always be given w.r.t. a reference point (v_x, v_y, v_z). That reference point is typically near the IP, however depending on where knowledge of the particles trajectory is required can be anywhere. A Runge-Kutta propagator [75] is used to find TPs at different points along a given particle trajectory. A cartoon describing the TPs is given in Fig. 4.1.

For each set of TPs there is a corresponding 5×5 covariance matrix that describes the uncertainties of the TPs. When TPs are given for different locations along a particle trajectory the uncertainties must be propagated using the jacobian of the coordinate transformation as shown below:

$$C_f = J_{fi}^T \, C_i \, J_{fi} \tag{4.1}$$

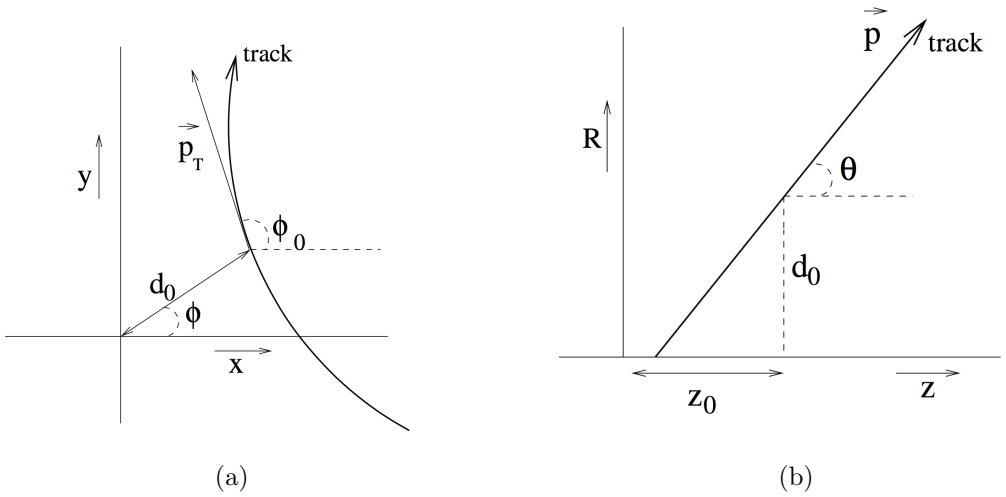

(a) (b)

Figure 4.1: Illustration of the perigee parameterization in both the (a) x-y and (b) r-z planes.

4.3.1.1 Inner detector

The primary track finding scheme within the ID starts near the IP and moves outward. Track seeds are formed using hits from the first few layers of silicon. The Kalman filtering technique [76] is used to add hits to the initial seed in an iterative process. The seed TPs are propagated to the next layer of detectors where hits near the expected position of the extrapolated TP are combined with the seed to form a new set of TPs. The technique is repeated through all layers of the silicon.

The final TP are then extrapolated through the TRT where hits close to the trajectory are grouped together. All hits associated with the trajectory, including silicon and TRT, are fit using the ATLAS global χ^2 fitter [77] to give an ID track.

Many of the track candidates will share hits or be incomplete. A scoring mechanism is used to rank the track candidates, and remove ambiguity that might exist between candidates. More information about the performance of the ID during Run 2 can be found here [78].

4.3.1.2 Muon spectrometer

The Muon reconstruction chain starts by grouping patterns of hits within each MS station. The hits are then fit to a "segment" within the given station. Another stage of pattern recognition then groups segments in different MS stations together. The collection of hits in all the grouped segments are fit to a track using the ATLAS global χ^2 fitter [77]. The track is defined using the perigee parameterization w.r.t. a position in the inner station of the MS.

These tracks are then extrapolated back toward the IP [79], where the fitted track parameters (TPs) are compared with the TPs of inner detector (ID) tracks. If a compatible ID track is found, the hits in the MS and ID tracks are refit to form a combined muon track, again with the global χ^2 fitter. Muons reconstructed in this way have an author of muId [80]. If the refit fails, a statistical combination of the separate MS and ID track fits is attempted. The muons reconstructed from a statistical combination have an author of STACO [81]. The match χ^2 distributions for both muId and STACO combined muons are given in Fig. 4.2. The STACO algorithm parameters are set extremely loose; as can be seen in the match χ^2 distribution. For this reason combined muons of author STACO are not used in computing the ΔR(combMu,MuSA) quantity as described in Sect. 5.1.

In addition to these two types of combined muons the muon reconstruction chain creates segment-tagged and calo-tagged muons [80], in which an ID track is matched to a MS segment (i.e. a fit of hits in one particular station of the MS) or a calo-cluster consistant with muon energy deposition, respectively. These "tagged" combined muons recover inefficiency in the MS system, however our analysis is only concerned with combined muons overlapping with MuSA tracks. Therefore, the tagged class of combined muons are not considered in the analysis. An illustration of the various types of muon objects is displayed in Fig. 4.3. A more detailed review of the muon reconstruction chain is given in [82].

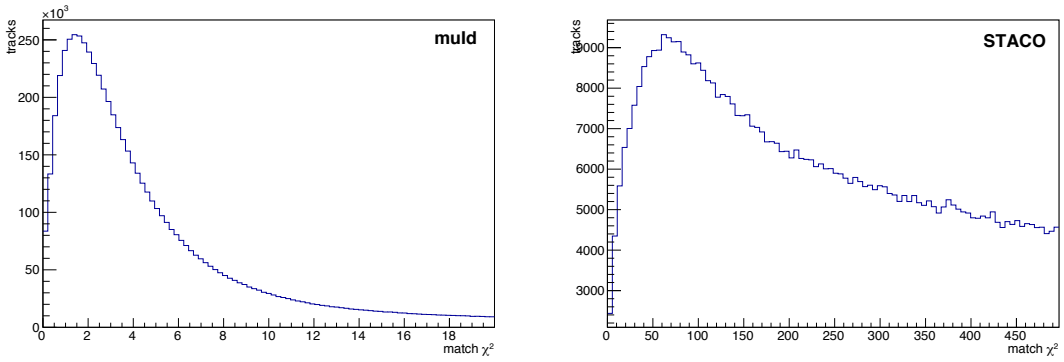

(a) (b)

Figure 4.2: Match χ^2 distributions for combined muon tracks reconstructed with the (a) muId and (b) STACO algorithms. Note the difference in horizontal axis scales for the two distributions.

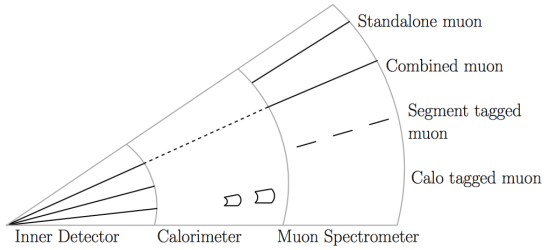

(a)

Figure 4.3: Illustration of the type of objects produced by the muon reconstruction chain.

4.3.2 Clustering

The calorimeters are used for measuring the energy of traversing particles. Each calorimeter subsystem is divided into cells. The anti-kt [83] algorithm is used to form clusters of nearby active cells that are associated to physics objects (electrons,photons,jets,taus). Jets are the only clustered objects used by this analysis, and even then only the location of the jets are used (to find and reject overlapping MuSA objects) not their kinematic properties.

4.4 MuSA Extrapolation

The physics objects used in the analysis are `MuonSpectrometerTrackParticles`. In the nominal muon reconstruction the track parameters of `MuonSpectrometerTrackParticles` are extrapolated towards the IP using the ATLAS extrapolator software. Tracks that pass certain pointing requirements are saved for physics analyses and labeled, `ExtrapolatedMuonTrackParticles`. Our signal models contain muons that would often fail these pointing requirements.

To retain signal efficiency we rerun the ATLAS extrapolator software on the `MuonSpectrometerTrackParticles` and save the non-pointing objects. The resulting tracks are then the primary physics objects used in the analysis, and referred to as MuSA tracks. The pull distributions and residual distributions for the extrapolated track parameters are shown in Fig 4.4 and Fig 4.5 respectively. Both pulls and residuals use the post-extrapolation TPs, and the truth track parameters taken with respect to the truth vertex. Since we are using prompt Z+jets events, the truth vertices are located sufficiently close to the IP for this approximation to be valid. The pull distributions fit well to a gaussian (unit width, centered at zero) confirming the sucess of the extrapolation procedure.

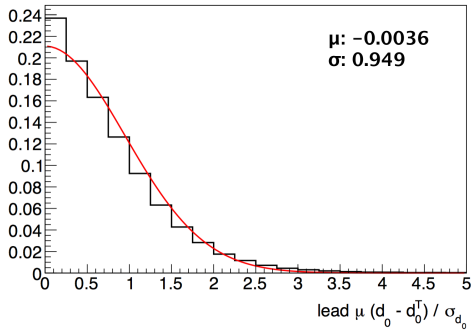

(a)

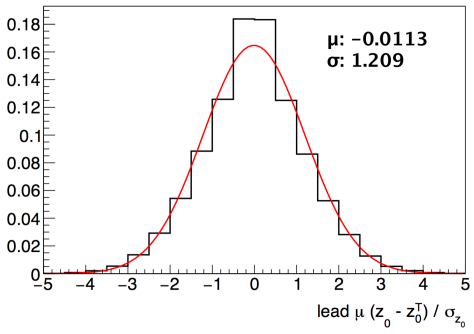

(b)

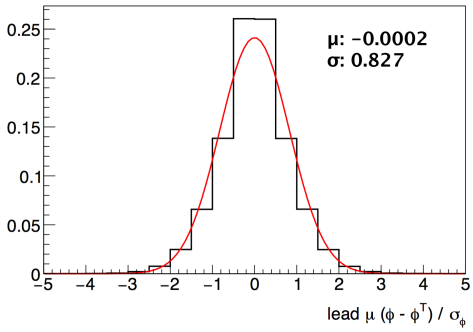

(c)

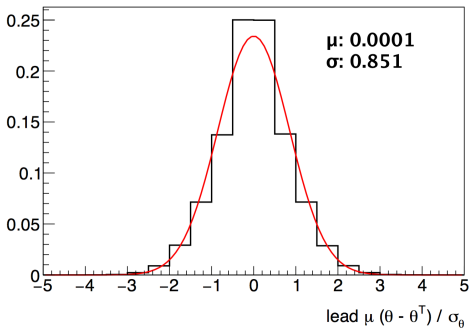

(d)

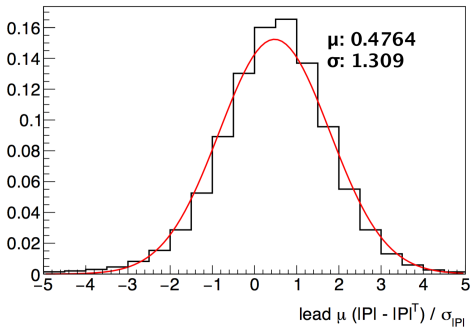

(e)

Figure 4.4: Pull distributions of extrapolated track parameters for : (a) d_0, (b) z_0, (c) ϕ, (d) θ, and (e) $|P|$. All distributions are fit to a gaussian, with scale and width parameters included.

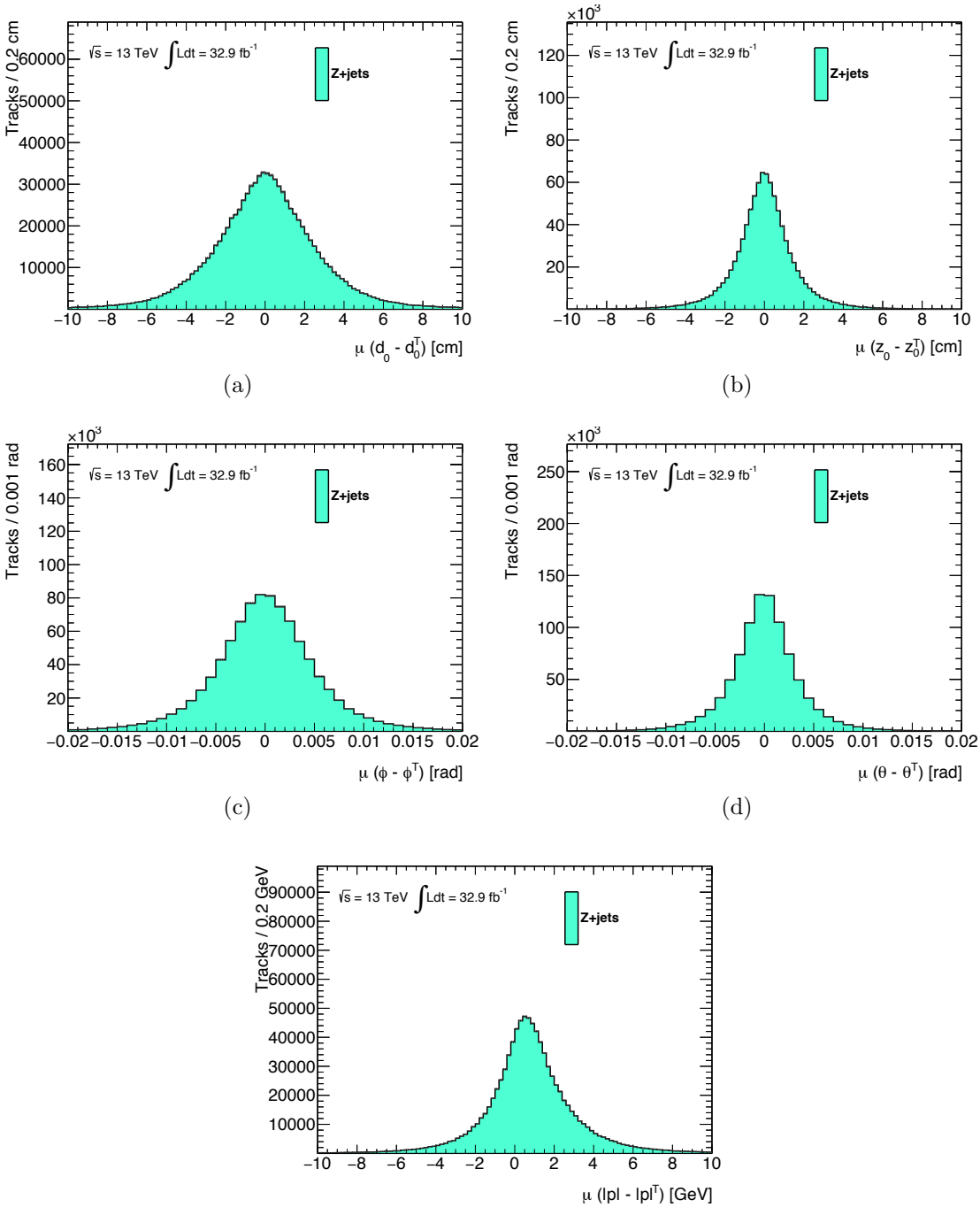

Figure 4.5: Residual distributions of extrapolated track parameters for : (a) d_0, (b) z_0, (c) ϕ, (d) θ, and (e) $|P|$.

4.5 Lifetime reweighting

The signal samples described in Sect. 4.2.1 are generated with only a few different choices of lifetime for the LLP: $c\tau_{\text{gen}} = 0.5$, 1.0 or 5.0 m. Determining the sensitivity of the analysis to other lifetime choices is necessary for limit setting, however generating a very large number of high-statistics samples spanning many orders of magnitude in $c\tau_{\text{gen}}$ is not feasible. We instead adopt the standard procedure of *reweighting* the few existing samples to mimic different lifetimes of interest $c\tau_{\text{new}}$. The weight assigned to any given displaced vertex i associated to an LLP generated with a lifetime of $c\tau_{\text{gen}}$ is given as:

$$w_i\left(t\right) = \frac{\tau_{\text{gen}}}{e^{-t_i/\tau_{\text{gen}}}} \cdot \frac{e^{-t_i/\tau_{\text{new}}}}{\tau_{\text{new}}}\,, \tag{4.2}$$

where the first factor is used to reweight the decay to a flat distribution and the second factor is used to reweight to the desired lifetime. The quantity t_i is the proper decay time of the LLP that gives rise to displaced vertex i and is calculated from the mass and momentum of the LLP.

In the models considered the LLPs are always pair produced. The proper treatment requires two weights to be applied per event, one for each LLP, as shown below.

$$w'_i\left(t_1, t_2\right) = w_i\left(t_1\right) \cdot w_i\left(t_2\right) \tag{4.3}$$

The efficiency for selecting signal events of a given lifetime τ_{new} is given by:

$$\varepsilon_{\text{new}} = \frac{\sum_{i=\text{selected}} w'_i}{\sum_{i=\text{all}} w'_i}\,, \tag{4.4}$$

where the summation in the numerator is over events that pass a given selection criteria and the summation in the denominator is over all LLP that have an opportunity to decay to the final state of interest.

CHAPTER 5

SELECTION

As described in Sect. 1.1, the aim of the analysis is to study events with displaced vertices, that include a pair of muons, in the most model-independent way possible. The event selection should rely dominantly on identification of the dimuon DV as opposed to other activity in the event, such as the presence of jets, heavy-flavor tagging, etc.

5.1 Minimum ΔR

The reconstruction of combined muons is described in Sect. 4.3.1.2. The dominant reasons why a combined track might not be found given a MuSA track are: combined reconstruction inefficiency, that the muon is not "pointing" (i.e. a track with displacement and momentum vectors that are not colinear), or that the track originates sufficiently far from the IP so that there are not enough hits in the ID to make a track. For these reasons a good discriminant against background (i.e. prompt muons) will reject MuSA tracks matched to combined muons.

The track level variable that defines a "match" between MuSA tracks and combined muons is the $\Delta\mathrm{R} = \sqrt{\delta\phi^2 + \delta\eta^2}$ between the MuSA track in question and the closest combined muon track. An illustration of this quantity is shown in Fig. 5.1. If $\Delta\mathrm{R} < 0.1$ then the combined muon is considered matched to the MuSA track.

The quantity $\min(\Delta\mathrm{R}) = \min\{\Delta\mathrm{R}_1, \Delta\mathrm{R}_2\}$ is formed to provide a vertex level object that can discriminate against prompt muon background. An illustration of $\min(\Delta\mathrm{R})$ is shown in Fig. 5.2. The benefit of using $\min(\Delta\mathrm{R})$ versus $\min(d_0)$ or

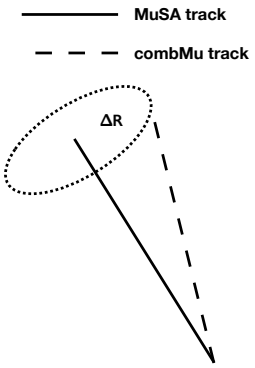

Figure 5.1: Illustration of ΔR discriminant.

r_{vtx} is that min(ΔR) incorporates the measurements from nearby ID tracks. This extra information allows for better separation between signal and background. The dark photon model provides additional motivation for choosing ΔR. The model features large physical decay lengths, which limits the formation of ID tracks, and small dimuon opening angles, which results in small d_0 MuSA tracks. Therefore a large fraction of signal vertices would pass a ΔR cut yet fail any d_0 requirement.

A final benefit of using the min(ΔR) is that it describes the combined reconstruction inefficiency which allows for a straightforward data-driven background estimation as described in Sect. 6.2.

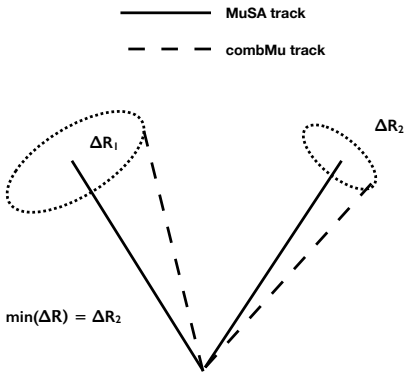

Figure 5.2: Illustration of min(ΔR) discriminant.

Trigger	Description
HLT_mu60_0eta105_msonly	MuSA trigger restricted to the barrel region.
HLT_xe110_mht_L1XE50	Jet p_{T} imbalance trigger with L1 requirement.
HLT_mu20_msonly_mu15noL1_msonly_nscan05_noComb	MuSA trigger requiring second stand alone muon with $\Delta R < 0.5$
HLT_3mu6_msonly	MuSA trigger requiring three SA objects.

Table 5.1: Description of triggers used in the analysis.

5.2 Triggers

We make use of the logical OR of four HLT trigger objects [84] in order to achieve the best possible efficiencies for a wide variety of signal topologies and kinematics. A list of the triggers used and their descriptions are given in Tab. 5.1. The first two triggers in Tab. 5.1 are highly efficient for signals with "high mass" states (mass $>$ 100 GeV) with high p_{T} displaced muons (e.g. the GGM SUSY model), while the final two allow for efficient selection of signals featuring "low mass" states, and therefore lower p_{T} muons (e.g. the dark gauge boson model). All of the muon triggers used are of the "msonly" type. The HLT software trigger utilizes nearly the same muon reconstruction code as does the offline reconstruction. This means the pointing requirements for msonly trigger objects are similar to those of MuSA tracks, and as a result the msonly triggers are necessary for sensitivity to displaced muon signatures.

The thresholds for the $\not{H}_T$ and "narrow scan" triggers changed during the course of 2016 data taking. To account for these changes the highest available threshold for each trigger chain is used and offline requirements are imposed corresponding to the thresholds listed above for each chain. (i.e. the highest thresholds used in 2016 data taking). Additional offline requirements are imposed in conjunction with each trigger to ensure that the trigger is operating at a uniform maximum efficiency. The additional requirements, described in detail below, are based on where the trigger efficiency plateaus with respect to the most relevent distribution for that trigger. (i.e. lead MuSA p_{T} for the single muon trigger)

The increase in instantaneous luminosity for Run 2 requires higher than desired trigger thresholds and unfortunately the efficiency of the HLT_mu60_0eta105_msonly

trigger is relatively low for the signals we are interested in. The $p_{\mathrm{T}} > 60$ GeV and barrel-only requirements significantly reduce the efficiencies for many signal model parameter points; additionally the muon trigger object makes use of an IP constraint to reduce combinatorics which also suppresses selection of muons with large d_0 and/or z_0 (this is, however, also true for the offline MS track reconstruction). The HLT_xe110_mht_L1XE50 trigger requires missing transverse hadronic energy, $\not{H}_T$, to fire. This trigger is most efficient for events with multiple high p_{T} muons and additional jets, typical features of the GGM SUSY model. Fig. 5.3 shows the efficiencies for the HLT_mu60_0eta105_msonly and HLT_xe110_mht_L1XE50 triggers, as functions of the p_{T} of the leading MuSA muon in the event and the reconstructed $\not{H}_T$ respectively. The HLT_mu60_0eta105_msonly efficiency is calculated with respect to all truth muons in the barrel. Both efficiency distributions are made using the dark gauge boson model with $m_{\mathrm{Z_D}} = 20$ GeV, since that model has more vertices near the plateau of each trigger. The HLT_mu60_0eta105_msonly trigger distribution plateaus at $p_{\mathrm{T}} \sim 60$ GeV and so an offline requirement that the lead MuSA $p_{\mathrm{T}} > 60$ GeV, in conjunction with this trigger passing, is used. The HLT_xe110_mht_L1XE50 trigger distribution plateaus at $\not{H}_T \sim 130$ GeV and so an offline requirement that the $\not{H}_T > 130$ GeV, in conjunction with this trigger passing, is used. Note that the HLT_mu60_0eta105_msonly trigger reaches a maximum efficiency well below 100% due to a fall-off in the efficiency to reconstruct MS trigger objects with large d_0.

The HLT_mu20_msonly_mu15noL1_msonly_nscan05_noComb trigger is based on reconstruction of MuSA tracks with low p_{T} thresholds. The large rates associated with the low p_{T} thresholds are offset by requiring *two* muons in the MS that are "near" each other, i.e. within a cone of $\Delta\mathrm{R} < 0.5$. The narrow scan trigger efficiency is displayed in Fig. 5.4. The HLT_mu20_msonly_mu15noL1_msonly_nscan05_noComb trigger distribution plateaus at $p_{\mathrm{T}} \sim 35$ GeV and so an offline requirement that the lead MuSA $p_{\mathrm{T}} > 35$ GeV, in conjunction with this trigger passing, is used. Note that

the efficiency of this trigger on a given signal model is strongly dependent on the size of the boost of the particle decaying to the dimuon final state, as this determines the likelihood of the two muons being found within a cone of size $\Delta R < 0.5$. The HLT_3mu6_msonly trigger benefits from the higher branching fraction to dimuon final states of the Z_D as opposed to the SM Z boson. The result being more events featuring at least three muons than in our high mass baseline models. The triple muon trigger efficiency is displayed in Fig. 5.5. The HLT_3mu6_msonly trigger distribution plateaus well below the analysis selection requirement on MuSA tracks that $p_T > 10$ GeV, described in Sect. 5.4, making an additional offline requirement redundant.

The total trigger efficiencies for the two representative baselines models are shown in Fig. 5.6 as functions of the physical decay length of the long-lived BSM particle. The additional offline requirements specified for each trigger above are only imposed when that is the only trigger passed for the event/vertex in question.

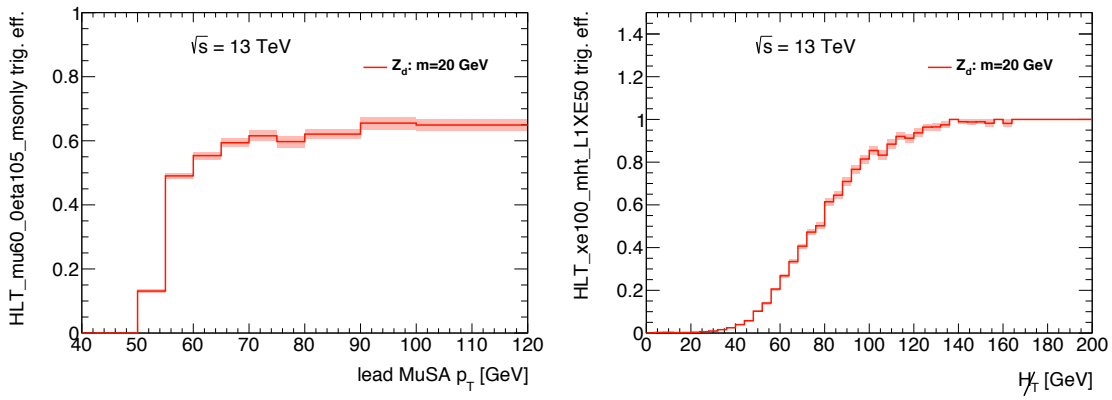

Figure 5.3: The efficiencies of the (a) HLT_mu60_0eta105_msonly trigger, as a function of the p_T of the leading MuSA track in the vertex, and (b) HLT_xe110_mht_L1XE50 trigger, as a function of the reconstructed $\not{H}_T$ in the event. The distributions are derived from signal events with a BSM long-lived dark gauge boson, Z_D ($m_{Z_D} = 20$ GeV and $c\tau_{Z_D} = 0.5$m), that decays to $\mu^+\mu^-$. The shaded bands represent the statistical uncertainty only.

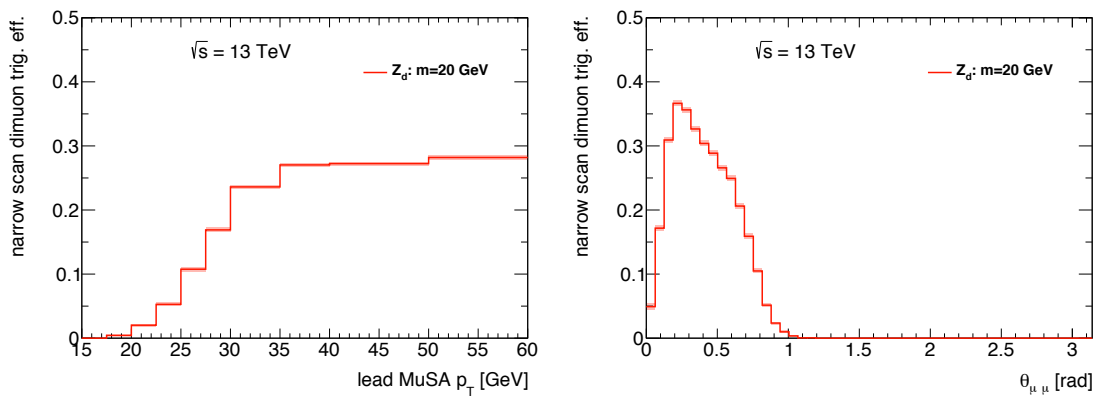

Figure 5.4: The efficiency of the low-mass trigger, HLT_mu20_msonly_mu15noL1_msonly_nscan05_noComb, as a function of (a) the p_{T} of the leading MuSA track in the vertex and (b) the opening angle of the two muons in the vertex. The distributions are derived from signal events with a BSM long-lived dark gauge boson, $\mathrm{Z_D}$ ($m_{\mathrm{Z_D}} = 20$ GeV and $c\tau_{Z_D} = 0.5$m), that decays to $\mu^+\mu^-$. The shaded bands represent the statistical uncertainty only.

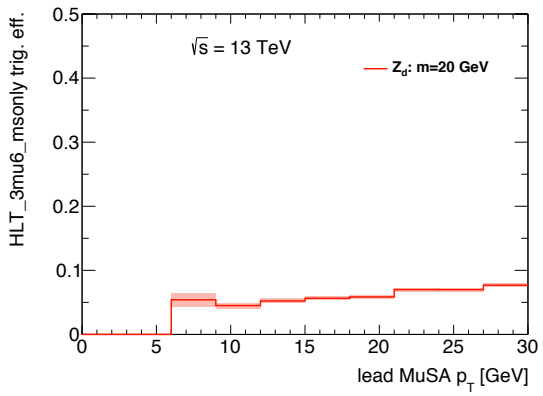

Figure 5.5: The efficiency of the triple muon trigger, HLT_3mu6_msonly, as a function of the p_{T} of the leading MuSA track in the vertex. The distributions are derived from signal events with a BSM long-lived dark gauge boson, $\mathrm{Z_D}$ ($m_{\mathrm{Z_D}} = 20$ GeV and $c\tau_{Z_D} = 0.5$m), that decays to $\mu^+\mu^-$. The shaded band represents the statistical uncertainty only.

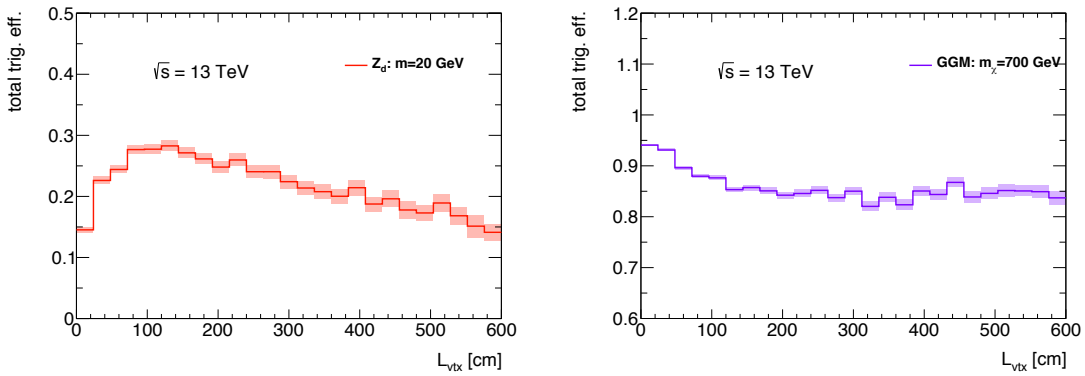

Figure 5.6: The total trigger efficiencies as a function of the true decay length $L_{\text{vtx}}^{\text{true}}$ for (a) signal events with a BSM long-lived dark gauge boson, Z_D ($m_{\text{Z}_\text{D}} = 20$ GeV and $c\tau_{Z_D} = 0.5$m), that decays to $\mu^+\mu^-$, and (b) signal events with a BSM long-lived neutralino, $\tilde{\chi}_1^0$ ($m_{\tilde{\chi}_1^0} = 700$ GeV and $c\tau_{\tilde{\chi}_1^0} = 1$m) decaying to a Z boson (with $Z \to \mu^+\mu^-$) and a gravitino. The shaded bands represent the statistical uncertainty only.

5.3 Isolation

Fake muons from pion/kaon decays constitute a major background for the analysis. Applying an isolation criteria for muons will directly reduce this background. The muon combined performance (MCP) group does not provide isolation working points for MuSA tracks [82], and so we have created one. The isolation variable is defined as the scalar sum of p_T for all ID tracks with $p_\text{T} > 0.5$ GeV in a ΔR cone of 0.4 around the MuSA track in question. ID tracks associated with a muId combined muon within $\Delta\text{R} = 0.1$ of the MuSA track are not used in constructing the isolation variable. The goal of this is to remove the contribution from the muon itself. The isolation variable is normalized with respect to the p_T of the MuSA track and a cut value of 0.05 is used as part of the signal region selection, in order to minimize background and maximize signal sensitivity.

The same isolation requirement is imposed on combined muons that are considered in constructing the ΔR(comb, MS) variable, except with a looser cut value of 0.10. This is done to keep the isolation definitions from sculpting the ΔR variable.

5.4 Offline selection

Events from both data and MC simulation are skimmed according to the trigger requirements described above. Offline *preselection* requirements are applied to obtain smaller samples of events that have characteristics matching what we expect to observe from signal processes. This begins with generic requirements on data quality. Events must be on the good runs list and not have TileCal, Lar, or SCT Corruption problems.

After passing initial quality requirements events must contain a primary vertex (PV), (i.e. the vertex with the largest value for the scalar sum of the p_{T} of tracks). Other vertices likely come from additional softer pp interactions in the event (i.e. 'pileup' interactions).

Track candidates with impact parameters d_0 and/or z_0 larger than the values allowed in the standard combined muon reconstruction are selected by making use of MS stand-alone tracks (MuSA), extrapolated as described in Sect. 4.4, with selection criteria applied in order to ensure that the track parameters are well measured and consistent with a signal-like, non-prompt decay.

Vertices are formed from all possible pairs of MuSA candidates. We use a simple and efficient algorithm that assumes a straight-line extrapolation of the muon trajectory from the MS inner surface towards the IP. The midpoint between the points of closest approach along the back extrapolated trajectories of the two muon candidates is taken to be the three-dimensional location of the vertex. This simple approach is sufficient for the purposes of this analysis, as the location of the putative dimuon vertex is only used in defining the geometrical acceptance of the analysis. Any func-

tion of the muon's p_{T}, η, or ϕ (i.e. m_{ll}) is calculated using the values expressed at the IP after passing through the ATLAS extrapolator. The decay length L_{vtx} and projections onto the x-y plane and z-axis, r_{vtx} and z_{vtx} respectively, are taken to be with respect to the IP.

Category	Cut Name	Requirement
Event Preselection	trigger	Logical OR of triggers in Tab. 5.1
	cleaning	GRL, TileCal, LAr, SCT Corruption
	PV	At least one vertex reconstructed with 2 or more tracks
Baseline Jets	p_{T}	> 10 GeV
	$\lvert\eta\rvert$	< 2.4
	jvt	> 0.59 when $p_{\mathrm{T}} < 60$ GeV
Baseline Combined Muon Tracks	p_{T}	> 10 GeV
	$\lvert\eta\rvert$	< 2.4
	isolation	$\frac{sumTrkPtCone40}{\mu p_{\mathrm{T}}} < 0.1$
	jet-muon overlap	$min\{\Delta R(jet\ ,\ \mu_{CO})\} > 0.4$[1]
Baseline MuSA Tracks	p_{T}	> 10 GeV
	$\lvert\eta\rvert$	< 2.4
	trigger layers	≥ 3 ϕ layers; ≥ 3 η layers
	precision layers	≥ 3
	MCP recommendations	chamber and transition region removal
	additional region removal	veto if $\lvert\eta\rvert < 0.33$ & $0.63 < \phi < 1.26$ (See Sect. 6.2)
	σ_{d_0}	< 20 cm (See App. D)
	isolation	$\frac{sumTrkPtCone40}{\mu p_{\mathrm{T}}} < 0.05$
	jet-muon overlap	$min\{\Delta R(jet\ ,\ \mu_{MS})\} > 0.4$[2]
Vertex Formation	make vertices from all possible pairs of MuSA tracks	
Baseline Vertex Selection	closest approach	< 20 cm
	$\theta_{\mu\mu}$	> 0.1 rad
	geometrical acceptance	$r < 4$ m; $\lvert z\rvert < 6$ m
	$\mathrm{m}_{\mu\mu}$	> 15 GeV
	vertex charge	$\lvert q_{vtx}\rvert = 0$
	cosmic	$\Delta R_{\mathrm{COS}}(\mu_1, \mu_2) = \sqrt{(\Sigma\eta)^2 + (\pi - \Delta\phi)^2} > 0.1$
SR_{Z_D} Selection	min ΔR	> 0.1
	min p_{T}	> 10 GeV
	$m_{\mu\mu}$	$15 - 60$ GeV
SR_{GGM} Selection	min ΔR	> 0.1
	min p_{T}	> 20 GeV
	$m_{\mu\mu}$	> 60 GeV

Table 5.2: Summary of event and objection selection criteria used in the analysis.

[2]The actual requirement is that $min\{0.4, 0.04 + \frac{10}{\mu\ p_{\mathrm{T}}}\} < min\{\Delta R(jet, \mu_{\mathrm{MS}})\}$ as recommended by the jetEtMiss group, however the simpler requirement is used throughout the text for brevity.

Signal is characterized by vertices composed of muons that are not associated with an ID track, hence, the primary selection criteria of our signal regions is that $0.1 < min\{\Delta R(\mu_{\mathrm{COMB}}, \mu_{\mathrm{MS}})\}$. The $min\{\Delta R(\mu_{\mathrm{COMB}}, \mu_{\mathrm{MS}})\}$ requirement unavoidably leads to a drop in efficiency for decays close to the IP. Displaced vertex analyses that make use of ID tracks effectively recover such signal events. The $min\{\Delta R(\mu_{\mathrm{COMB}}, \mu_{\mathrm{MS}})\}$ distribution for vertices passing the baseline selection is shown in Fig. 5.7 for both SM MC simulation and our bench mark signal models.

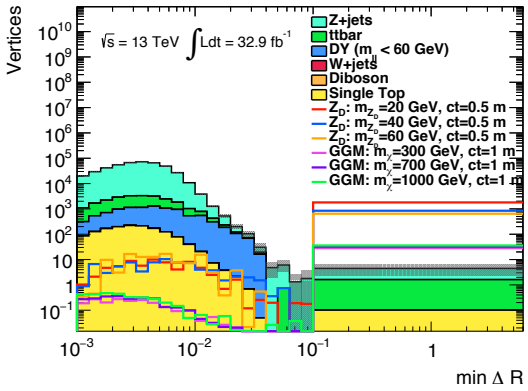

Figure 5.7: Distribution of $min\{\Delta R(\mu_{\mathrm{COMB}}, \mu_{\mathrm{MS}})\}$ for vertices passing the preselection for both SM and BSM MC simulation. The shaded bands represent the statistical uncertainty only.

We use two signal regions to increase the sensitivity to low and high mass signal models. All of the event and object selection for both the baseline and signal regions are described in Tab. 5.2.

5.5 Signal efficiencies

Using MC-simulated signal events, the vertex-finding efficiencies (relative to all signal vertices) as functions of true d_0, true L_{vtx}, true p_{T}, and the opening angle between the two muons in the vertex are given in Fig. 5.8, for the GGM SUSY model, and Fig. 5.9, for the dark boson model. The corresponding signal truth distributions are given in App. C to aid in understanding these efficiencies. The

loss of efficiency for small decay lengths/opening angles is due to the veto of prompt, combined muons, while the drop-off at large decay lengths/opening angles reflects the falling MuSA efficiency for tracks that do not point to the IP. Due to the large difference in boost for the different Z_D mass points the peaks in efficiency are located at noticably different values.

The residual distributions for the physical decay length L_{vtx} and radial vertex positions r_{vtx} are shown in Fig. 5.10. The residuals demonstrate that the average resolution is about $2 - 3$ cm. The resolution has little dependence on the physical decay length, but does deteriorate significantly for small dimuon opening angle, for the reasons described above.

The selection requirements, along with cutflows, for vertices entering our signal region are summarized in App. A for the primary SM backgrounds estimated using MC simulation as well as for our two benchmark signal models. The total efficiencies, trigger and offline selection criteria applied, as functions of the lifetime of the long-lived BSM particle, are given in Fig. 5.11, for both baseline models that have been considered. The reweighted samples, as described in Sect. 4.5, have been used to estimate the efficiencies for values of the lifetime that were not used in generating the simulated samples. Various distributions for simulated signal vertices in SR_{GGM} and SR_{Z_D} are displayed in Fig. 5.12 and Fig. 5.13 respectively.

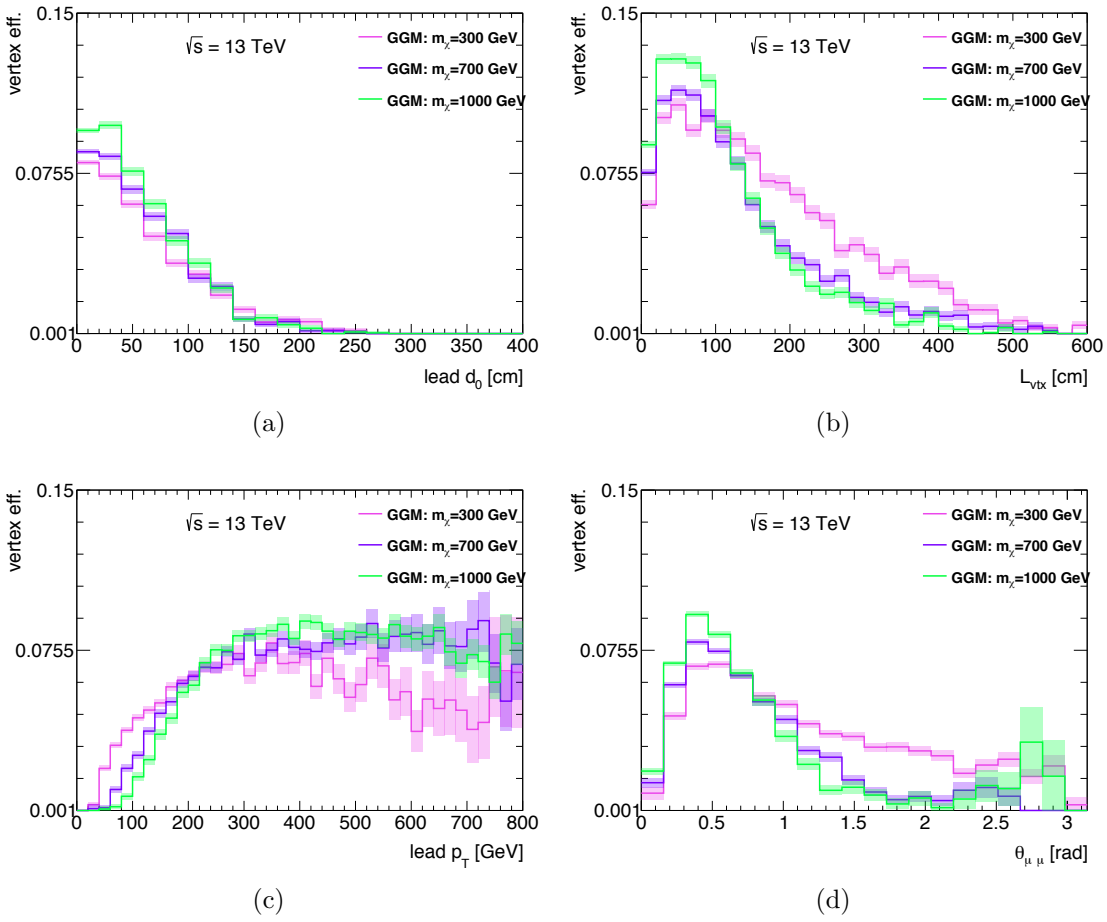

Figure 5.8: The efficiencies to select a displaced dimuon vertex that satisfies the requirements of the SR_{GGM}, as function of (a) true d_0, (b) true L_{vtx}, (c) true p_{T}, and (d) the opening angle between the two muons in the vertex. These efficiencies are calculated relative to all generated signal vertices. The distributions are derived from signal events with a BSM long-lived neutralino, $\tilde{\chi}_1^0$, decaying to a Z boson (with $Z \to \mu^+\mu^-$) and a gravitino. The shaded bands represent the statistical uncertainty only.

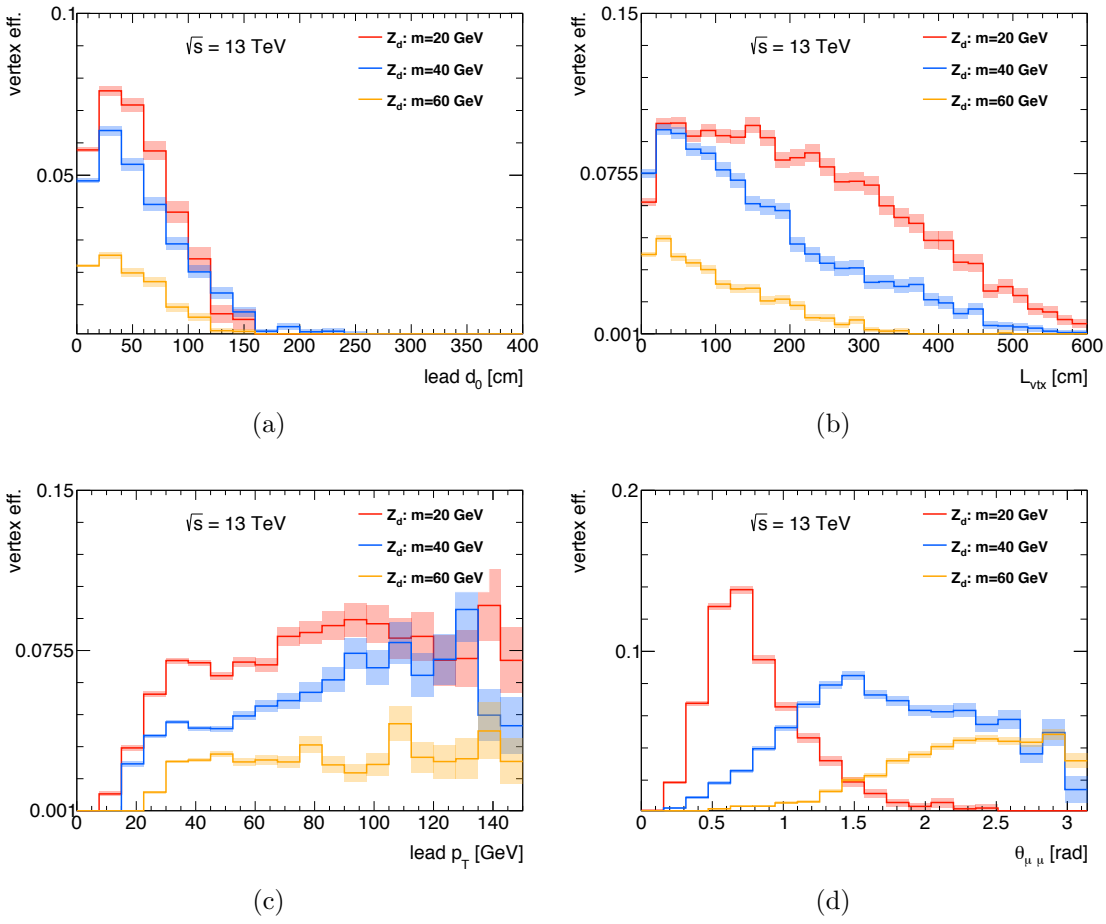

Figure 5.9: The efficiencies to select a displaced dimuon vertex that satisfies the requirements of the SR_{Z_D}, as function of (a) true d_0, (b) true L_{vtx}, (c) true p_{T}, and (d) the opening angle between the two muons in the vertex. These efficiencies are calculated relative to all generated signal vertices. The distributions are derived from signal events with a BSM long-lived dark gauge boson, Z_D, that decays to $\mu^+\mu^-$. The shaded bands represent the statistical uncertainty only.

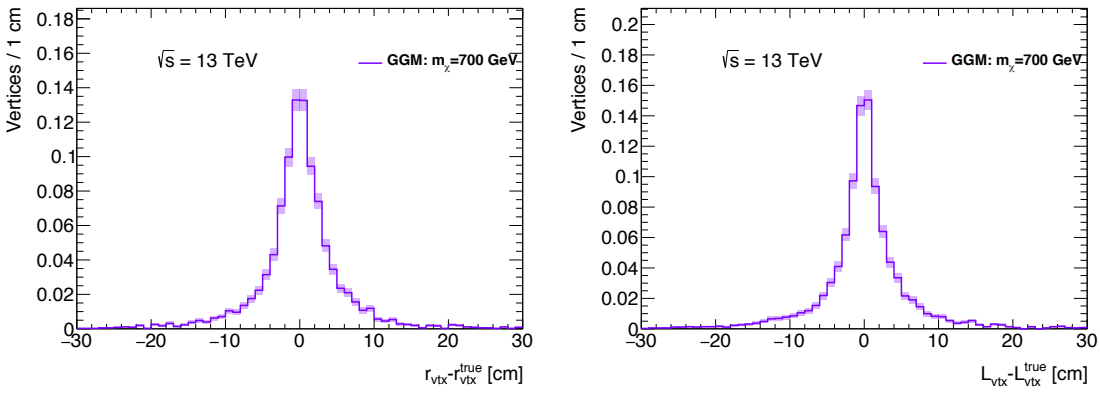

(a) (b)

Figure 5.10: The residual distributions (reconstructed value minus true value) for (a) r_{vtx} and (b) L_{vtx}. The distributions are derived from signal events with a BSM long-lived neutralino, $\tilde{\chi}_1^0$ ($m_{\tilde{\chi}_1^0} = 700$ GeV and $c\tau_{\tilde{\chi}_1^0} = 1$m) decaying to a Z boson (with $Z \to \mu^+\mu^-$) and a gravitino. The shaded bands represent the statistical uncertainty only.

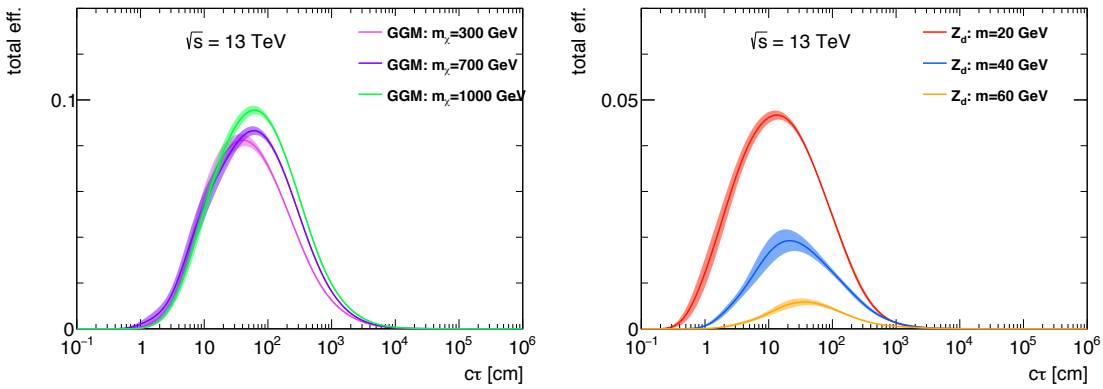

(a) (b)

Figure 5.11: Overall efficiencies (combining trigger and offline selection), as a function of the lifetime of the long-lived BSM particle, $c\tau_{\text{BSM}}$, for (a) the GGM SUSY model and (b) the dark gauge boson model. The shaded bands represent the statistical uncertainty only.

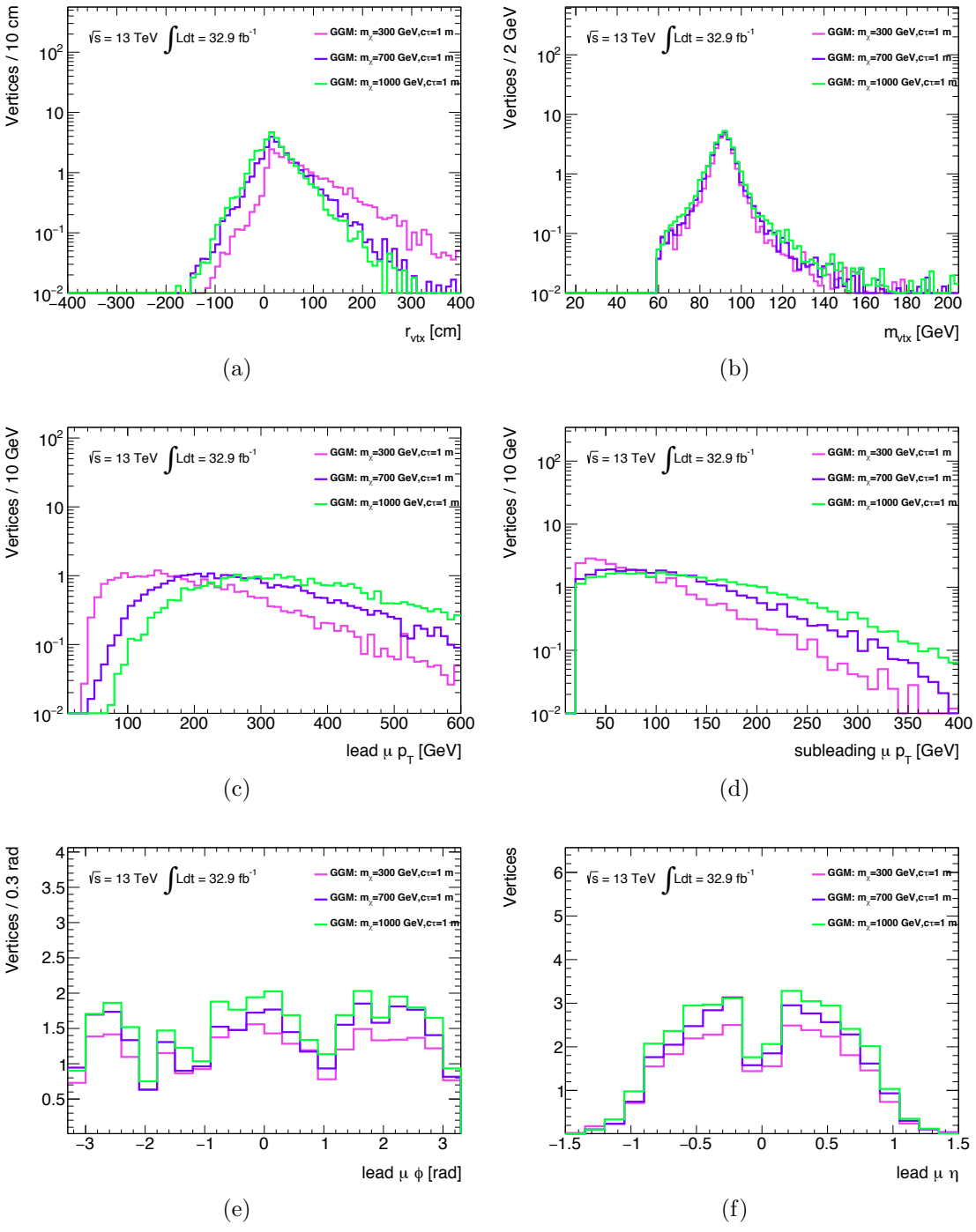

Figure 5.12: Distributions of (a) r_{vtx}, (b) m_{vtx}, (c) lead μ p_{T}, (d) subleading μ p_{T}, (e) lead μ ϕ, and (f) lead μ η for signal vertices in SR_{GGM} with a BSM long-lived neutralino, $\tilde{\chi}_1^0$ decaying to a Z boson (with $Z \to \mu^+\mu^-$) and a gravitino. The signal is scaled to 32.9 fb^{-1}.

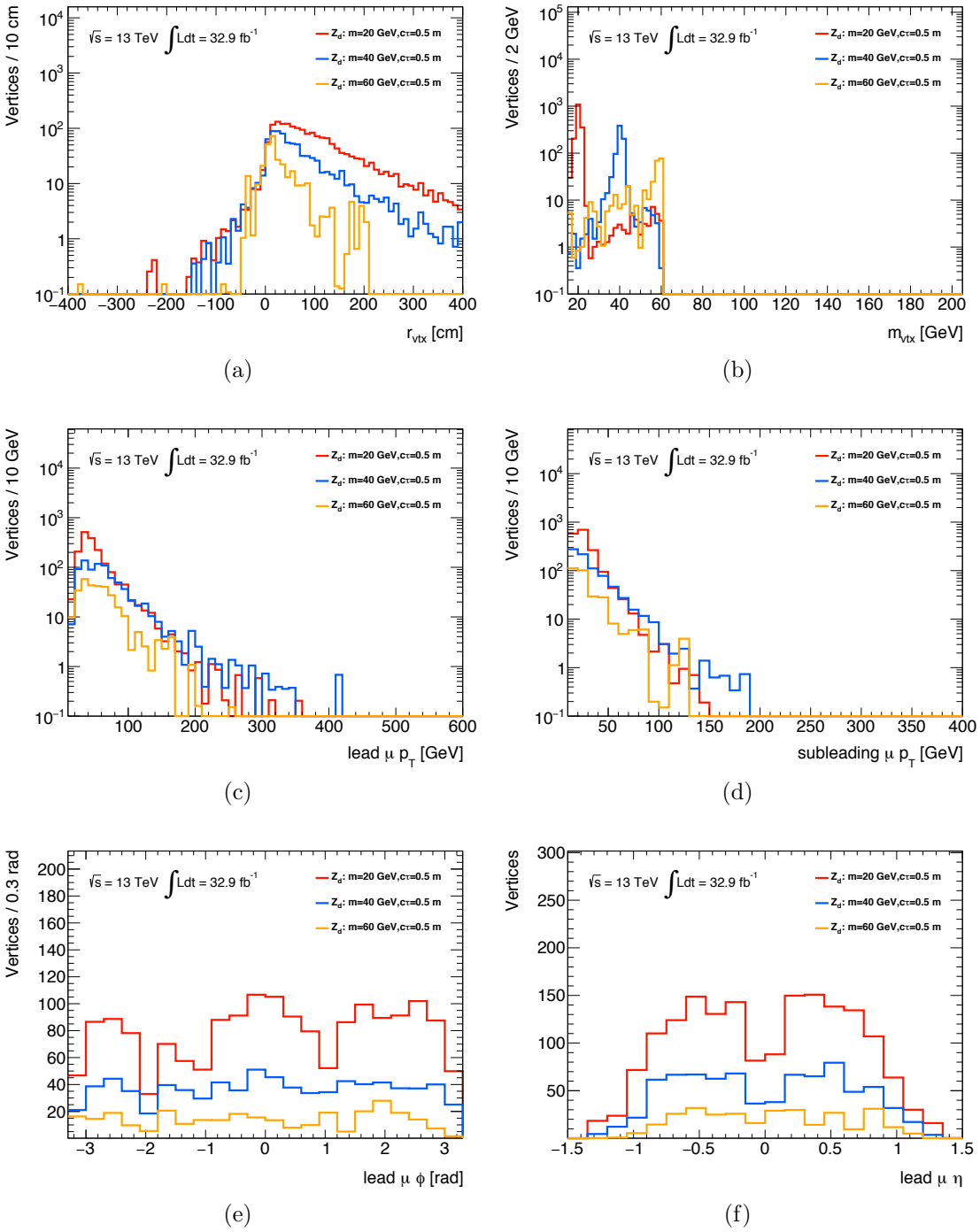

Figure 5.13: Distributions of (a) r_{vtx}, (b) m_{vtx}, (c) lead μ p_{T}, (d) subleading μ p_{T}, (e) lead μ ϕ, and (f) lead μ η for signal vertices in SR_{Z_D} with a BSM long-lived dark gauge boson that decays to $\mu^+\mu^-$. The signal is scaled to 32.9 fb^{-1}.

CHAPTER 6

ESTIMATION OF BACKGROUNDS

As there are no long-lived SM particles that decay to final states with a dimuon pair, it is to be expected that the dominant backgrounds in this analysis fall into the following categories: SM Drell-Yan (DY) or Z+jets production, where a $Z \to \mu^+\mu^-$ vertex is erroneously reconstructed far from the IP (prompt muon background); random pairing of MuSA tracks that are not associated with a true muon (e.g. fake muon background from QCD events); pairing of unrelated muon tracks in SM background events (e.g. muons from two semileptonic top decays in $t\bar{t}$ events); or non-beam-related events (e.g. cosmic muons). The following sections describe the methods used to estimate the number of background vertices entering our analysis.

6.1 Fake muons

MuSA tracks for which no matching ID track is expected are referred to as "fake" muons. The primary sources of fake muons are cosmic/BIB muons and those arising from pion/kaon decay. Cosmic and BIB (Beam Induced Background) muons are not expected to pass the pointing requirements associated with ID tracks, and as a result produce MuSA tracks that enter our signal selection. Pions and kaons have non-negligible lifetimes and feature large branching fractions to final states with at least one muon. Such decays often feature a kinked track which can result in either no ID track being present, or the ID track failing to be associated to the MS track. In either case a MuSA track will be produced and might enter the signal selection.

Vertices that contain one, in the case of W+jet events, or two, in the case of QCD dijet events, fake muons are referred to as "fake" vertices. The correlation of track charge in fake vertices is quantified using the ratio of opposite sign (OS) to same sign (SS) vertices, $R_q = \frac{N^{OS}}{N^{SS}}$. This ratio can be used to predict the number of fake vertices entering our signal selection (i.e. $N^{OS} = R_q \times N^{SS}$), however the ratio will depend on the what the source of the fake vertices is. If the vertex contains cosmic/BIB like muons the charge of the two tracks will clearly be uncorrelated, (i.e. $R_q^{COS} = 1$). For fake vertices arising from pion/kaon decay R_q^{QCD} must be calculated. We expect muons from pion/kaon decay to be non-isolated, and so we study R_q^{QCD} in data as a function of the minimum vertex isolation (min μ_{iso}). For the vertex selection we impose the preselection criteria, except for the isolation, jet-muon overlap requirement, and vertex charge cuts. We then perform a linear χ^2 fit to the min μ_{iso} distribution above 0.1 (i.e. where the contribution from the prompt tails becomes negligible), and take $R_q^{QCD} = f(0.025)$ as our prediction, (i.e. at the midpoint of our preselection's isolation range). The fits/distributions are shown for each of the ABCD regions defined in the subsequent section in Fig. 6.1.

Since we do not know the composition of our fake background, we use $R_q^{Avg} = \frac{R_q^{QCD}+R_q^{COS}}{2}$ for the central value and $\delta R_q = \frac{R_q^{QCD}-R_q^{COS}}{2}$ as the uncertainty. The R_q values used for each of the ABCD regions defined in the subsequent section are given in Tab. 6.1.

Region	R_q^{QCD}	R_q^{AVG}
A	1.47 ± 0.01	1.24 ± 0.24
B	1.55 ± 0.03	1.28 ± 0.28
C	1.39 ± 0.03	1.20 ± 0.20
D	1.39 ± 0.09	1.20 ± 0.20

Table 6.1: Comparison of R_q^{AVG} for each of the ABCD regions.

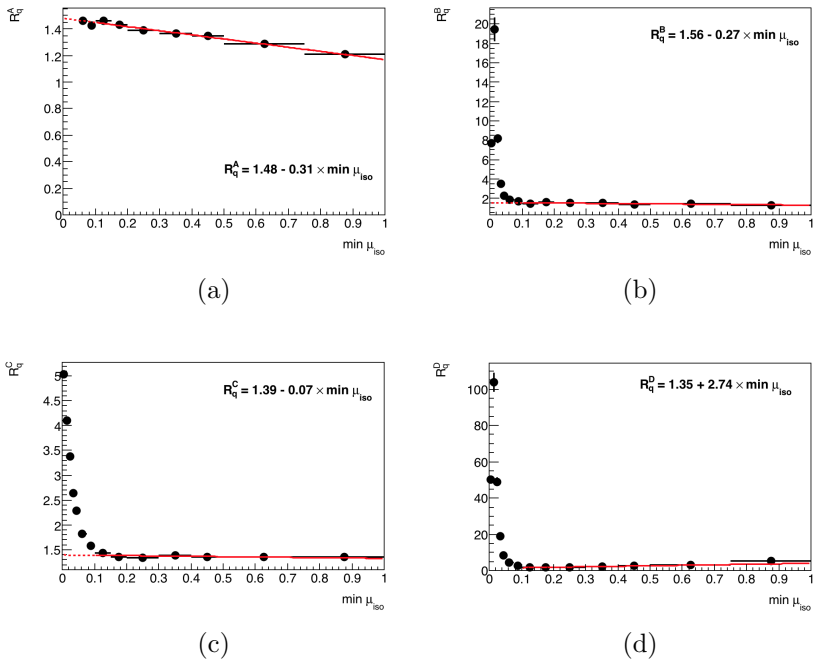

Figure 6.1: The distributions of (a) R_q^A, (b) R_q^B, (c) R_q^C, and (d) R_q^D for displaced vertices with preselection criteria enforced, except for the isolation, jet-muon overlap requirement, and vertex charge cuts, for an integrated luminosity of 32.9 fb^{-1}. The uncertainty on data is purely statistical.

6.2 Prompt muons (ABCD method)

The dominant SM backgrounds that give rise to dimuon vertices are Z+jets/DY, ttbar, and diboson. While none of these processes create real displaced dimuon vertices, inefficiency in the combined muon reconstruction creates displaced dimuon pairs that enter the signal region. Prompt muons can be background like (ΔR < 0.1) and referred to as μ_{CO} since a combined muon is matched to the MuSA track, or signal like (ΔR > 0.1) and will be referred to as μ_{MS} since only a MuSA track is present. Fake muons, as described in Sect. 6.1, will be referred to as μ_F.

Vertices passing the preselection requirements will exist in one of the four quadrants of the $\Delta R_L - \Delta R_S$ plane shown in Fig. 6.2. Region A coincides with the signal region. Regions B and C contain the vertices with one signal like muon and one background like muon. Finally, region D contains well reconstructed real dimuon vertices.

All of the regions in the figure have the types of vertices they contain listed using the convention that the first and second muon type represent the lead and subleading muon respectively. These regions are used to determine the ratio (i.e. transfer factor) of vertices with signal like muons to those without, but first the number of "fake" vertices must be removed. This is done using the following equation:

$$X^* = X_{OS} - X_{SS} \times R_q^X, \qquad X = B, C, D \tag{6.1}$$

where X_{OS} gives the number of OS vertices in a region, X_{SS} is the number of SS vertices in that region and R_q^X is the appropriate OS/SS ratio described in the previous section. While we expect little to no fake vertices in region D we still subtract off the appropriate SS contribution to keep the method consistant.

Region B^* contains lead muons that fail combined reconstruction, while region D^* contains lead muons that pass the combined reconstruction. In both regions the subleading muon passes combined reconstruction. Region C^* contains subleading muons that fail combined reconstruction, while region D^* contains subleading muons that pass the combined reconstruction. In both regions the lead muon passes combined reconstruction. With these definitions the subleading and lead transfer factors are given respectively in the following equations:

$$f^L = \frac{B^*}{D^*}, \qquad f^S = \frac{C^*}{D^*} \tag{6.2}$$

The lead transfer factor multiplied by the C^* yield or the subleading transfer factor multiplied by the B^* yield will predict the number of $\mu_{MS} - \mu_{MS}$ vertices in region A as shown in the following equation:

$$A_{\mu_{MS}-\mu_{MS}} = \frac{B^* \times C^*}{D^*} \tag{6.3}$$

The $\eta - \phi$ distributions for lead muons in region B^* and subleading muons in region C^* are displayed in Fig. 6.3. As can be seen in the figures, the bins with

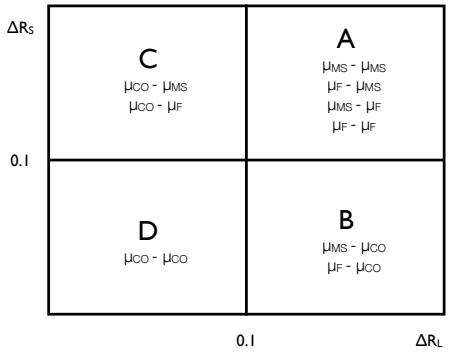

Figure 6.2: Illustration of the $\Delta R_L - \Delta R_S$ plane divided into regions A,B,C and D.

$|\eta| < 0.33$ & $0.63 < \phi < 1.26$ have significantly more muons than the rest of the detector. Since it is not clear what is causing this (i.e. alignment or resolution effects) the region has been vetoed from the preselection.

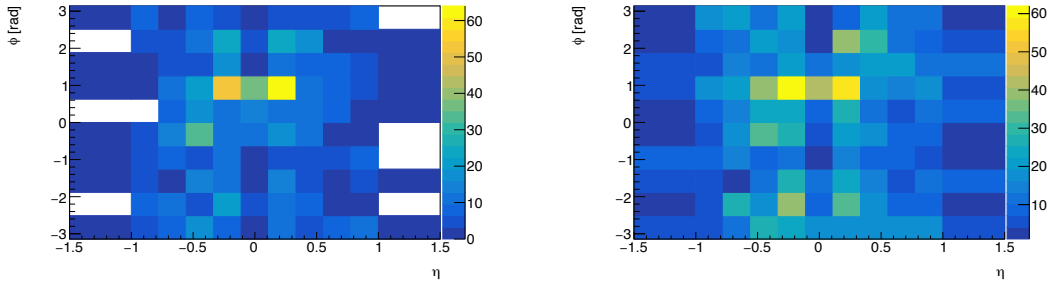

(a) (b)

Figure 6.3: $\eta - \phi$ distributions for (a) lead MuSA tracks in region B^* and (b) subleading MuSA tracks in region C^*. The distributions are derived from data using 32.9 fb^{-1}.

6.3 Cosmic Muon Background

Due to the pointing requirements within the muon reconstruction software, it is more probable that a cosmic muon traversing the detector will only be reconstructed in one hemisphere of the detector as opposed to both. The fake vertex background prediction will account for signal vertices containing one leg of a cosmic muon and another uncorrelated muon. It will not account for cases when both legs of a cosmic muon are reconstructed, and so their contribution to the signal yield must be predicted. MC generation of such a signal is difficult and unreliable and so a data driven method is used.

Cosmic muons create two MuSA tracks that are nearly colinear. This means the two tracks will be back to back in ϕ and have η values that sum to zero. The discriminant $\Delta R_{\mathrm{COS}} = \sqrt{(\Sigma\eta)^2 + (\pi - \Delta\phi)^2}$ is created to separate cosmic muon background (cosmic muons have $\Delta R_{\mathrm{COS}} \sim 0$). The flux of cosmic muon tracks primarily come through the access shafts at the top of the ATLAS cavern, due to minimum shielding, and therefore have an asymmetric ϕ distribution, and η values corresponding to the location of the access shafts ($|\eta| \sim 0.7$). The ΔR_{COS} distribution for events passing the preselection (except for the ΔR_{COS} cut) with the SR min(ΔR) requirement inverted is given in Fig. 6.4. For $\Delta R_{\mathrm{COS}} < 0.1$ the distribution has a cosmic component which is evident from the data/MC ratio. This illustrates why the $\Delta R_{\mathrm{COS}} > 0.1$ selection requirement is part of the preselection. Additional distributions are displayed in Fig. 6.5 with the preselection requirements enforced, except that the ΔR_{COS} requirement is inverted to highlight cosmic dimuon vertices.

6.4 BIB (Beam Induced Background)

BIB events occur when interactions between one of the proton beams and a beampipe mask upstream of the collision point create high energy muons entering the ATLAS detector nearly parallel to the beampipe. The Non-Collision Background

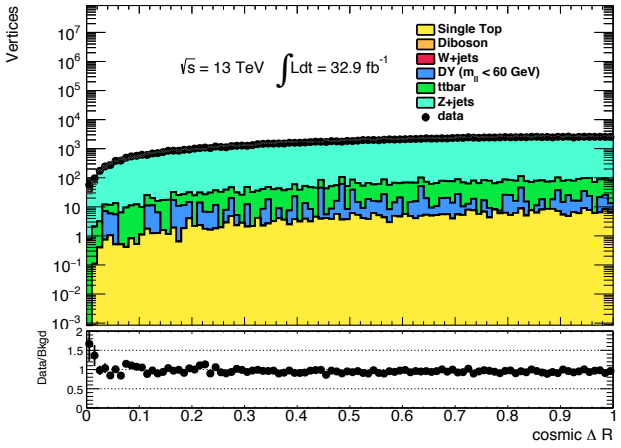

(a)

Figure 6.4: The distributions of ΔR_{COS}. The stacked histograms represent the contributions from SM background processes and are derived from MC-simulated samples scaled to an integrated luminosity of 32.9 fb^{-1}. The observed distribution in data is given by the points with error bars. The lower pane displays the ratio of data (point) to predicted background (histogram), bin-by-bin. The uncertainties on data and MC simulation are purely statistical.

(NCB) group have created the "Two-sided no-time method" of identifying such events [85]. This method reconstructs the BIB muon trajectory by finding a coincidence of muon segments in the endcap muon system and jet objects in the calorimeters. While this method is primarily used to tag jets that have resulted from BIB muons, we employ the method to remove any possible MuSA objects arising from BIB events. This is performed by removing any MuSA objects from the analysis that contain muon segments identified by the above procedure. Any vertices arising from BIB muons that are not removed will be accounted for with the fake vertex background prediction.

6.5 Estimation of background in the signal regions

The number of fake vertices in the SRs is predicted using the number of SS vertices passing the SR requirements and the appropriate R_q, as described in Sect. 6.1. The predicted yields for both SRs are given in Tab. 6.2. Various distributions for SS

vertices in SR_{Z_D} are displayed in Fig. 6.6 and for SR_{GGM} in Fig. 6.7. The low statistics limits what can be inferred from these distributions, however the lack of clustering of vertices at particular values give confidence that there is not a major systemic effect that has been ignored regarding this prediction.

The number of prompt vertices in the SRs is predicted using the ABCD method described in Sect. 6.2. The BCD region yields as well as the predictions for region A are summarized in Tab. 6.2. The leading and subleading transfer factors used for the ABCD prediction are given in Tab. 6.3. The distribution of vertices in the ABCD plane, passing the preselection and all SR requirements except for the min(ΔR) requirement, is given for both benchmark signal model selections in Fig. 6.8.

Region	OS yield	SS yield	Fake muon estimate (= SS $\times R_q$)	Prompt muon estimate (= OS - SS $\times R_q$)	Fake + prompt muon estimate
B	123	65	83 ± 21	40 ± 24	
C	450	331	397 ± 70	53 ± 73	
D	19035	3233	3880 ± 650	15155 ± 665	
A	XXXX	12	14.9 ± 5.2	0.14 ± 0.21 (= B × C / D)	15.0 ± 5.2

(a) SR_{Z_D}

Region	OS yield	SS yield	Fake muon estimate (= SS $\times R_q$)	Prompt muon estimate (= OS - SS $\times R_q$)	Fake + prompt muon estimate
B	1830	2	2.6 ± 2.0	1827 ± 43	
C	1698	21	25 ± 6.9	1673 ± 42	
D	395341	407	488 ± 85	394853 ± 634	
A	XXXX	2	2.5 ± 1.9	7.7 ± 0.3 (= B × C / D)	10.2 ± 1.9

(b) SR_{GGM}

Table 6.2: Yields for (a) SR_{Z_D} and (b) SR_{GGM} in regions A,B,C, and D of transfer factor method given an integrated luminosity of 32.9 fb^{-1}. All quoted uncertainties are purely statistical.

	SR_{Z_D}	SR_{GGM}
$f_L(= B*/D*)$	0.0026 ± 0.0016	0.0046 ± 0.0001
$f_S(= C*/D*)$	0.0035 ± 0.0048	0.0042 ± 0.0001

Table 6.3: The Lead and subleading transfer factors of the ABCD method are shown for both SR_{Z_D} and SR_{GGM}, given an integrated luminosity of 32.9 fb^{-1}. All quoted uncertainties are purely statistical.

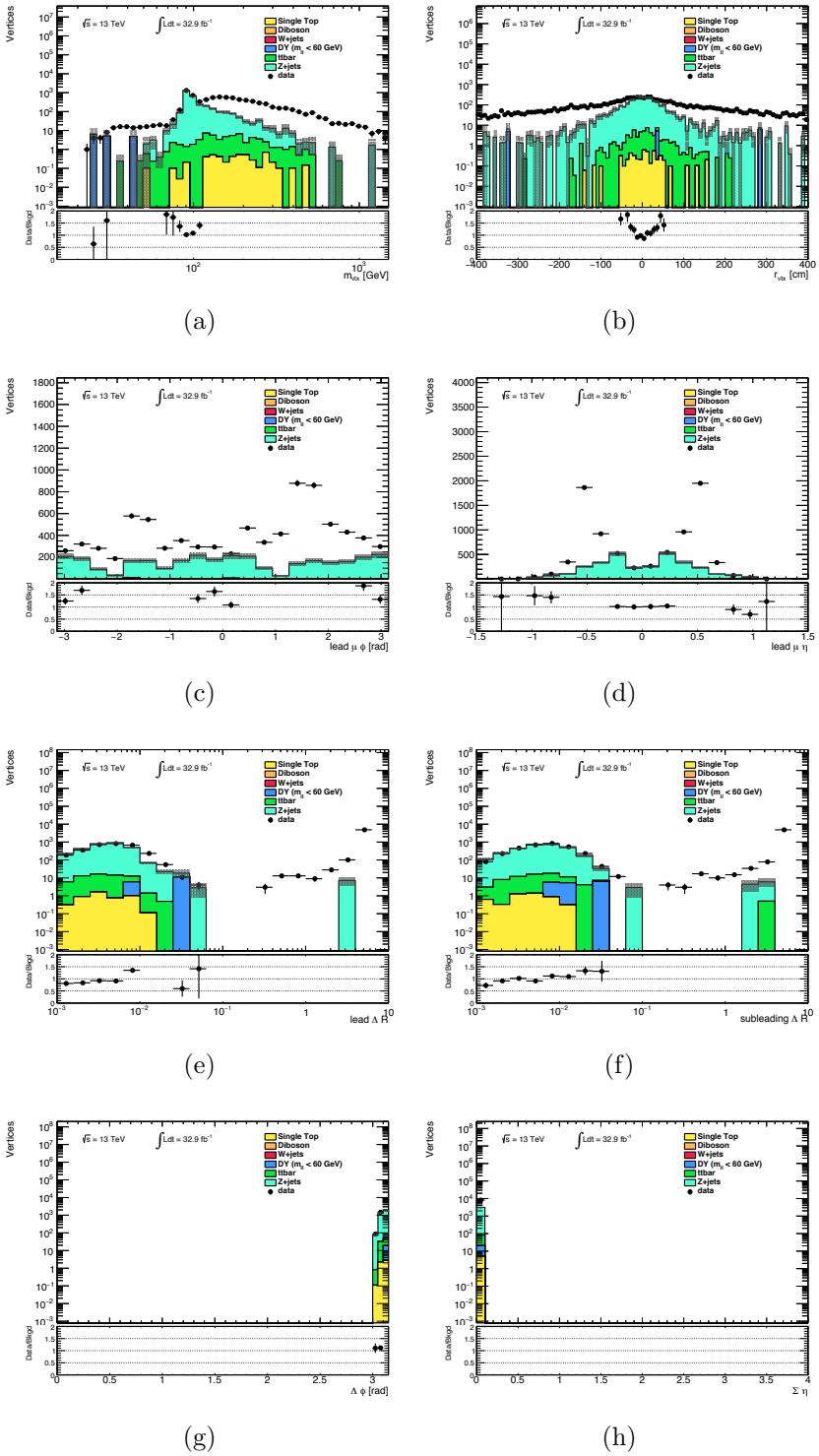

(a) (b) (c) (d) (e) (f) (g) (h)

Figure 6.5: The distributions of (a) m_{ll}, (b) r_{vtx}, (c) lead μ ϕ, (d) lead μ η, (e) lead μ ΔR, (f) subleading μ ΔR, (g) $\Delta\phi$, and (h) $\Sigma\eta$ for displaced vertices with the preselection requirements enforced, but the ΔR_{COS} requirement inverted. The stacked histograms are derived from MC-simulated samples scaled to an integrated luminosity of 32.9 fb^{-1}. The observed distribution in data is given by the points with error bars. The uncertainties on data and MC simulation are purely statistical.

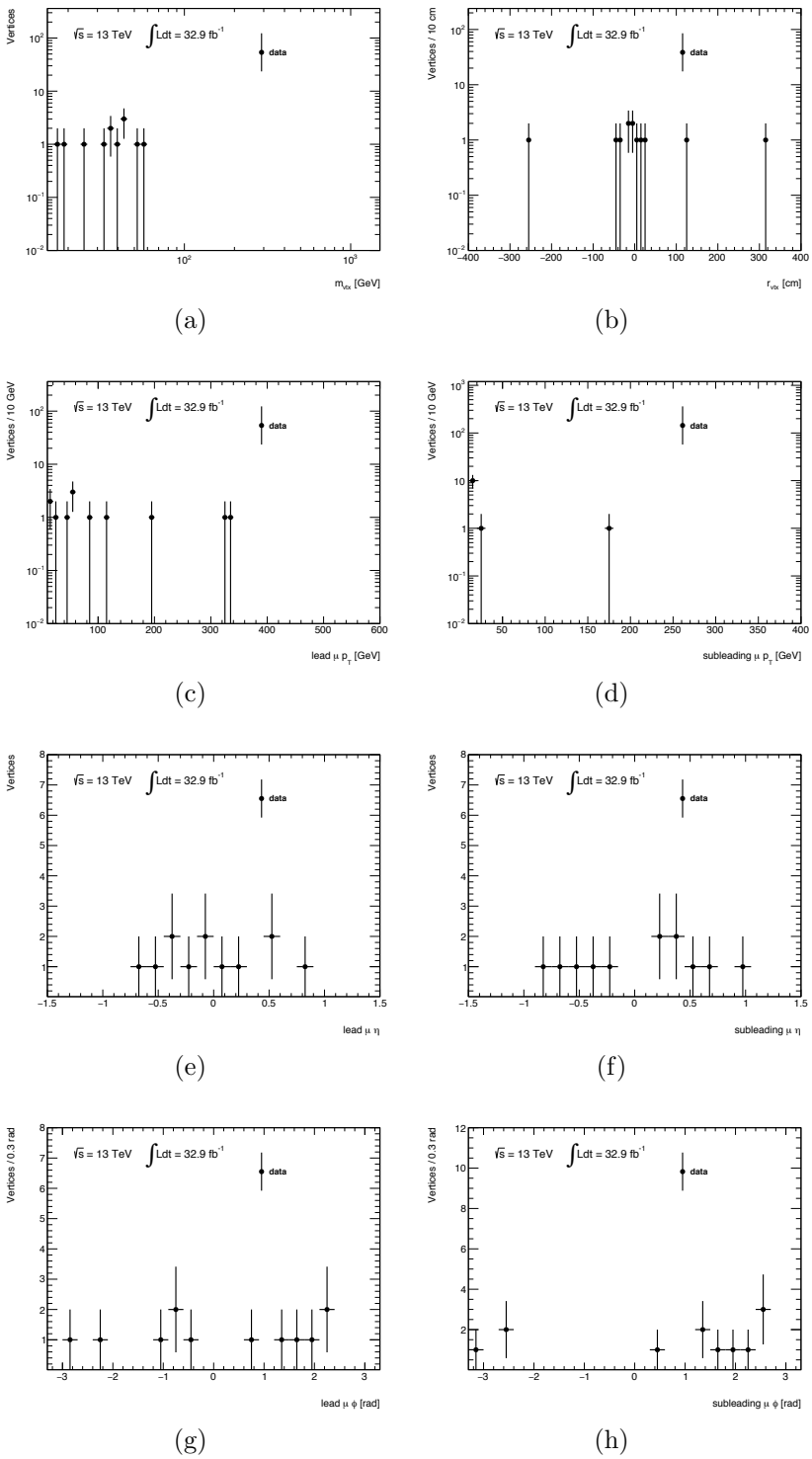

Figure 6.6: The distributions of (a) m_{ll}, (b) r_{vtx}, (c) lead μ p_{T}, (d) subleading μ p_{T}, (e) lead μ η, (f) subleading μ η, (g) lead μ ϕ, (h) subleading μ ϕ for displaced vertices passing the preselection and SR_{Z_D} requirements, with the vertex charge requirement inverted. The observed distribution in data is given by the points with error bars. The uncertainty on data is purely statistical.

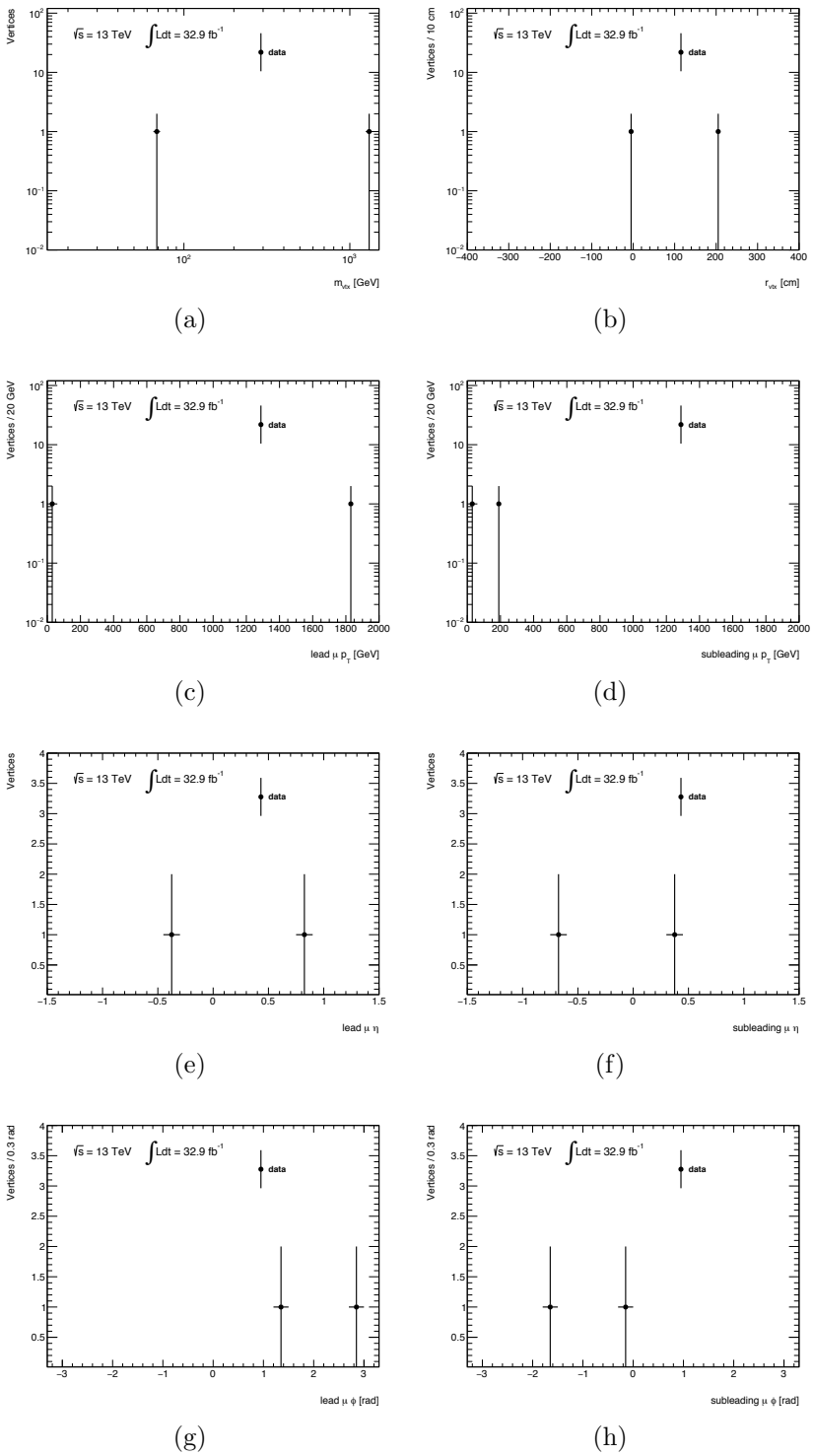

Figure 6.7: The distributions of (a) m_{ll}, (b) r_{vtx}, (c) lead μ p_{T}, (d) subleading μ p_{T}, (e) lead μ η, (f) subleading μ η, (g) lead μ ϕ, (h) subleading μ ϕ for displaced vertices passing the preselection and SR_{GGM} requirements, with the vertex charge requirement inverted. The observed distribution in data is given by the points with error bars. The uncertainty on data is purely statistical.

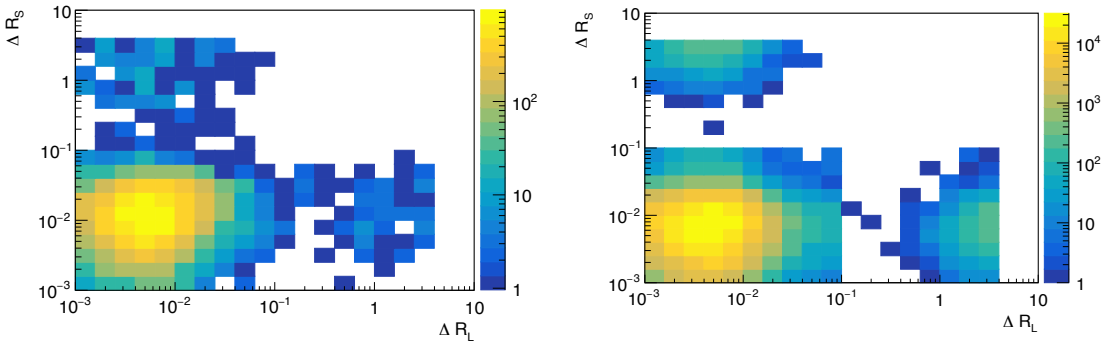

(a) (b)

Figure 6.8: $\Delta R - \Delta R$ distributions for (a) SR_{Z_D} and (b) SR_{GGM}. The distributions are derived from data using 32.9 fb^{-1}.

CHAPTER 7

VALIDATION

7.1 ABCD transfer factor profiling

The ABCD method defines the lead and subleading transfer factors which are used to predict the prompt background in region A. The nominal case assumes that the transfer factors are constant, however they might vary as a function of vertex level variables. It is necessary, therefore, to validate the assumption by profiling the transfer factors.

7.1.1 $\eta - \phi$ profiling

To include detector effects that might go unaccounted for in our global prediction the transfer factors are profiled using $\eta - \phi$. The logic of the method is given in the following equations:

$$
\begin{aligned}
i \in \{\eta\}, \;\; j \in \{\phi\}, \qquad X^{*L}_{ij} = (X_{OS})^L_{ij} - (X_{SS})^L_{ij} \times R^X_q, \qquad X = B, C, D \\
f^L_{ij} = \frac{B^{*L}_{ij}}{D^{*L}_{ij}}, \qquad f^S_{ij} = \frac{C^{*S}_{ij}}{D^{*S}_{ij}} \\
A^L_{\mu_{MS}-\mu_{MS}} = \sum_{ij} f^L_{ij} C^{*L}_{ij}, \qquad A^S_{\mu_{MS}-\mu_{MS}} = \sum_{ij} f^S_{ij} B^{*S}_{ij}
\end{aligned} \tag{7.1}
$$

The $\eta - \phi$ distributions for the lead/subleading transfer factors and yields are given in Fig. 7.1 for SR_{GGM}. SR_{Z_D} does not contain enough statistics to profile in $\eta - \phi$. The integrated yields for SR_{GGM} are displayed in Tab. 7.1. While there are

some bins with seemingly large transfer factors, both leading and subleading methods give results consistant with each other and with the global prediction.

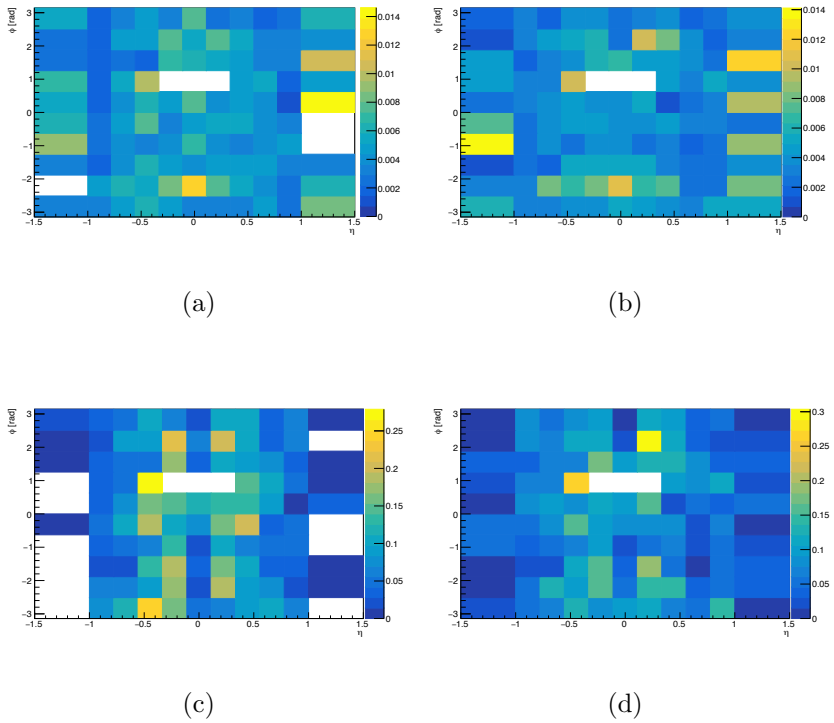

(a) (b)

(c) (d)

Figure 7.1: The distributions of (a) f_L, (b) f_S, (c) $A^L_{\mu_{MS}-\mu_{MS}}$, and (d) $A^S_{\mu_{MS}-\mu_{MS}}$ as functions of η and ϕ for the GGM selection. White bins signify that at least one of the inputs to that bin is zero.

$A^L_{\mu_{MS}-\mu_{MS}}$	7.8 ± 0.3
$A^S_{\mu_{MS}-\mu_{MS}}$	7.8 ± 0.3

Table 7.1: SR_{GGM} predictions for $\mu_{MS}-\mu_{MS}$ vertices using $\eta-\phi$ dependent transfer factors, given an integrated luminosity of 32.9 fb^{-1}. All quoted uncertainties are purely statistical.

7.1.2 p_{T} profiling

It is also important to consider any p_{T} dependence that might be lost in a global prediction. The logic of the method is given in the following equations:

$$i \in \{p_{\mathrm{T}}\}, \qquad X_i^{*L} = (X_{OS})_i^L - (X_{SS})_i^L \times R_q^X, \qquad X = B, C, D$$

$$f_i^L = \frac{B_i^{*L}}{D_i^{*L}}, \qquad f_i^S = \frac{C_i^{*S}}{D_i^{*S}}$$

$$A^L_{\mu_{MS}-\mu_{MS}} = \sum_i f_i^L C_i^{*L}, \qquad A^S_{\mu_{MS}-\mu_{MS}} = \sum_i f_i^S B_i^{*S} \tag{7.2}$$

The p_{T} distributions for the lead/subleading transfor factors and yields for SR_{Z_D} and SR_{GGM} are given in Fig. 7.2 and Fig. 7.3 respectively. The integrated yields are displayed in Tab. 7.2. The transfer factors are constant for the range of p_{T} associated with SM Z boson decay. Both predictions are consistant with each other and with the $\eta - \phi$ dependent and global predictions.

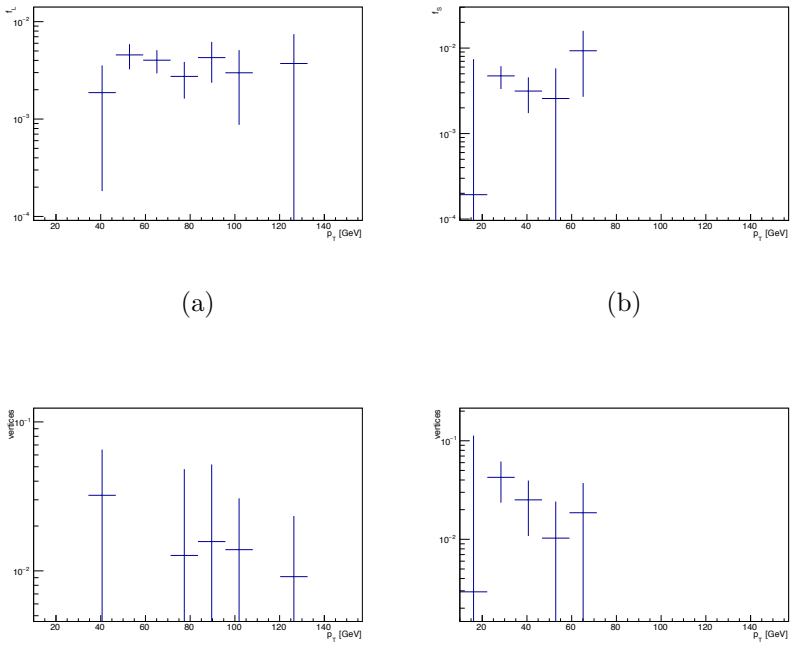

(a) (b)

(c) (d)

Figure 7.2: The distributions of (a) f_L, (b) f_S, (c) $A^L_{\mu_{MS}-\mu_{MS}}$, and (d) $A^S_{\mu_{MS}-\mu_{MS}}$ as functions of p_{T} for the Z_D selection.

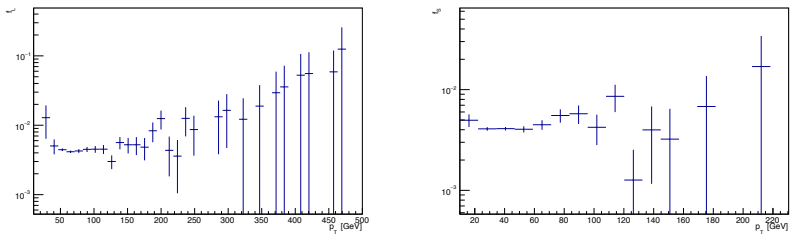

(a) (b)

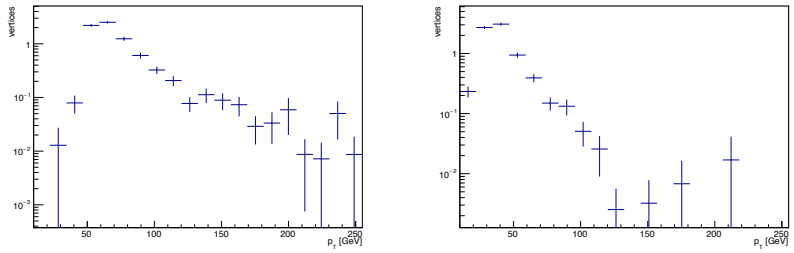

(c) (d)

Figure 7.3: The distributions of (a) f_L, (b) f_S, (c) $A^L_{\mu_{MS}-\mu_{MS}}$, and (d) $A^S_{\mu_{MS}-\mu_{MS}}$ as functions of p_{T} for the GGM selection.

Region	SR_{Z_D}	SR_{GGM}
$A^L_{\mu_{MS}-\mu_{MS}}$	0.08 ± 0.06	7.8 ± 0.3
$A^S_{\mu_{MS}-\mu_{MS}}$	0.10 ± 0.11	7.7 ± 0.3

Table 7.2: SR_{Z_D} and SR_{GGM} predictions for $\mu_{MS}-\mu_{MS}$ vertices using p_{T} dependent transfer factors, given an integrated luminosity of 32.9 fb^{-1}. All quoted uncertainties are purely statistical.

7.1.3 run profiling

We also consider any time dependence that might have resulted from degrading detector conditions over the data taking period. The logic of the method is given in the following equations:

$$i \in \{run\ number\}, \qquad X_i^* = (X_{OS})_i - (X_{SS})_i \times R_q^X, \qquad X = B, C, D$$

$$f_i^L = \frac{B_i^*}{D_i^*}, \qquad f_i^S = \frac{C_i^*}{D_i^*}$$

$$A_{\mu_{MS}-\mu_{MS}} = \sum_i f_i^L C_i^* = \sum_i f_i^S B_i^* \tag{7.3}$$

The run number distributions for the lead/subleading transfor factors and predicted number of vertices for SR_{GGM} are given in Fig. 7.4. The integrated yield is displayed in Tab. 7.3. The transfer factors are consistent thoughout all runs with the exception of one. The outlier is still within 2 σ of the nominal value, and the integrated yields agree with the nominal prediction.

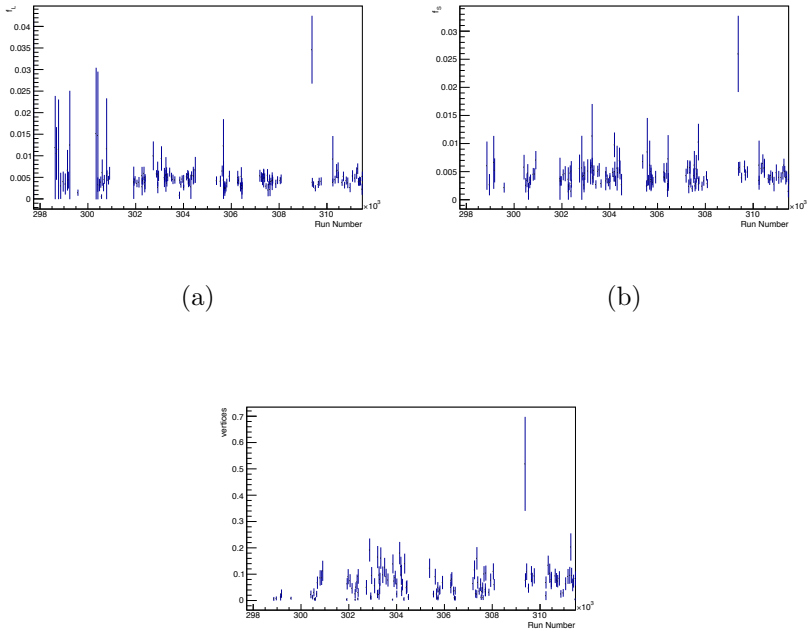

(a) (b)

(c)

Figure 7.4: The distributions of (a) f_L, (b) f_S, and (c) $A_{\mu_{MS}-\mu_{MS}}$ as functions of run number for the GGM selection.

$A_{\mu_{MS}-\mu_{MS}}$	8.3 ± 0.3

Table 7.3: SR_{GGM} predictions for $\mu_{MS} - \mu_{MS}$ vertices using run number dependent transfer factors, given an integrated luminosity of 32.9 fb^{-1}. All quoted uncertainties are purely statistical.

7.1.4 pile-up profiling

We also consider any dependence on pile-up that might affect our background prediction. The logic of the method is given in the following equations:

$$
\begin{aligned}
i \in \{pile-up\}, \qquad X_i^* = (X_{OS})_i - (X_{SS})_i \times R_q^X, \qquad X = B, C, D \\
f_i^L = \frac{B_i^*}{D_i^*}, \qquad f_i^S = \frac{C_i^*}{D_i^*} \\
A_{\mu_{MS}-\mu_{MS}} = \sum_i f_i^L C_i^* = \sum_i f_i^S B_i^* \qquad (7.4)
\end{aligned}
$$

The μ distributions for the lead/subleading transfor factors and predicted number of vertices for SR_{GGM} are given in Fig. 7.5. The integrated yield is displayed in Tab. 7.4. The transfer factors do feature a slight trend of increasing with pile-up however the impact of this trend is negligible as the integrated yield agrees with the nominal prediction.

$A_{\mu_{MS}-\mu_{MS}}$	7.8 ± 0.3

Table 7.4: SR_{GGM} predictions for $\mu_{MS} - \mu_{MS}$ vertices using pile-up dependent transfer factors, given an integrated luminosity of 32.9 fb^{-1}. All quoted uncertainties are purely statistical.

7.2 ABCD region size

The size of the ABCD regions (i.e. ΔR $>$ 0.1 or ΔR $<$ 0.1) for our prompt background estimate is based on a reasonable division between prompt and displaced

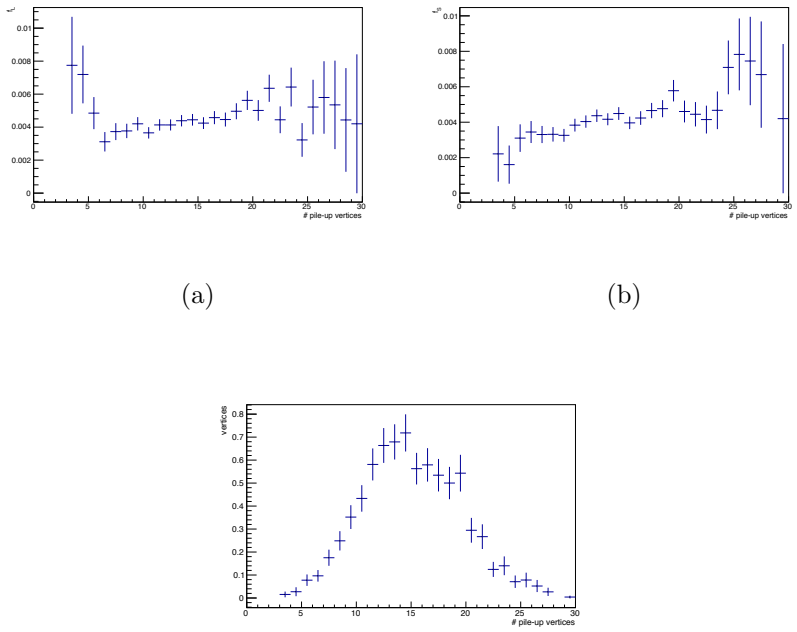

(a) (b)

(c)

Figure 7.5: The distributions of (a) f_L, (b) f_S, and (c) $A_{\mu_{MS}-\mu_{MS}}$ as functions of pile-up for the GGM selection.

vertices. It is important, however, to check that this choice does not bias the background prediction method. To do this two of the regions (either C & D or B & D) are divided in half as shown in Fig. 7.6 which gives two lead transfer factors and two subleading transfer factors. The regions are divided in a way that roughly splits the statistics in half. This procedure allows for four predictions of the prompt background in region A (i.e. either $A_{1,2} = B \times \frac{C_{1,2}}{D_{1,2}}$ or $A_{3,4} = C \times \frac{B_{3,4}}{D_{3,4}}$) which are summarized in Tab. 7.5. All four predictions are in good agreement with the nominal prediction. This validation study is only performed for the GGM selection since the prompt background is neglible for the Z_D selection.

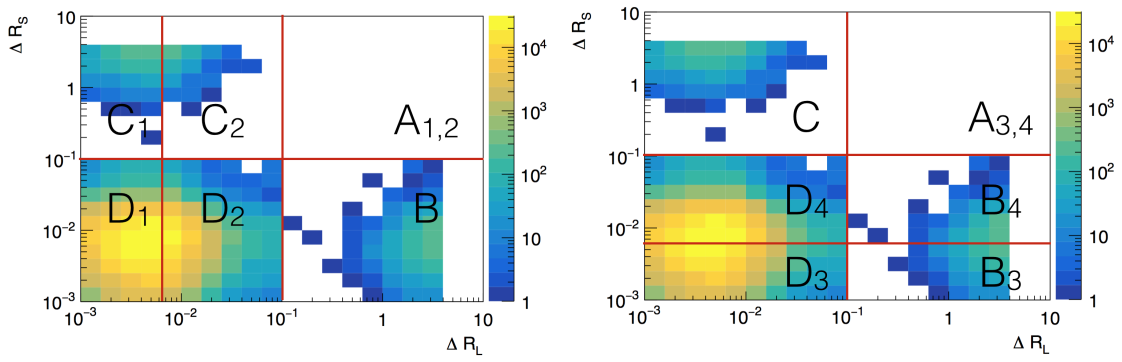

(a) $f^S_{1,2}$ (b) $f^L_{3,4}$

Figure 7.6: The distribution of displaced vertices in the ABCD plane with either regions (a) C and D or (b) B and D bisected.

Region	OS	SS	OS - $R_q\times$ SS	Region	OS	SS	OS - $R_q\times$ SS
B	1830	2	1827 ± 43	B	1830	2	1827 ± 43
C_1	1185	15	1167 ± 35	C_2	513	6	506 ± 23
D_1	282352	279	282017 ± 536	D_2	112989	128	112835 ± 337
A_1^{pred}			7.6 ± 0.3	A_2^{pred}			8.2 ± 0.4

(a) $f^S_{1,2}$

Region	OS	SS	OS - $R_q\times$ SS	Region	OS	SS	OS - $R_q\times$ SS
B_3	873	1	872 ± 30	B_4	957	1	956 ± 31
C	1698	21	1673 ± 42	C	1698	21	1673 ± 42
D_3	181888	194	181655 ± 429	D_4	213453	213	213197 ± 464
A_3^{pred}			8.0 ± 0.3	A_4^{pred}			7.5 ± 0.3

(b) $f^L_{3,4}$

Table 7.5: The BCD yields as well as region A prediction with either regions (a) C and D or (b) B and D bisected.

7.3 MC validation

As shown in App. B MC simulations are not capable of reproducing the ΔR distributions as seen in data. This is why data-driven methods are used for the background prediction. It is still important, however, to validate the consistency of the background prediction methods using our MC simulation samples.

The number of fake vertices in the SRs is predicted using the number of SS vertices passing the SR requirements and the appropriate R_q, as described in Sect. 6.1. The predicted yields for both SRs are given in Tab. 7.6. The number of prompt vertices in the SRs is predicted using the ABCD method described in Sect. 6.2. The BCD region yields as well as the predictions for region A are summarized in Tab. 7.6. The leading and subleading transfer factors used for the ABCD prediction are given in Tab. 7.7. The distribution of vertices in the ABCD plane, passing the preselection and all SR requirements except for the min(ΔR) requirement, is given for both benchmark signal model selections in Fig. 7.7.

Region	OS yield	SS yield	Fake muon estimate (= SS $\times R_q$)	Prompt muon estimate (= OS - SS $\times R_q$)	Fake + prompt muon estimate
B	50 ± 13	4.1 ± 2.0	5.2 ± 2.8	45 ± 13	
C	164 ± 16	140 ± 16	168 ± 34	-4 ± 38	
D	13497 ± 254	890 ± 56	1068 ± 190	12429 ± 317	
A	0.8 ± 0.4	1.5 ± 1.5	1.9 ± 1.9	-0.01 ± 0.14 (= B × C / D)	1.9 ± 1.9

(a) Z_D

Region	OS yield	SS yield	Fake muon estimate (= SS $\times R_q$)	Prompt muon estimate (= OS - SS $\times R_q$)	Fake + prompt muon estimate
B	984 ± 51	0.2 ± 0.2	0.3 ± 0.3	984 ± 51	
C	888 ± 44	10 ± 5.3	12 ± 6.7	876 ± 45	
D	396023 ± 918	44 ± 6.4	53 ± 12	395970 ± 918	
A	3.5 ± 2.0	0.7 ± 0.4	0.9 ± 0.5	2.2 ± 0.2 (= B × C / D)	3.1 ± 0.5

(b) GGM

Table 7.6: Yields in $Z \to \mu\mu$ MC simulation for (a) Z_D and (b) GGM selections in A,B,C, and D regions used for the prompt background prediction. The simulations are scaled to an integrated luminosity of 32.9 fb^{-1}. All quoted uncertainties are purely statistical.

	SR_{Z_D}	SR_{GGM}
$f_L(= B*/D*)$	0.0036 ± 0.0011	0.0025 ± 0.0001
$f_S(= C*/D*)$	-0.0003 ± 0.0031	0.0022 ± 0.0001

Table 7.7: The Lead and subleading transfer factors of the ABCD method are shown for both SR_{Z_D} and SR_{GGM}, using $Z \to \mu\mu$ MC simulation scaled to 32.9 fb^{-1}. All quoted uncertainties are purely statistical.

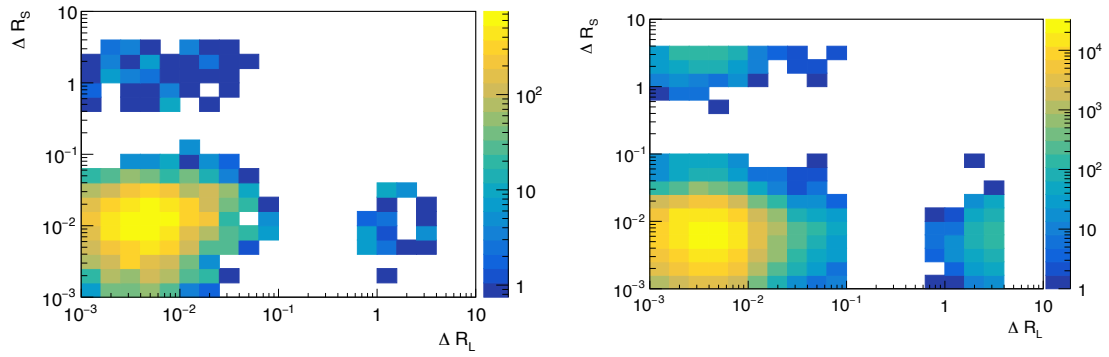

(a) (b)

Figure 7.7: $\Delta R - \Delta R$ distributions for (a) SR_{Z_D} and (b) SR_{GGM}. The distributions are shown for $Z \to \mu\mu$ MC simulation scaled to 32.9 fb^{-1}.

7.4 ABCD signal contamination

The ABCD method relies on measuring a single source of background in three control regions (i.e. BCD) to predict that sources yield in a signal region (i.e. region A). The fake background is subtracted from all of the BCD regions to leave only prompt muon background, but what about signal? For shorter LLP lifetimes a larger fraction of the signal yield from either of our benchmark models will migrate into the BCD regions and potentially affect the validity of the ABCD prediction. It is necessary to quantify the contamination for the range of signal model parameter space studied.

Region D is dominated by real prompt dimuon vertices coming from SM processes (i.e. Z+jets,etc...). For the range of signal cross sections considered the maximum contamination (i.e. $D_{sig} = 1.0 \times \sigma_{sig} \times BF \times \mathcal{L} \times \epsilon$) would be a fraction of a percent of the SM background. For any model with a cross section large enough to not be ignored, an excess should have already been observed in prompt analyses with dimuon final states. For these reasons the contamination of region D is not considered.

For the dark photon model it is shown in Sect. 6.5 that the prompt background prediction is negligible, with close to 100% uncertainty, and so the issue of Z_D signal contamination can safely be ignored in the statistical analsyis.

The total signal efficiency as a function of lifetime for the GGM SUSY model is shown in Fig. 5.11. It is negligible below 1 cm, which places a lower bound on lifetimes for which we must consider contamination. The peak is near 50 cm. The signal contamination defined as $\alpha = \frac{B_{sig}+C_{sig}}{A_{sig}+B_{sig}+C_{sig}+D_{sig}}$ is shown in Fig. 7.8 as a function of the LLP lifetime. For small lifetimes most signal events are in region D, and for large lifetimes in region A, this leaves a peak in the contamination at $\sim 32\%$ for lifetimes of $2-6$ cm. The convolution of the signal contamination and total efficiency is also given in Fig. 7.8, which shows that it is at lifetimes of ~ 10 cm that the prompt background prediction is most susceptible to contamination. For cross sections less than 1.5 pb, the contamination will be $< 1\%$, and for 15 pb the contamination will be $< 10\%$. The GGM SUSY cross sections that will be considered in the statistical analysis are at most small fractions of a pb and so signal contamination can be ignored in this analysis.

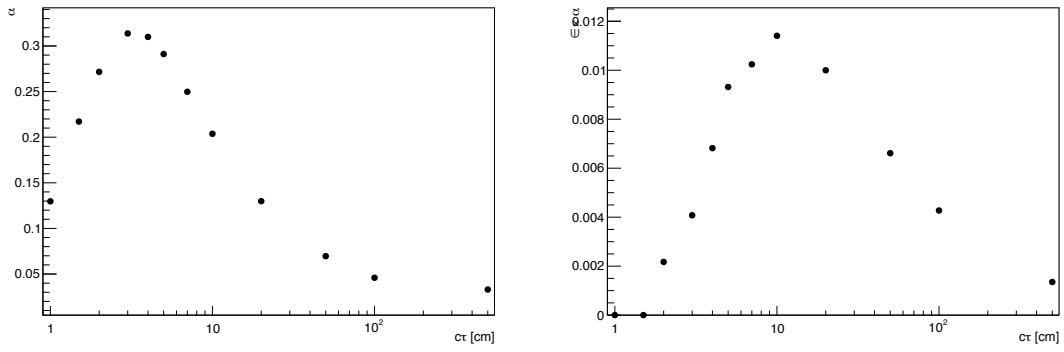

(a) (b)

Figure 7.8: Distributions of (a) signal contamination, $\alpha = \frac{B_{sig}+C_{sig}}{A_{sig}+B_{sig}+C_{sig}+D_{sig}}$, and (b) $\alpha \times \epsilon$ as functions of LLP lifetime for the GGM SUSY benchmark signal model.

CHAPTER 8

SYSTEMATIC UNCERTAINTIES

The systematic uncertainties considered in this analysis are described in detail below and a summary is given in Tab. 8.1. These uncertainties are used as nuisance parameters in the statistical analysis.

8.1 Luminosity

The uncertainty on the 2016 integrated luminosity is 2.2%. It is derived, following a methodology similar to that detailed in [63], from a preliminary calibration of the luminosity scale using x-y beam-separation scans performed in May 2016.

8.2 Pileup reweighting (PRW)

A variation in the pileup reweighting of MC is included to cover the uncertainty on the ratio between the predicted and measured inelastic cross-section in the fiducial volume defined by $M_X > 13$ GeV where M_X is the mass of the hadronic system [86]. The variation results in a systematic uncertainty of 0.2%.

8.3 Trigger and MuSA reconstruction efficiency

The trigger and reconstruction efficiencies in MC simulation will differ from those observed in data due to imperfections in the simulation procedure. When MC simulation is used in an analysis it must be corrected by trigger and reconstruction scale factors (SFs) which are defined as the ratio of the relevent efficiency in data to what is found in MC simulation ($\mathrm{SF}_i = \frac{\epsilon_i^{\mathrm{data}}}{\epsilon_i^{\mathrm{MC}}}$). The trigger/reconstruction efficiencies are easy

to calculate for MC simulation where the truth information is available. In data the trigger/reconstruction efficiency is typically calculated using a tag-and-probe method [82]. The tag-and-probe method will "tag" a $Z \to \mu\mu$ event using ID tracks, and then for one of the ID tracks it will "probe" whether or not there is a muon trigger object associated to it, or a MuSA reconstructed track, and measure the relevent efficiency.

The tag-and-probe method requires that muons have associated ID tracks, but this is not the case for displaced muons. Since MC simulation is only used in this analysis to determine signal yields, and such samples are full of displaced muons it is not possible to use the tag-and-probe method to find the trigger/reconstruction efficiencies/SFs.

The MC simulation normalization described in App. B is considered a proxy for these SFs (i.e. $SF^{Norm} \sim SF^{trig} \times SF^{reco}$). The statistical uncertainty on the normalization SF is very small (0.3%) and so a conservative systematic uncertainty of 1% is used in the statistical analysis.

8.4 Fake vertex prediction uncertainty

Fake vertices constitute a major background for the analysis, and the prediction of their yield is covered in Sect. 6.1. Part of the methodology relies on knowing R_q, the number of OS to SS vertices for a given source of fake vertices. Our background is primarily made up of two sources of which the exact composition is not known. As a result, we use the averge R_q, with a systematic uncertainty of half the deviation between the two R_q's. This results in a systematic uncertainty of 24% on the fake background prediction.

8.5 ABCD prediction uncertainty

The other primary background in the analysis arises from combined muon reconstruction inefficiency and is described in Sect. 6.2. The estimation method used

Source	Signal [%]	Background [%]
Luminosity	2.2	-
PRW	0.2	-
Trigger/Reco	1.0	-
Fake vertices	-	24
ABCD region size	-	9.1

Table 8.1: Summary of systematics evaluated in the analysis.

requires the definition of the ABCD regions. The uncertainty on this prediction is estimated by shifting the borders of the ABCD regions and comparing the result to the nominal prediction as described in Sect. 7.2. The systematic uncertainty is taken as the range of the four predictions which amounts to 9.1% of the prompt background.

CHAPTER 9

RESULTS

The yields observed in data for both SRs along with our background predictions as described in Sect. 6 are given in Tab. 9.1. While there is no indication of an excess of observed events for SR_{Z_D}, there is a large excess for SR_{GGM}. Various distributions for the vertices in SR_{Z_D} and SR_{GGM} are shown in Figs. 9.1 and 9.2 respectively.

Region	SR_{Z_D}	SR_{GGM}
$A_{\mu_{MS}-\mu_{MS}}$	0.1 ± 0.2	7.7 ± 0.3
$A_{\mu_F-\mu_X}$	14.9 ± 5.2	2.5 ± 1.9
A_{total}	15.0 ± 5.2	10.2 ± 1.9
Data	23	74

Table 9.1: Total background predictions and observed data yields for SR_{Z_D} and SR_{GGM}, given an integrated luminosity of 32.9 fb^{-1}. All quoted uncertainties are purely statistical.

9.1 SR_{GGM} Excess

It is clear from the distributions in SR_{GGM} that the excess is not due to new physics. The lead ϕ and η distributions are asymmetric with most of the vertices in a small region of the detector. The subleading distributions are more dispersed. This points to an issue with the ID that must be occuring globally to not factor in to the ABCD prediction. The invariant mass is on the Z-pole, which is predicted by the GGM model, however GGM also predicts large p_{T} for the resulting muons. The vertices in SR_{GGM} do not have significantly large muon p_{T}. Since it is evident that the excess of vertices are not coming from new physics then in order to set reasonable

limits on the GGM SUSY model something is needed to discriminate against SM Z background to bring it to negligible levels. The p_{T} distributions hint that a cut on the boost[1] of the Z should discriminate well.

Since the analysis has already been unblinded, the application of additional selection criteria is done carefully to minimize bias. The boost of the dimuon vertex in data is shown for the BCD regions of the prompt background estimate, and in region A for the GGM signal in Fig. 9.3. It is not straight forward to use a metric such as $\frac{S}{\sqrt{B}}$ to decide where the cut should be placed, since the boost distribution varies as a function of the GGM model parameters. In order to signficantly reduce the SM background (by roughly an order of magnitude) and still retain sufficient signal efficiency across the range of considered model parameters, a cut on the boost is placed at $\beta\gamma_T = 2$. This additional requirement is only placed on SR_{GGM} since the prompt background component of SR_{Z_D} is already negligible and since as the Z_D mass approachs half the higgs mass the Z_D is no longer boosted. The effect of adding the boost cut to SR_{GGM} is summarized in the following subsections:

9.1.1 Signal Efficiency

Modified vertex efficiency plots are shown in Fig. 9.4 and the modified total efficiency as a function of lifetime is shown in Fig. 9.5. The lower mass $\tilde{\chi}_1^0$ sample is affected the most by this change, as expected due to producing less boosted Z bosons. Still this has a minimal effect on the overall sensitivity given the strong background supression.

9.1.2 Background Prediction

After changing the selection criteria the background prediction for SR_{GGM} is recalculated and the fake and prompt background predictions are summarized in

[1]The transverse boost, defined as $\beta\gamma_T = \frac{p_T}{m}$, is used instead of the traditional boost.

Tab. 9.2. The transfer factors of the ABCD method are given in Tab. 9.3. The new background prediction for the GGM channel is much smaller, as anticipated, since the boost cut significantly reduces the prompt dimuon background sources.

Region	OS yield	SS yield	Fake muon estimate (= SS $\times R_q$)	Prompt muon estimate (= OS - SS $\times R_q$)	Fake + prompt muon estimate
B	117	0	0 ± 1.5	117 ± 11	
C	83	0	0 ± 1.4	83 ± 9.2	
D	19195	22	26 ± 7.1	19169 ± 139	
A	XXXX	0	0 ± 1.4	0.51 ± 0.07	0.5 ± 1.4

Table 9.2: Yields for GGM selection in regions A,B,C, and D of transfer factor method given an integrated luminosity of 32.9 fb^{-1} with additional boost requirement enforced. All quoted uncertainties are purely statistical.

f_L	0.0061 ± 0.0006
f_S	0.0043 ± 0.0005

Table 9.3: The lead and subleading transfer factors for the GGM selection, with the additional boost requirement, given an integrated luminosity of 32.9 fb^{-1}. All quoted uncertainties are purely statistical.

9.1.3 Validation

The same validation methods as presented in Sect. 7 are performed for vertices in the GGM channel with the addition of the transverse boost requirement. These validation methods consistently show that the prompt background is brought to negligible levels by the additional boost requirement.

9.1.3.1 ABCD profiling

The distributions of predicted vertices as functions of the profiled variables are given in Fig. 9.6 and the comparison of the nominal SR_{GGM} prediction with the profiled predictions are given in Tab. 9.4. The most variation is seen when profiling by the run number however it is still consistent with the nominal prediction.

A_{nom}	0.51 ± 0.07
$A^{L}_{\eta-\phi}$	0.50 ± 0.10
$A^{S}_{\eta-\phi}$	0.51 ± 0.10
$A^{L}_{p_{\mathrm{T}}}$	0.51 ± 0.08
$A^{S}_{p_{\mathrm{T}}}$	0.46 ± 0.07
$A_{pile-up}$	0.51 ± 0.08
$A_{run\ num.}$	0.61 ± 0.12

Table 9.4: SR_{GGM} predictions, with the additional boost requirement, for $\mu_{MS} - \mu_{MS}$ vertices using various profiled transfer factors, given an integrated luminosity of 32.9 fb^{-1}. All quoted uncertainties are purely statistical.

9.1.3.2 ABCD region size

The prompt background predictions formed using from various subsets of the ABCD regions are given in Tab. 9.5 for SR_{GGM} with the additional boost requirement. This procedure is used to provide a systematic uncertainty on the prompt background prediction. The value of the systematic is taken as the range of the predictions relative to the nominal prediction. Incorporating the additional boost requirement raises the uncertainty from 9.1% to 19.6%.

Region	OS	SS	OS - $R_q\times$ SS	Region	OS	SS	OS - $R_q\times$ SS
B	117	0	117 ± 11	B	117	0	117 ± 11
C_1	66	0	66 ± 8.2	C_2	17	0	17 ± 4.4
D_1	15209	17	15189 ± 123	D_2	3986	5	3980 ± 63
A_1^{pred}			0.51 ± 0.08	A_2^{pred}			0.50 ± 0.14

(a) $f^{S}_{1,2}$

Region	OS	SS	OS - $R_q\times$ SS	Region	OS	SS	OS - $R_q\times$ SS
B_3	60	0	60 ± 7.9	B_4	57	0	57 ± 7.7
C	83	0	83 ± 9.2	C	83	0	83 ± 9.2
D_3	10714	11	10701 ± 104	D_4	8481	11	8468 ± 92
A_3^{pred}			0.47 ± 0.08	A_4^{pred}			0.56 ± 0.10

(b) $f^{L}_{3,4}$

Table 9.5: The BCD yields as well as region A prediction with either regions (a) C and D or (b) B and D bisected.

9.1.3.3 MC validation

The closure test performed on $Z \to \mu\mu$ MC suffers from limited statistics. A summary of the region yields is shown in Tab. 9.6 and the distribution of MC vertices in the $\Delta R - \Delta R$ plane is given in Fig. 9.7.

Region	OS yield	SS yield	Fake muon estimate (= SS $\times R_q$)	Prompt muon estimate (= OS - SS $\times R_q$)	Fake + prompt muon estimate
B	36.15 ± 7.03	0.23 ± 0.23	0.29 ± 0.30	35.86 ± 7.04	
C	35.12 ± 8.64	0.42 ± 0.42	0.50 ± 0.51	34.62 ± 8.66	
D	15686 ± 186.1	1.99 ± 0.99	2.39 ± 1.25	15684 ± 186.10	
A	0.25 ± 0.25	< 0.001	< 0.001	0.08 ± 0.03 (= B × C / D)	0.08 ± 0.03

(a)

Table 9.6: Yields in $Z \to \mu\mu$ MC simulation for GGM selections, with additional boost requirement, in A,B,C, and D regions used for the prompt background prediction. The simulations are scaled to an integrated luminosity of 32.9 fb^{-1}. All quoted uncertainties are purely statistical.

9.2 Modified Results

With the modified background prediction for SR_{GGM} complete, the SR yields in data are again observed and shown in Tab. 9.7. Plots of the vertices in the modified SR_{GGM} are shown in Fig. 9.8.

Region	SR_{Z_D}	SR_{GGM}
$A_{\mu_{MS}-\mu_{MS}}$	0.1 ± 0.2	0.5 ± 0.1
$A_{\mu_F-\mu_X}$	14.9 ± 5.2	0 ± 1.4
A_{total}	15.0 ± 5.2	0.5 ± 1.4
Data	23	4

Table 9.7: Final background predictions and observed data yields for SR_{Z_D} and SR_{GGM}, given an integrated luminosity of 32.9 fb^{-1}. All quoted uncertainties are purely statistical.

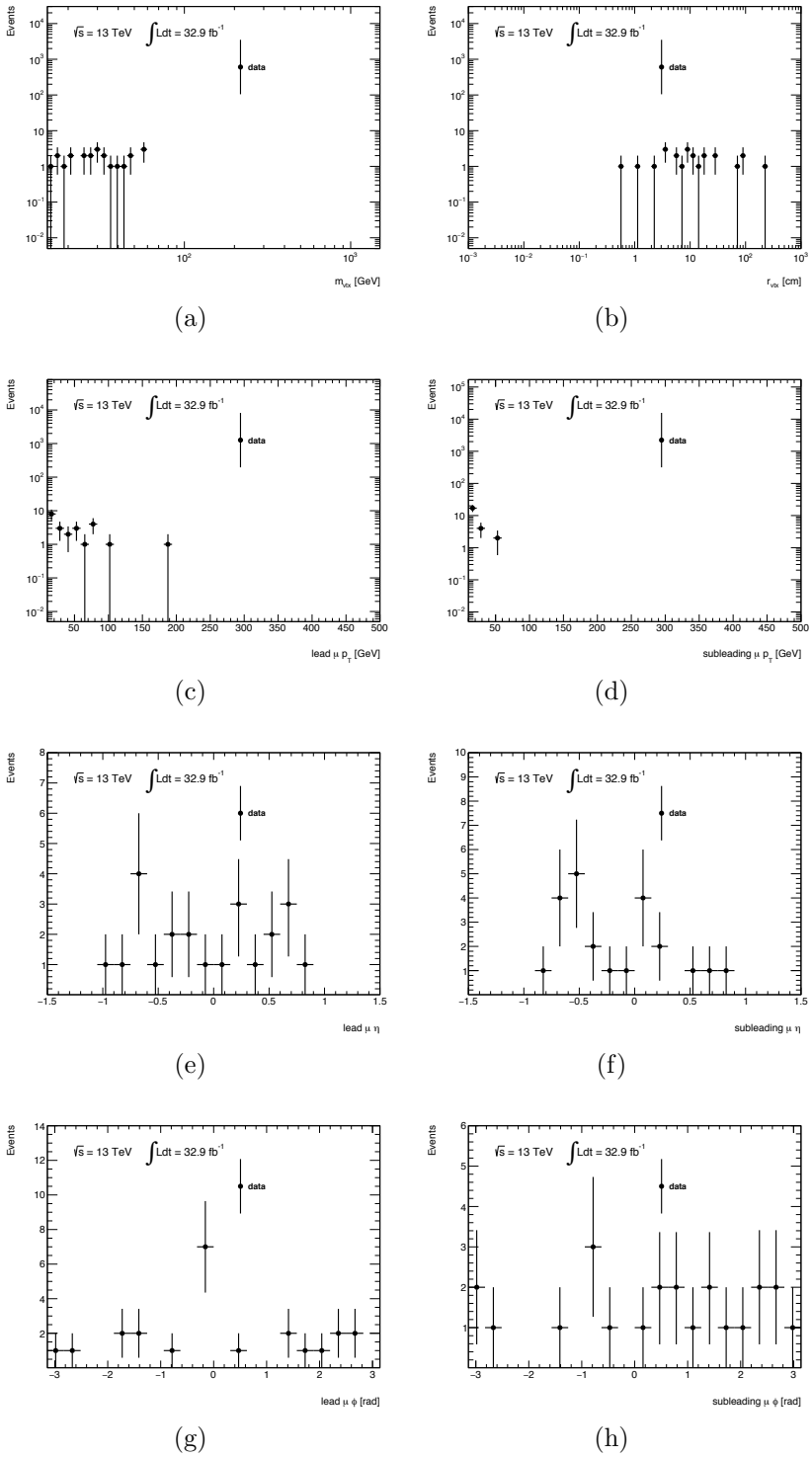

Figure 9.1: The distributions of (a) m_{ll}, (b) r_{vtx}, (c) lead μ p_{T}, (d) subleading μ p_{T}, (e) lead μ η, (f) subleading μ η, (g) lead μ ϕ, (h) subleading μ ϕ for displaced vertices passing the SR_{Z_D} selection criteria. The observed distribution in data is given by the points with error bars. The uncertainty on data is purely statistical.

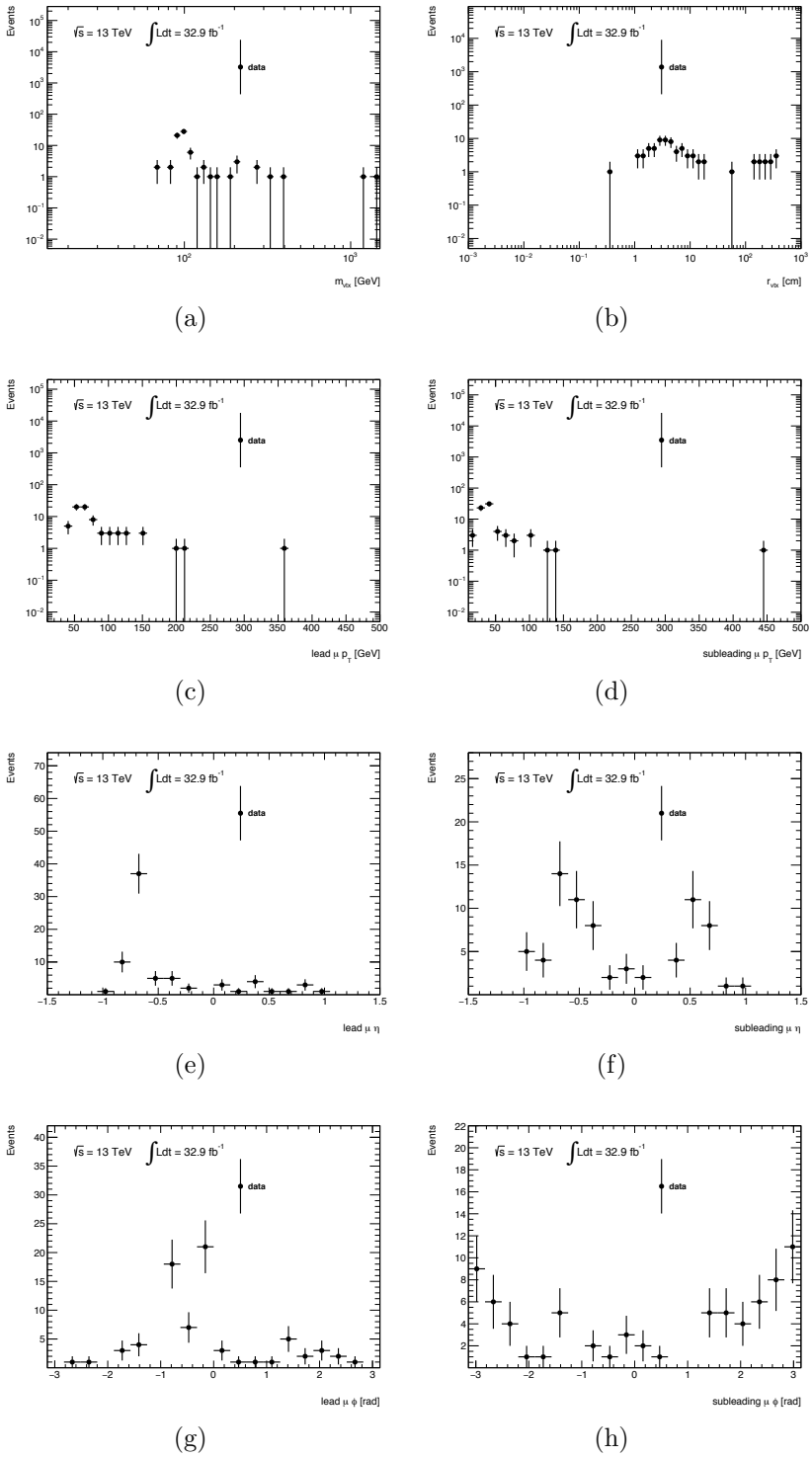

Figure 9.2: The distributions of (a) m_{ll}, (b) r_{vtx}, (c) lead μ p_{T}, (d) subleading μ p_{T}, (e) lead μ η, (f) subleading μ η, (g) lead μ ϕ, (h) subleading μ ϕ for displaced vertices passing the SR_{GGM} selection criteria. The observed distribution in data is given by the points with error bars. The uncertainty on data is purely statistical.

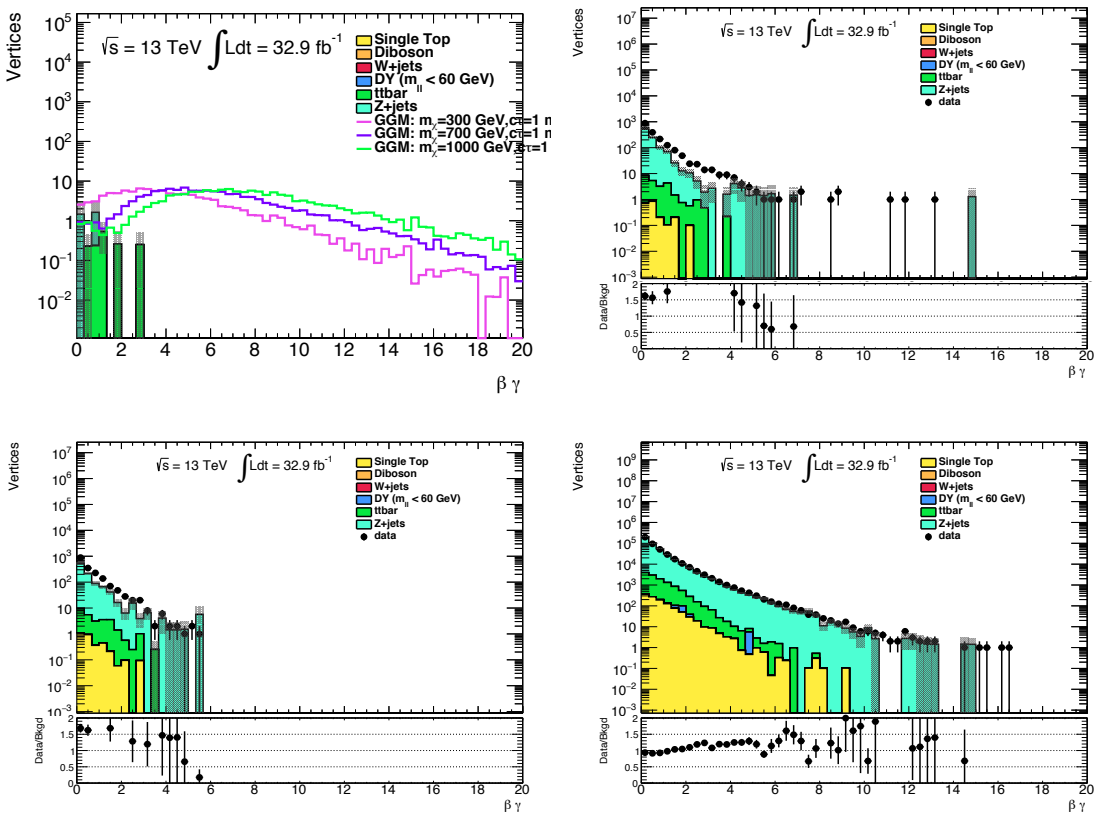

Figure 9.3: The $\beta\gamma_T$ distribution is shown for the GGM selection in regions (a) A, (b) B, (c) C, and (d) D of the transfer factor method. Only signal is shown in region A. The uncertainties shown are purely statistical.

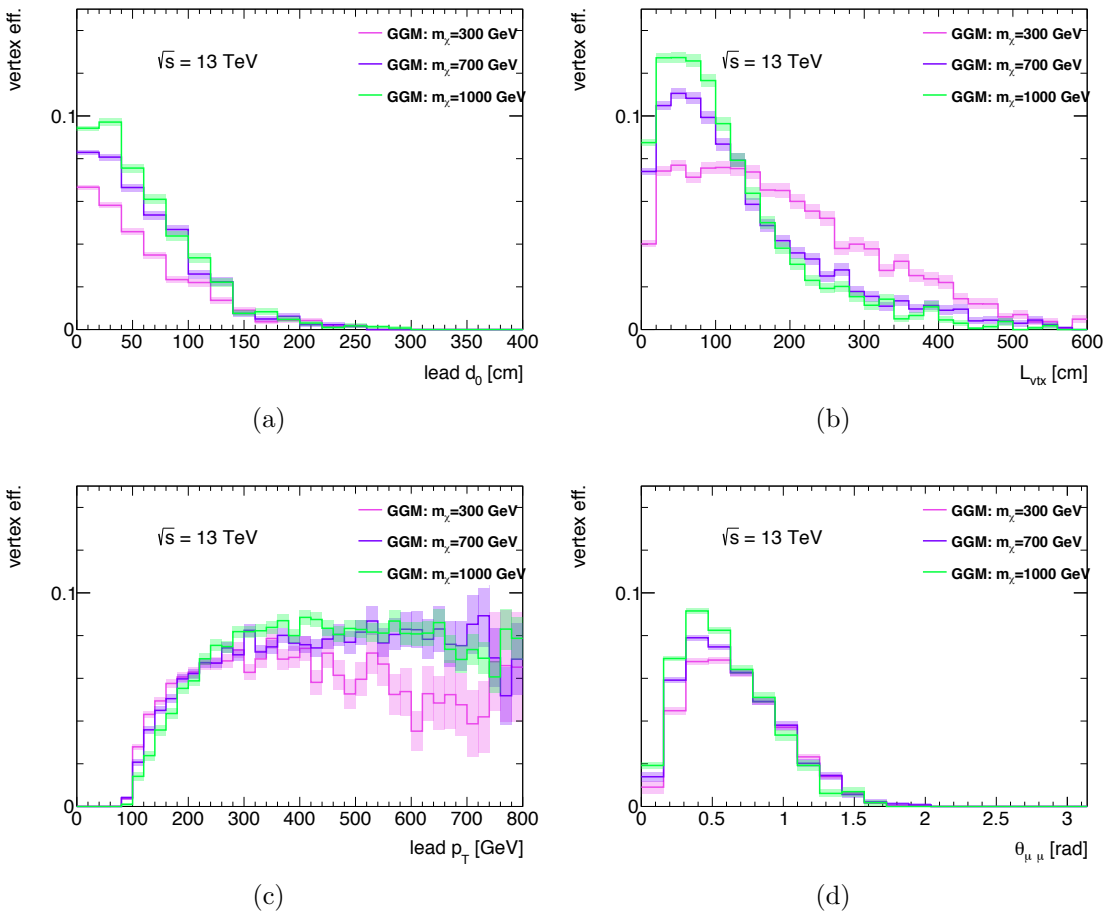

(a) (b) (c) (d)

Figure 9.4: The efficiencies to select a displaced dimuon vertex that satisfies the requirements of the SR_{GGM} as well as the discussed transverse boost cut, as function of (a) true d_0, (b) true L_{vtx}, (c) true p_{T}, and (d) the opening angle between the two muons in the vertex. These efficiencies are calculated relative to all generated signal vertices. The distributions are derived from signal events with a BSM long-lived neutralino, $\tilde{\chi}_1^0$, decaying to a Z boson (with $Z \to \mu^+\mu^-$) and a gravitino. The shaded bands represent the statistical uncertainty only.

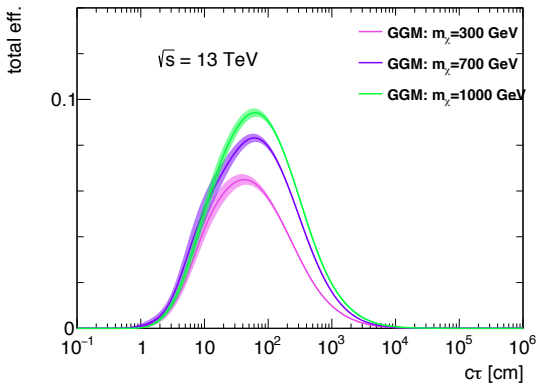

(a)

Figure 9.5: Overall efficiency (combining trigger and offline selection), as function of the lifetime of the long-lived BSM particle, $c\tau_{\mathrm{BSM}}$, for the GGM SUSY model with the addition of the transverse boost requirement. The shaded bands represent the statistical uncertainty only.

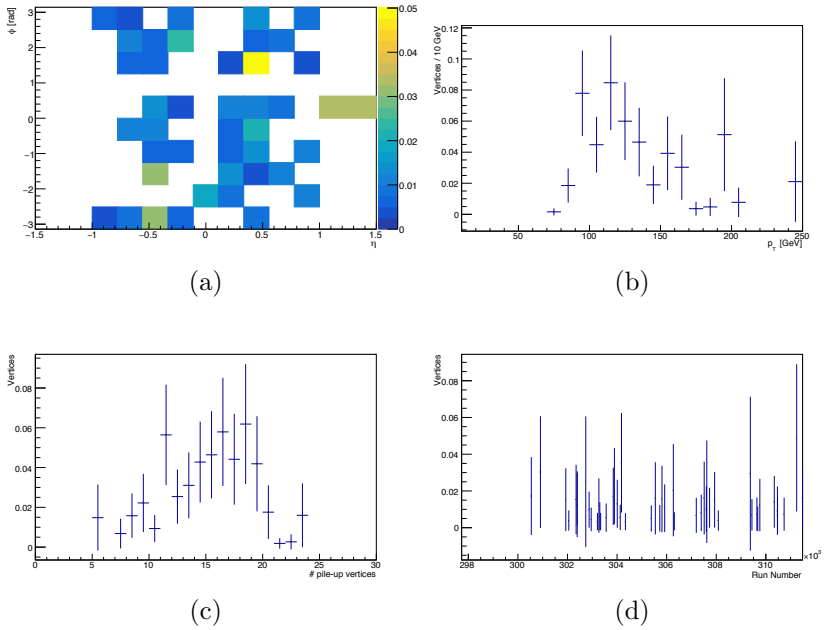

(a) (b)

(c) (d)

Figure 9.6: The distributions of (a) $A^L_{\eta-\phi}$, (b) $A^L_{p_{\mathrm{T}}}$, (c) $A_{pile-up}$, and (d) $A_{run\ num.}$ for the modified GGM selection.

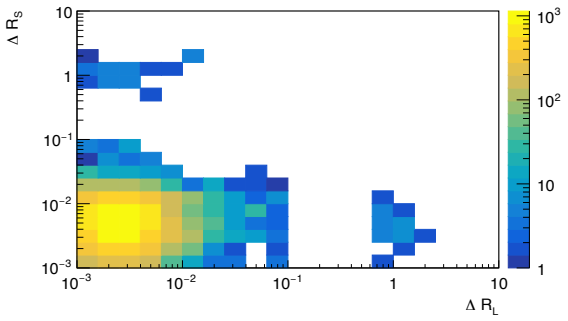

(a)

Figure 9.7: $\Delta R - \Delta R$ distributions for SR_{GGM} with additional boost requirement. The distribution is shown for $Z \to \mu\mu$ MC simulation scaled to 32.9 fb^{-1}.

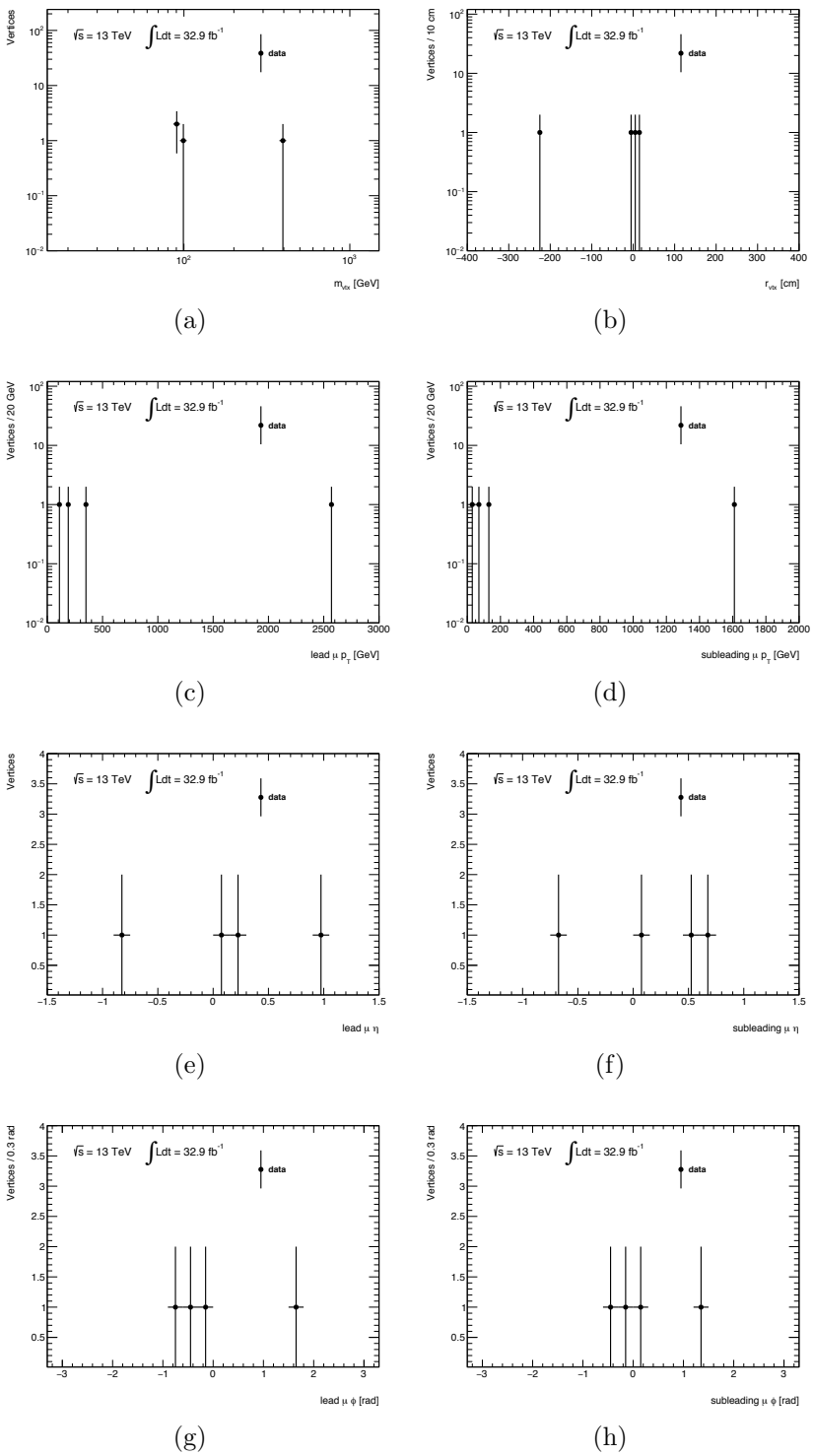

Figure 9.8: The distributions of (a) m_{ll}, (b) r_{vtx}, (c) lead μ p_{T}, (d) subleading μ p_{T}, (e) lead μ η, (f) subleading μ η, (g) lead μ ϕ, (h) subleading μ ϕ for displaced vertices passing the SR_{GGM} selection criteria. The observed distribution in data is given by the points with error bars. The uncertainty on data is purely statistical.

CHAPTER 10

INTERPRETATION

The results do not show signs of new physics and so 95 % Confidence Level (C.L.) upper limits on the cross section times branching fraction are set on our benchmark models. Limits are set using the CLs method [87, 88], which is summarized below:

- The analysis is described by a likelihood function, L(x|H), which represents the likelihood of observing data x under a given model hypothesis H. There will be two primary hypothesis: H_0, the null "background-only" hypothesis and H_1, the alternate hypothesis of "background + signal".

- A test statistic defined as $\lambda(\sigma_s) = -2\ ln\frac{L(\sigma_s,\hat{\hat{\theta}})}{L(\hat{\sigma_s},\hat{\theta})}$ is introduced to estimate how probable the observed data is w.r.t. our hypotheses. σ_s is the parameter of interest (signal cross section) and θ represents the nuisance parameters [89]. $\hat{\hat{\theta}}$ is the conditional maximum likelihood estimate (MLE)[90] of θ, and $\hat{\sigma_s}$ and $\hat{\theta}$ are the unconditional MLEs of σ_s and θ respectively.

- A range of σ_s is chosen for which the analysis is expected to have sensitivity. The test statistic is then evaluated for a number of σ_s points within the range.

- For a given σ_s, toy MC simulations are used to profile the conditional MLEs for both the null and alternate hypothesis and determine the probability distribution functions (pdfs) of the test statistic for both hypotheses, $P_{s+b}(\lambda)$ and $P_b(\lambda)$.

- Confidence Levels (CL) are defined as the probability that the test statistic is less than or equal to the value observed in data under a given hypothesis. (i.e. $CL_{s+b} = P_{s+b}(\lambda \leq \lambda_{obs})$ and $CL_b = P_b(\lambda \leq \lambda_{obs})$). Small values of CL_{s+b} favor the null hypothesis and values of CL_b close to 1 favor the alternate hypothesis.

- The CLs method uses the ratio $CL_s = \frac{CL_{s+b}}{CL_b}$ to set limits. The benefits of the CLs method can be seen in the following example: if a search channel containing a negligible amount of signal experiences a strong downward fluctation in background, then both the null and alternate hypotheses will be disfavored. Using CL_{s+b} will indicate an exlusion should be made, even though no real sensitivity exists, while CL_s will not. Although CLs lacks full frequentist coverage it only does so when there is no sensitivity. This conservative aspect makes it favorable for setting limits.

The likelihood function used in the analysis is given below:

$$\mathrm{L}(\sigma_s, w^i, \epsilon, \mathcal{L}, b_F, b_{CO}) = Poisson(N_{SR}|(\Pi_i w^i)\epsilon\sigma_s\mathcal{L}+b_F+b_{CO})\times\Pi_i\, Gauss(\tilde{w^i}|w^i, \delta_{w^i}) \times Gauss(\tilde{\epsilon}|\epsilon, \delta_\epsilon) \times Gauss(\tilde{\mathcal{L}}|\mathcal{L}, \delta_\mathcal{L}) \times Gauss(\tilde{b_F}|b_F, \delta_{b_F}) \times Gauss(\tilde{b_{CO}}|b_{CO}, \delta_{b_{CO}}) \tag{10.1}$$

σ_s is the parameter of interest (signal cross section) and the rest are nuisance parameters: w^i correspond to data/MC corrections applied to the signal MC simulation (PRW,MC normalization), ϵ is the total efficiency (trigger and reconstruction), $\mathcal{L}$ is the integrated luminosity, b_F is the number of fake background vertices, and b_P is the number of prompt background vertices. Each nuissance parameter is represented by a gaussian constraint in the likelihood, where the $\sim$ variables represent the observed value, and the other parameters represent the mean and width respectively. From a bayesian point of view these gaussian likelihoods can be thought of as priors on the parameters.

10.1 Dark photon

The ATLAS and CMS collaborations have set upper limits on the invisible branching fraction of the higgs boson [91, 92] at 0.25 and 0.24 respectively. This gives a bound on the maximum branching fraction the SM higgs boson can have to new physics, BF(H$\rightarrow Z_D Z_D$) < 0.25. Below BFs of 0.01 the analysis has no sensitivity.

The expected and observed 95 % C.L. upper limits on $\sigma \times BF$, using an integrated luminosity of 32.9 fb^{-1}, for the dark photon model are shown in Fig. 10.1 as a function of Z_D lifetime. The expected and observed $c\tau$ limits for the dark photon model are given in Tab. 10.1.

m_{Z_D}	$c\tau_{LL}^{exp}$ [cm]	$c\tau_{LL}^{obs}$ [cm]	$c\tau_{UL}^{exp}$ [cm]	$c\tau_{UL}^{obs}$ [cm]
20	0.30 ± 0.01	0.32	1877 ± 247	1572
40	0.78 ± 0.04	0.83	1450 ± 215	1215
60	1.67 ± 0.15	1.89	517 ± 81	426

(a)

m_{Z_D}	$\epsilon_{LL}^{exp}[\times 10^{-10}]$	$\epsilon_{LL}^{obs}[\times 10^{-10}]$	$\epsilon_{UL}^{exp}[\times 10^{-10}]$	$\epsilon_{UL}^{obs}[\times 10^{-10}]$
20	5.37 ± 0.35	5.86	423 ± 20	410
40	6.11 ± 0.45	6.67	263 ± 15	255
60	10.2 ± 0.81	11.3	180 ± 16	169

(b)

Table 10.1: The expected and observed limits on (a) $c\tau$ and (b) mixing parameter ϵ using $\int L = 32.9$ fb^{-1} for the low mass bench mark model. A branching fraction BF(H$\rightarrow Z_D Z_D$) $= 0.1$ is assumed and $BF(Z_D \rightarrow \mu\mu)$ is set according to the model.

10.2 GGM SUSY

The expected and observed 95 % C.L. upper limits on $\sigma \times BF$, using an integrated luminosity of 32.9 fb^{-1}, for the GGM SUSY model are shown in Fig. 10.3 as a function of the $\tilde{\chi}_1^0$ lifetime. The expected and observed $c\tau$ limits for the GGM SUSY model are given in Tab. 10.2.

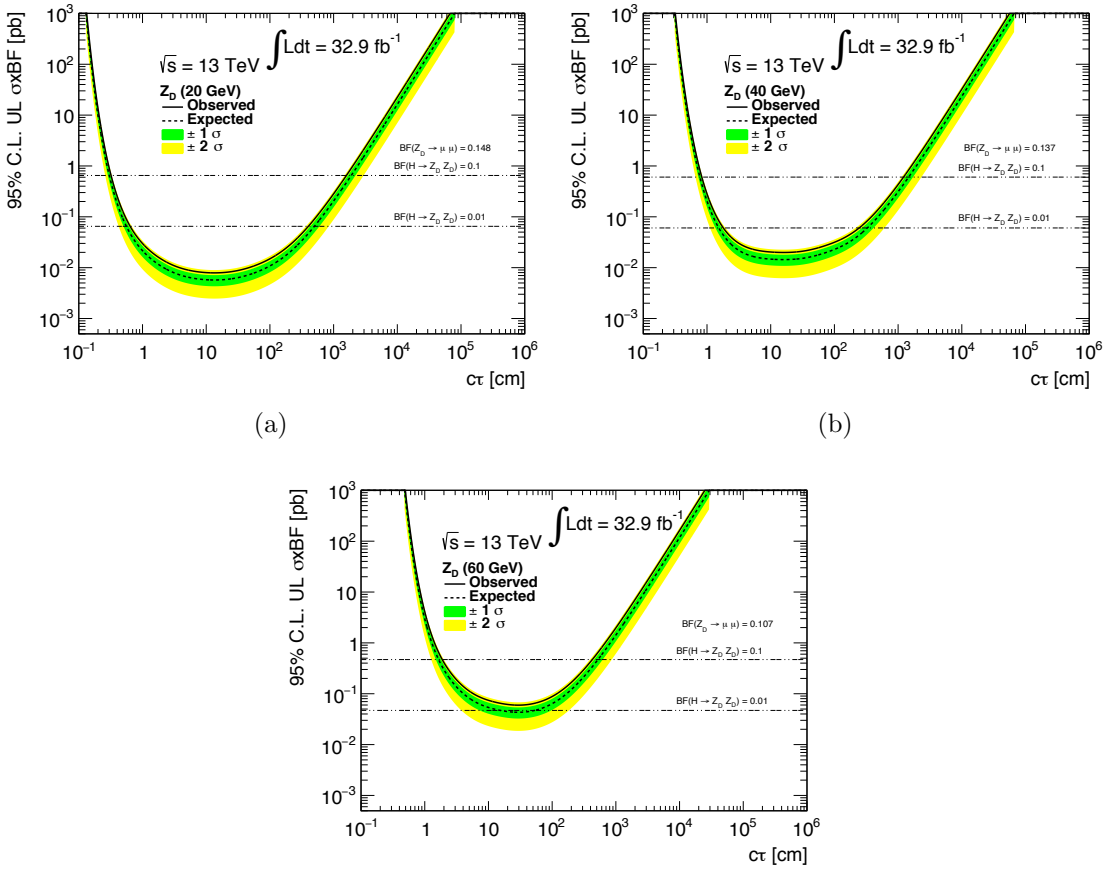

Figure 10.1: The expected and observed 95 % C.L. upper limits on $\sigma \times BF$, with $BF(Z_D \to \mu\mu)$ set by the mass/model and $\int L = 32.9$ fb^{-1}, for the low mass bench mark model with m_{Z_D}: (a) 20 GeV (b) 40 GeV or (c) 60 GeV as a function of Z_D lifetime. The shaded bands represent the statistical and systematic uncertainty. The horizontal dotted lines represent $\sigma \times BF$ with different assumptions for $BF(H \to Z_D Z_D)$.

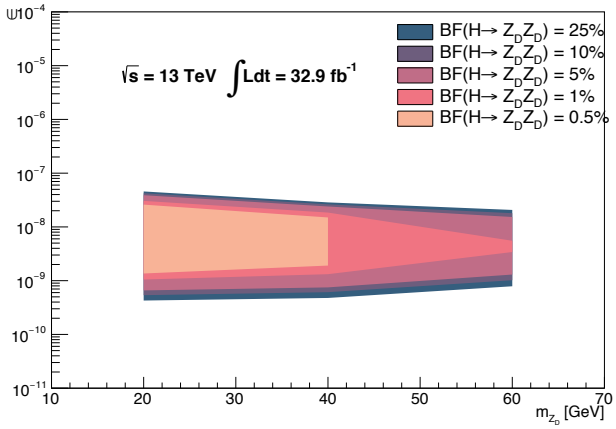

(a) expected limit

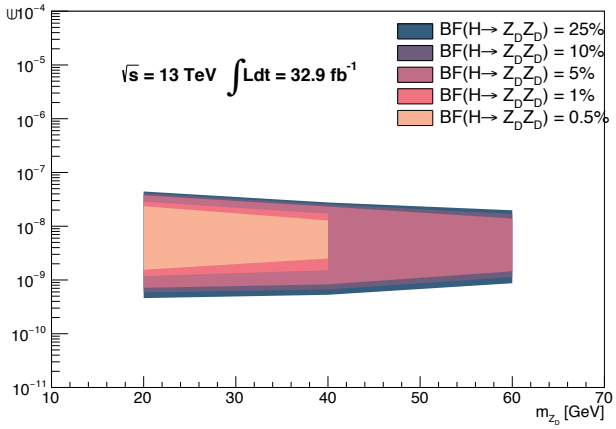

(b) observed limit

Figure 10.2: The (a) expected and (b) observed limits in the $m_{Z_D} - \epsilon_{Z_D}$ plane with an integrated luminosity $\int L = 32.9$ fb^{-1}. The contours represent different hypotheses of BF(H→ $Z_D Z_D$). $BF(Z_D \to \mu\mu)$ is mass dependent and determined by the model.

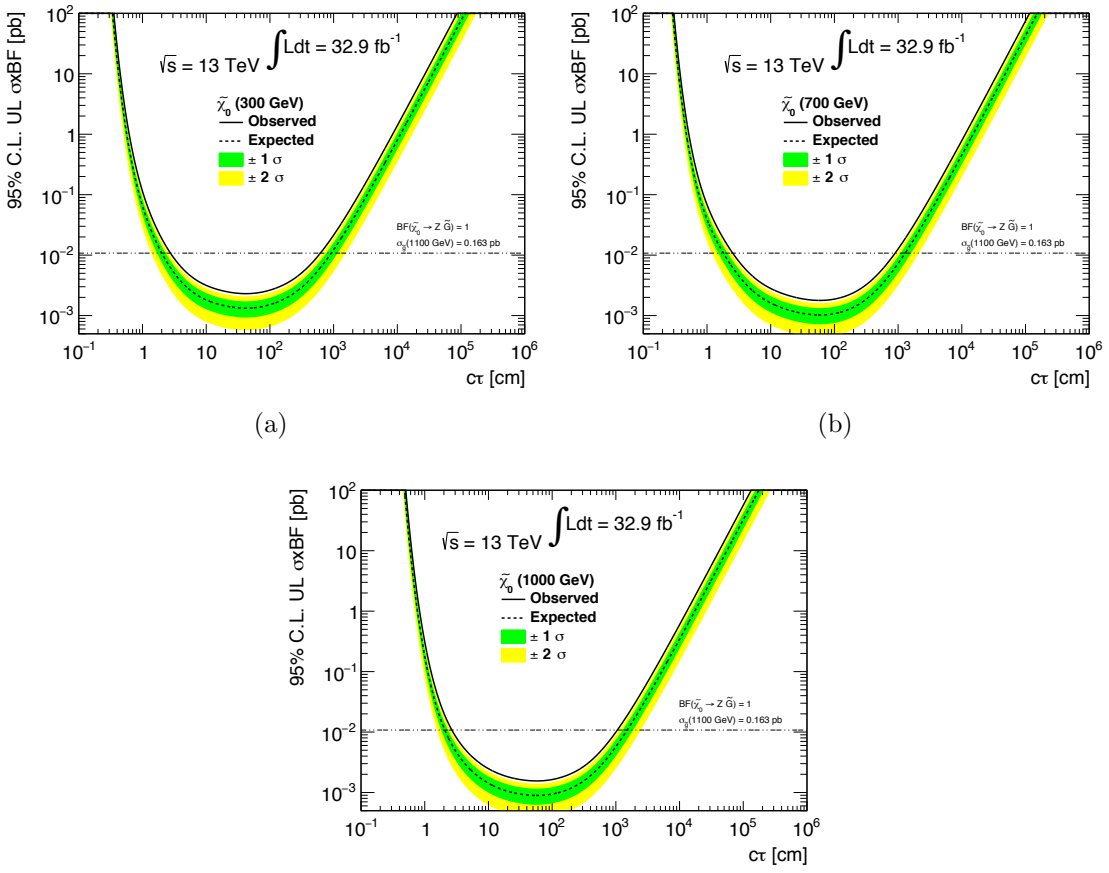

Figure 10.3: The expected and observed 95 % C.L. upper limits on $\sigma \times BF$, with $BF(\tilde{\chi}_0 \to Z\tilde{G}) = 1$ and $\int L = 32.9$ fb^{-1}, for the high mass bench mark model with $m_{\tilde{\chi}_0}$: (a) 300 GeV (b) 700 GeV or (c) 1000 GeV as a function of $\tilde{\chi}_1^0$ lifetime. The shaded bands represent the statistical and systematic uncertainty. The horizontal dotted line represents $\sigma \times BF$ with $\sigma_{\tilde{g}}(1100 \text{ GeV}) = 0.163$ pb.

$m_{\tilde{\chi}_1^0}$	$c\tau_{LL}^{\text{exp}}$ [cm]	$c\tau_{LL}^{\text{obs}}$ [cm]	$c\tau_{UL}^{\text{exp}}$ [cm]	$c\tau_{UL}^{\text{obs}}$ [cm]
300	2.02 ± 0.32	2.79	909 ± 189	617
700	1.83 ± 0.30	2.57	1275 ± 256	894
1000	2.09 ± 0.25	2.70	1498 ± 286	1050

Table 10.2: The expected and observed $c\tau$ limits using $\sigma_{\tilde{g}}(1100 \text{ GeV}) = 0.163$ pb, $BF(\tilde{\chi}_0 \to Z\tilde{G}) = 1$, and $\int L = 32.9$ fb^{-1} for the high mass bench mark model.

CHAPTER 11

CONCLUSION

A search for non-collimated displaced dimuon vertices within the ATLAS detector during the 2016 data taking period of Run II of the LHC has been presented. MuSA tracks are used to reconstruct displaced dimuon vertices which provides a much higher geometrical acceptance than with ID based DV searches. The search utilizes two benchmark signal models for interpreting the data: The "low mass" dark photon model and the "high mass" GGM SUSY model. The two primary sources of background are fake and prompt vertices. Fake vertices consist of MuSA tracks that systematically lack ID tracks, (i.e. cosmics or pion/kaon decay). Prompt vertices come from standard dimuon processes in which no ID track is present due to track finding inefficiency. Two signal selections, one for each benchmark model, are used in the statistical analysis. The low mass selection is dominated by fake vertices while the high mass selection is dominated by prompt vertices.

An excess of data over the expected background is seen in the high mass GGM channel. The majority of vertices in the excess have a lead MuSA track that falls within a very narrow region of the detector ($\eta \sim -0.7$ and $\phi \sim 0$). A back of the envelope calculation of the probability to observe such a large upward fluctuation in any region that size, assuming vertices are distributed uniformally throughout the detector, gives $p = 3.33 \times 10^{-45}$. For this reason it can safely be reasoned that the observed excess is not due to new physics, but a detector related issue. The fact that the ABCD prompt background estimation method does not predict these vertices means they are correlated in ΔR. When one MuSA track goes through the troubled

region of the detector, it is likely that the other MuSA track will lack an associated ID track. This points to a global issue affecting the ID efficiency.

Once new physics has been ruled out, exclusion limits need to be placed on regions of parameter space in the two benchmark models for which the analysis has sensitivity. The excess in the GGM channel will result in weaker limits on that model, and so another selection rule is added to require a boost of the dimuon system. With the additional cut the ABCD method confirms the prompt background has been brought to negligible levels and the observed excess disappears.

95% CL upper limits are placed on the cross section times branching fraction for both benchmark models as functions of the LLP lifetime. The limits are placed for multiple LLP mass hypotheses. The observed $c\tau$ limits for the GGM channel extend from 2.57 to 1050 cm and for the Z_D channel from 0.32 to 1572 cm. 95% CL exclusion contours are also placed in the $\epsilon - m_{Z_D}$ plane for the dark photon model.

This analysis marks the first use of MuSA tracks as primary physics objects in ATLAS. Typically the muon system is used as a means of identifying ID tracks consistent with a muon, and the superior p_{T} measurement of the ID is used in analyses. As far as long lived particle searches go, the gain in geometrical acceptence achieved by using MuSA tracks is enormous. Additionally, the poorer p_{T} resolution of MuSA tracks is not an issue for a search (as opposed to a precision measurement). What is an issue is obtaining detailed knowledge of the correlation of ID track finding efficiency for dimuon vertices. For most ATLAS analyses small gaps in ID efficiency will result in minimal efficiency loss for the analysis. However for the analysis presented, small correlated inefficiences coupled with a relatively common physics process ($Z \to \mu\mu$) will systematically add background only to the signal selection. Future iterations of the analysis will need to either, (a) develop a more detailed efficiency map of the ID tracking than what is currently available, or (b) use the ABCD method to

confirm that the selection requirements of the analysis bring the prompt background prediction to negligible levels.

APPENDIX

A Cut Flows

The selection requirements for our analysis as well as cut flows for our benchmark signal models and various non-QCD SM backgrounds are given in Tab. 11.1 − 11.5 for the Z_D selection, and Tab. 11.6 − 11.10 for the GGM selection.

selection Cut	N_{evt}	$N_{\text{evt}}^{\text{scaled}}$	ε_{rel} [%]	ε_{abs} [%]
none	99000	1469.36	1.00	1.00
Trigger	95996	1424.77	0.97	0.97
GRL & PV	95996	1424.77	1.00	0.97
> 1 MSonly tracks	48462	719.27	0.50	0.49
min p_{T}	42529	631.22	0.88	0.43
min d_0	42529	631.22	1.00	0.43
chamber removal	27803	412.65	0.65	0.28
σ_{d_0} removal	19302	286.48	0.69	0.19
fiducial volume	19242	285.59	1.00	0.19
isolation	11510	170.83	0.60	0.12
jet-muon overlap removal	10775	159.92	0.94	0.11
track separation at vertex	10095	149.83	0.94	0.10
m_{ll}	309	4.59	0.03	0.00
OS vtx	278	4.13	0.90	0.00
cosmic	278	4.13	1.00	0.00
ΔR	265	3.93	0.95	0.00

Table 11.1: Event-level selection cutflow, using the Z_D selection, for the MC-simulated SUSY GGM signal sample with $m_{\tilde{g}} = 1.1$ TeV, $c\tau_{\tilde{\chi}_1^0} = 1$m and $m_{\tilde{\chi}_1^0} = 700$ GeV. The quantities N_{evt} and $N_{\text{evt}}^{\text{scaled}}$ are the raw and scaled (to 32.9 fb^{-1}) numbers of events, respectively, selected after applying all cuts in that row and above. The quantity ε_{rel} [%] is the efficiency of the cut relative to the previous row and ε_{tot} [%] is the total efficiency, after appling all cuts up to and including that row.

selection Cut	N_{evt}	$N_{\text{evt}}^{\text{scaled}}$	ε_{rel} [%]	ε_{abs} [%]
none	198000	42731.90	1.00	1.00
Trigger	65152	14061.00	0.33	0.33
GRL & PV	65152	14061.00	1.00	0.33
> 1 MSonly tracks	42498	9171.82	0.65	0.21
min p_{T}	39190	8457.90	0.92	0.20
min d_0	39190	8457.90	1.00	0.20
chamber removal	26229	5660.68	0.67	0.13
σ_{d_0} removal	13836	2986.05	0.53	0.07
fiducial volume	13661	2948.29	0.99	0.07
isolation	9538	2058.47	0.70	0.05
jet-muon overlap removal	9419	2032.79	0.99	0.05
track separation at vertex	8643	1865.31	0.92	0.04
m_{ll}	8194	1768.41	0.95	0.04
OS vtx	8093	1746.61	0.99	0.04
cosmic	8093	1746.61	1.00	0.04
ΔR	7844	1692.87	0.97	0.04

Table 12.2: Event-level selection cutflow, using the Z_{D} selection, for the MC-simulated dark gauge boson signal sample with $m_S = 150$ GeV, $m_{Z_{\text{D}}} = 20$ GeV and $c\tau_{Z_{\text{D}}} = 0.5$m. The quantities N_{evt} and $N_{\text{evt}}^{\text{scaled}}$ are the raw and scaled (to 32.9 fb^{-1}) numbers of events, respectively, selected after applying all cuts in that row and above. The quantity ε_{rel} [%] is the efficiency of the cut relative to the previous row and ε_{tot} [%] is the total efficiency, after appling all cuts up to and including that row.

selection Cut	N_{evt}	$N_{\text{evt}}^{\text{scaled}}$	ε_{rel} [%]	ε_{abs} [%]
none	1908360	3252680.00	1.00	1.00
Trigger	1683446	2869330.00	0.88	0.88
GRL & PV	1683446	2869330.00	1.00	0.88
> 1 MSonly tracks	1241530	2116110.00	0.74	0.65
min p_{T}	1186545	2022390.00	0.96	0.62
min d_0	1186545	2022390.00	1.00	0.62
chamber removal	868662	1480580.00	0.73	0.46
σ_{d_0} removal	523776	892745.00	0.60	0.27
fiducial volume	523618	892475.00	1.00	0.27
isolation	404955	690221.00	0.77	0.21
jet-muon overlap removal	314784	536530.00	0.78	0.16
track separation at vertex	310739	529636.00	0.99	0.16
m_{ll}	1348	2297.58	0.00	0.00
OS vtx	1004	1711.26	0.74	0.00
cosmic	999	1702.74	1.00	0.00
ΔR	0	0.00	0.00	0.00

Table 12.3: Event-level selection cutflow, using the Z_{D} selection, for the MC-simulated $Z+$jets sample. The quantities N_{evt} and $N_{\text{evt}}^{\text{scaled}}$ are the raw and scaled (to 32.9 fb^{-1}) numbers of events, respectively, selected after applying all cuts in that row and above. The quantity ε_{rel} [%] is the efficiency of the cut relative to the previous row and ε_{tot} [%] is the total efficiency, after appling all cuts up to and including that row.

selection Cut	N_{evt}	$N_{\text{evt}}^{\text{scaled}}$	ε_{rel} [%]	ε_{abs} [%]
none	83420	458414.00	1.00	1.00
Trigger	34773	191086.00	0.42	0.42
GRL & PV	34773	191086.00	1.00	0.42
> 1 MSonly tracks	29573	162511.00	0.85	0.35
min p_{T}	12342	67822.40	0.42	0.15
min d_0	12342	67822.40	1.00	0.15
chamber removal	8402	46171.10	0.68	0.10
σ_{d_0} removal	3945	21678.80	0.47	0.05
fiducial volume	3944	21673.30	1.00	0.05
isolation	2300	12639.10	0.58	0.03
jet-muon overlap removal	1803	9907.94	0.78	0.02
track separation at vertex	1771	9732.09	0.98	0.02
m_{ll}	1643	9028.70	0.93	0.02
OS vtx	1618	8891.32	0.98	0.02
cosmic	1615	8874.83	1.00	0.02
ΔR	0	0.00	0.00	0.00

Table 12.4: Event-level selection cutflow, using the Z_D selection, for the MC-simulated DY sample. The quantities N_{evt} and $N_{\text{evt}}^{\text{scaled}}$ are the raw and scaled (to 32.9 fb^{-1}) numbers of events, respectively, selected after applying all cuts in that row and above. The quantity ε_{rel} [%] is the efficiency of the cut relative to the previous row and ε_{tot} [%] is the total efficiency, after appling all cuts up to and including that row.

selection Cut	N_{evt}	$N_{\text{evt}}^{\text{scaled}}$	ε_{rel} [%]	ε_{abs} [%]
none	4167729	1037960.00	1.00	1.00
Trigger	3891081	969058.00	0.93	0.93
GRL & PV	3891081	969058.00	1.00	0.93
> 1 MSonly tracks	2186745	544600.00	0.56	0.52
min p_{T}	1287150	320559.00	0.59	0.31
min d_0	1287150	320559.00	1.00	0.31
chamber removal	920469	229239.00	0.72	0.22
σ_{d_0} removal	446762	111264.00	0.49	0.11
fiducial volume	444772	110769.00	1.00	0.11
isolation	91591	22810.40	0.21	0.02
jet-muon overlap removal	63447	15801.20	0.69	0.02
track separation at vertex	62667	15607.00	0.99	0.02
m_{ll}	17283	4304.26	0.28	0.00
OS vtx	16705	4160.31	0.97	0.00
cosmic	16700	4159.07	1.00	0.00
ΔR	3	0.75	0.00	0.00

Table 12.5: Event-level selection cutflow, using the Z_D selection, for the MC-simulated $t\bar{t}$ sample. The quantities N_{evt} and $N_{\text{evt}}^{\text{scaled}}$ are the raw and scaled (to 32.9 fb^{-1}) numbers of events, respectively, selected after applying all cuts in that row and above. The quantity ε_{rel} [%] is the efficiency of the cut relative to the previous row and ε_{tot} [%] is the total efficiency, after appling all cuts up to and including that row.

selection Cut	N_{evt}	$N_{\text{evt}}^{\text{scaled}}$	ε_{rel} [%]	ε_{abs} [%]
none	99000	1469.36	1.00	1.00
Trigger	95996	1424.77	0.97	0.97
GRL & PV	95996	1424.77	1.00	0.97
> 1 MSonly tracks	48462	719.27	0.50	0.49
min p_{T}	37296	553.55	0.77	0.38
min d_0	37296	553.55	1.00	0.38
chamber removal	24027	356.61	0.64	0.24
σ_{d_0} removal	16988	252.14	0.71	0.17
fiducial volume	16944	251.48	1.00	0.17
isolation	10853	161.08	0.64	0.11
jet-muon overlap removal	10274	152.49	0.95	0.10
track separation at vertex	9651	143.24	0.94	0.10
m_{ll}	9399	139.50	0.97	0.09
OS vtx	9327	138.43	0.99	0.09
cosmic	9327	138.43	1.00	0.09
ΔR	8423	125.01	0.90	0.09

Table 12.6: Event-level selection cutflow, using the GGM selection, for the MC-simulated SUSY GGM signal sample with $m_{\tilde{g}} = 1.1$ TeV, $c\tau_{\tilde{\chi}_1^0} = 1$m and $m_{\tilde{\chi}_1^0} = 700$ GeV. The quantities N_{evt} and $N_{\text{evt}}^{\text{scaled}}$ are the raw and scaled (to 32.9 fb^{-1}) numbers of events, respectively, selected after applying all cuts in that row and above. The quantity ε_{rel} [%] is the efficiency of the cut relative to the previous row and ε_{tot} [%] is the total efficiency, after appling all cuts up to and including that row.

selection Cut	N_{evt}	$N_{\text{evt}}^{\text{scaled}}$	ε_{rel} [%]	ε_{abs} [%]
none	198000	42731.90	1.00	1.00
Trigger	65152	14061.00	0.33	0.33
GRL & PV	65152	14061.00	1.00	0.33
> 1 MSonly tracks	42498	9171.82	0.65	0.21
min p_{T}	26067	5625.72	0.61	0.13
min d_0	26067	5625.72	1.00	0.13
chamber removal	17043	3678.18	0.65	0.09
σ_{d_0} removal	8948	1931.14	0.53	0.05
fiducial volume	8788	1896.61	0.98	0.04
isolation	6585	1421.16	0.75	0.03
jet-muon overlap removal	6502	1403.25	0.99	0.03
track separation at vertex	5915	1276.56	0.91	0.03
m_{ll}	604	130.35	0.10	0.00
OS vtx	332	71.65	0.55	0.00
cosmic	331	71.44	1.00	0.00
ΔR	286	61.72	0.86	0.00

Table 12.7: Event-level selection cutflow, using the GGM selection, for the MC-simulated dark gauge boson signal sample with $m_S = 150$ GeV, $m_{Z_{\text{D}}} = 20$ GeV and $c\tau_{Z_{\text{D}}} = 0.5$m. The quantities N_{evt} and $N_{\text{evt}}^{\text{scaled}}$ are the raw and scaled (to 32.9 fb^{-1}) numbers of events, respectively, selected after applying all cuts in that row and above. The quantity ε_{rel} [%] is the efficiency of the cut relative to the previous row and ε_{tot} [%] is the total efficiency, after appling all cuts up to and including that row.

selection Cut	N_{evt}	$N_{\text{evt}}^{\text{scaled}}$	ε_{rel} [%]	ε_{abs} [%]
none	1908360	3252680.00	1.00	1.00
Trigger	1683446	2869330.00	0.88	0.88
GRL & PV	1683446	2869330.00	1.00	0.88
> 1 MSonly tracks	1241530	2116110.00	0.74	0.65
min p_{T}	1023684	1744810.00	0.82	0.54
min d_0	1023684	1744810.00	1.00	0.54
chamber removal	749143	1276870.00	0.73	0.39
σ_{d_0} removal	482961	823178.00	0.64	0.25
fiducial volume	482844	822978.00	1.00	0.25
isolation	382934	652688.00	0.79	0.20
jet-muon overlap removal	298916	509484.00	0.78	0.16
track separation at vertex	295093	502968.00	0.99	0.15
m_{ll}	294884	502612.00	1.00	0.15
OS vtx	294872	502592.00	1.00	0.15
cosmic	292911	499249.00	0.99	0.15
ΔR	2	3.41	0.00	0.00

Table 12.8: Event-level selection cutflow, using the GGM selection, for the MC-simulated $Z+$jets sample. The quantities N_{evt} and $N_{\text{evt}}^{\text{scaled}}$ are the raw and scaled (to 32.9 fb^{-1}) numbers of events, respectively, selected after applying all cuts in that row and above. The quantity ε_{rel} [%] is the efficiency of the cut relative to the previous row and ε_{tot} [%] is the total efficiency, after appling all cuts up to and including that row.

selection Cut	N_{evt}	$N_{\text{evt}}^{\text{scaled}}$	ε_{rel} [%]	ε_{abs} [%]
none	83420	458414.00	1.00	1.00
Trigger	34773	191086.00	0.42	0.42
GRL & PV	34773	191086.00	1.00	0.42
> 1 MSonly tracks	29573	162511.00	0.85	0.35
min p_{T}	4302	23640.60	0.15	0.05
min d_0	4302	23640.60	1.00	0.05
chamber removal	3009	16535.20	0.70	0.04
σ_{d_0} removal	1444	7935.14	0.48	0.02
fiducial volume	1444	7935.14	1.00	0.02
isolation	867	4764.38	0.60	0.01
jet-muon overlap removal	697	3830.19	0.80	0.01
track separation at vertex	688	3780.73	0.99	0.01
m_{ll}	18	98.91	0.03	0.00
OS vtx	18	98.91	1.00	0.00
cosmic	18	98.91	1.00	0.00
ΔR	0	0.00	0.00	0.00

Table 12.9: Event-level selection cutflow, using the GGM selection, for the MC-simulated DY sample. The quantities N_{evt} and $N_{\text{evt}}^{\text{scaled}}$ are the raw and scaled (to 32.9 fb^{-1}) numbers of events, respectively, selected after applying all cuts in that row and above. The quantity ε_{rel} [%] is the efficiency of the cut relative to the previous row and ε_{tot} [%] is the total efficiency, after appling all cuts up to and including that row.

selection Cut	N_{evt}	$N_{\text{evt}}^{\text{scaled}}$	ε_{rel} [%]	ε_{abs} [%]
none	4167729	1037960.00	1.00	1.00
Trigger	3891081	969058.00	0.93	0.93
GRL & PV	3891081	969058.00	1.00	0.93
> 1 MSonly tracks	2186745	544600.00	0.56	0.52
min p_{T}	647743	161318.00	0.30	0.16
min d_0	647743	161318.00	1.00	0.16
chamber removal	457189	113861.00	0.71	0.11
σ_{d_0} removal	221849	55250.60	0.49	0.05
fiducial volume	221117	55068.30	1.00	0.05
isolation	71741	17866.80	0.32	0.02
jet-muon overlap removal	51919	12930.20	0.72	0.01
track separation at vertex	51300	12776.10	0.99	0.01
m_{ll}	41320	10290.60	0.81	0.01
OS vtx	41222	10266.20	1.00	0.01
cosmic	41009	10213.10	0.99	0.01
ΔR	3	0.75	0.00	0.00

Table 12.10: Event-level selection cutflow, using the GGM selection, for the MC-simulated $t\bar{t}$ sample. The quantities N_{evt} and $N_{\text{evt}}^{\text{scaled}}$ are the raw and scaled (to 32.9 fb^{-1}) numbers of events, respectively, selected after applying all cuts in that row and above. The quantity ε_{rel} [%] is the efficiency of the cut relative to the previous row and ε_{tot} [%] is the total efficiency, after appling all cuts up to and including that row.

B MC normalization

MC simulations are used sparingly in the analysis, however global discrepancies between the MC simulated events and data exist and must be corrected. These discrepancies are primarily due to trigger and reconstruction efficiency mismodelling in simulation. A SF correction is found by taking the ratio of data to Z+jets MC simulation, with the preselection requirements applied, the SR min(ΔR) cut inverted, and the requirement that $70 < m_{ll} < 100$ GeV, as shown below.

$$\mathrm{SF_Z} = \frac{N_{\mathrm{data}} - \Sigma N_{i,\text{non-Z+jets}}}{N_{\text{Z+jets}}} \tag{12.1}$$

The non-Z+jets component of the data is removed using the MC predictions from all available non-Z+jets samples. All MC simulation samples receive the same normalization SF. It is not possible to create selections that isolate the other SM backgrounds well enough to derive accurate SFs. Additionally the minor SM backgrounds account for less than 1% of the total SM background in the selection used for normalization.

The resulting SF from this normalization procedure is given in Tab. 12.11. A comparison of the m_{ll} distribution before and after normalization is given in Fig. 12.1. The excess in data for $m_{ll} < 60$ GeV is consistant in magnitude and location with QCD multijet events. Any further use of the above discussed MC simulation samples refers to their normalized predictions. Various normalized distributions in $\mathrm{CR_{SM}}$ are shown for both data and MC simulation in Fig. 12.2. Discrepancies between data and MC simulation support the need for a data-driven background estimate.

Dataset	normalization range	SF
Z+jets	$70 < m_{ll} < 100$ GeV	0.888 ± 0.003

Table 12.11: The ratio between data and MC (SF) is given for the Z+jet MC dataset. The preselection requirements are applied, the min(ΔR) requirement is inverted and an additional requirement that $70 < m_{ll} < 100$ GeV is used for all events considered. The ratio is derived using 32.9 fb^{-1}. The quoted uncertainty is purely statistical.

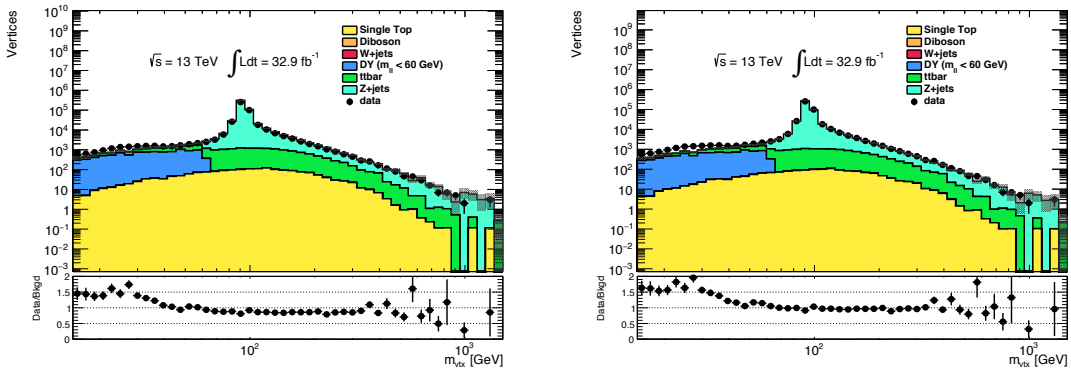

Figure 12.1: Comparison of the m_{ll} distribution (a) before, and (b) after normalization for vertices passing preselection with the SR min(ΔR) requirement inverted. The uncertainties on data and MC simulation are purely statistical.

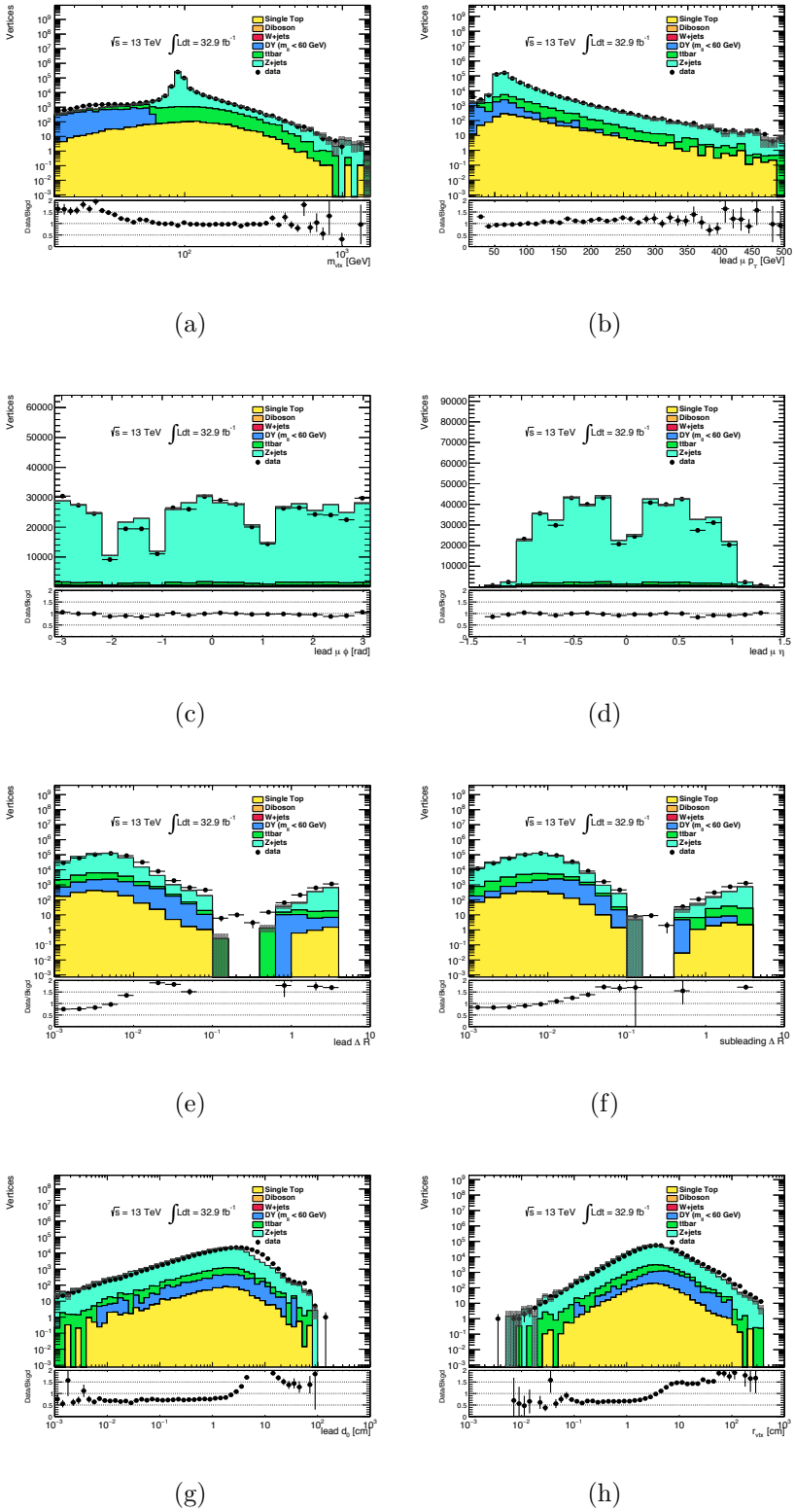

(a) (b)

(c) (d)

(e) (f)

(g) (h)

Figure 12.2: The normalized distributions of (a) m_{ll}, (b) lead μ p_T, (c) lead μ ϕ, (d) lead μ η, (e) lead μ Δ R, (f) subleading μ Δ R, (g) lead μ d_0, and (h) r_{vtx} for displaced vertices passing preselection with the SR min(ΔR) requirement inverted. The uncertainties on data and MC simulation are purely statistical.

C Signal truth distributions

The truth level distributions of d_0, L_{vtx}, p_{T}, and the opening angle between the two muons in the vertex are given in Fig. 12.3, for the dark photon model, and Fig. 12.4, for the GGM SUSY model.

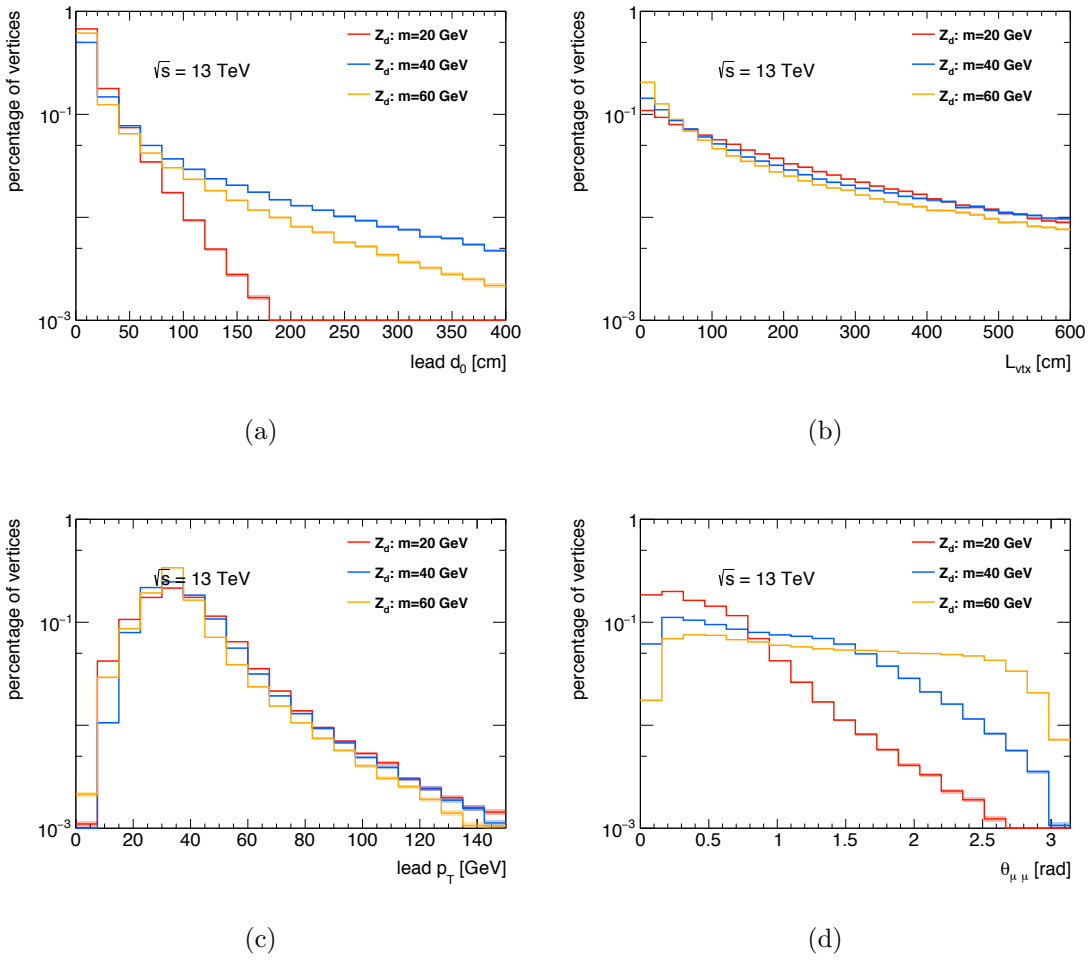

Figure 12.3: The truth level distribution for (a) d_0, (b) L_{vtx}, (c) p_{T}, and (d) the opening angle between the two muons in the vertex. The distributions are derived from signal events with a BSM long-lived dark gauge boson, Z_{D}, that decays to $\mu^+\mu^-$. The shaded bands represent the statistical uncertainty only.

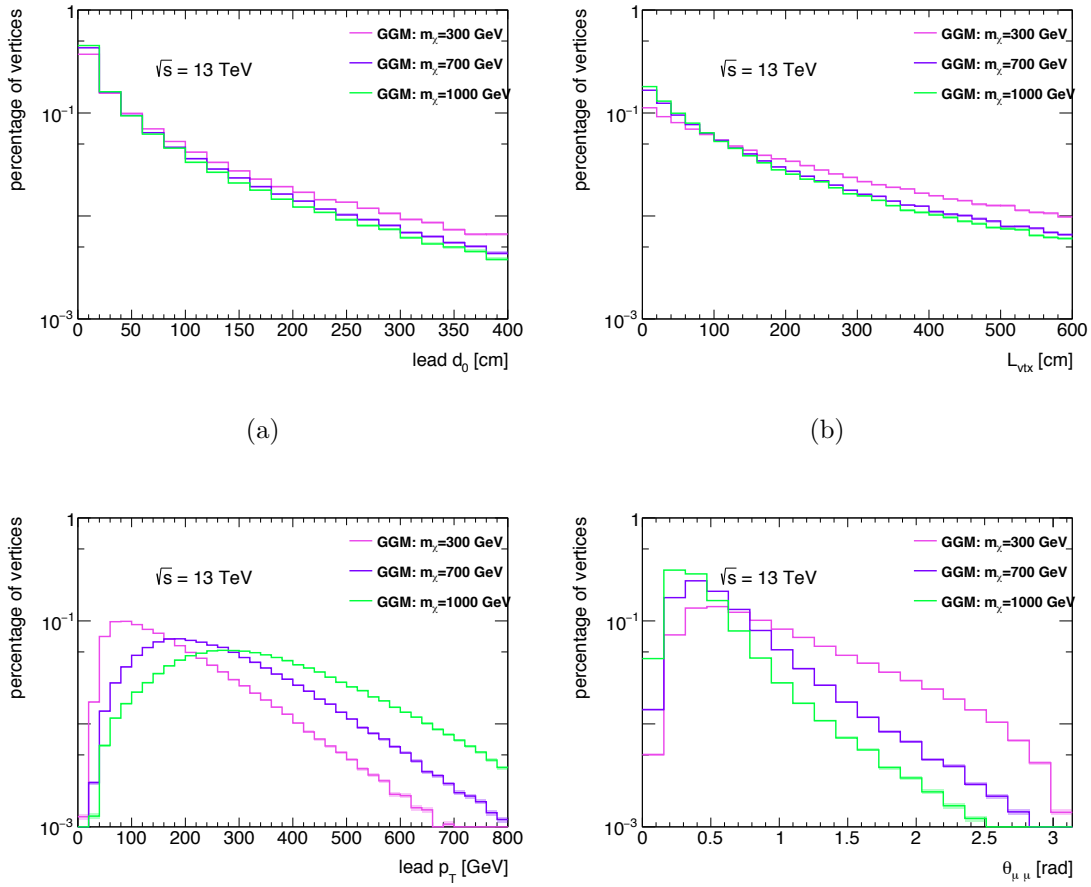

(a) (b)

(c) (d)

Figure 12.4: The truth level distribution for (a) d_0, (b) L_{vtx}, (c) p_{T}, and (d) the opening angle between the two muons in the vertex. The distributions are derived from signal events with a BSM long-lived neutralino, $\tilde{\chi}_1^0$, decaying to a Z boson (with $Z \to \mu^+\mu^-$) and a gravitino. The shaded bands represent the statistical uncertainty only.

D Diagonal covariance matrix elements

The covariance matrix expresses the uncertainties on a set of track parameters, and is crucial in understanding their quality. Our primary physics objects are MuSA tracks, whose track parameters and corresponding covariance matrix are given with respect to a point in the inner most station of the MS. Both the track parameters and covariance matrix are propagated inward until they are expressed with respect to the IP. The original and extrapolated diagonal covariance elements are displayed in Fig. 12.5 and Fig. 12.6 for the barrel and endcap respectively. In the barrel the uncertainties are as one would expect (i.e. they have reasonable original values, which then spread during extrapolation.) In the endcap however the original values for σ_{d_0} have obviously unphysical values. It is not clear what is the cause of this, but it is beyond the scope of this analysis. For this reason a cut of $\sigma_{d_0} < 20$ cm is used to maintain the quality of tracks used in the analysis.

In our analysis, extrapolation of MuSA tracks is done privately, however this is also done as part of the nominal muon reconstruction chain for pointing tracks (so called exMuSA). The diagonal covariance elements for exMuSA tracks are displayed in Fig. 12.7 and Fig. 12.8 for the barrel and endcap respectively. In both regions, there are large spikes for the σ_{d_0}. This implies that when the covariance elements for a MS track are unphysically large they are artificially set to a small value (0.5992).

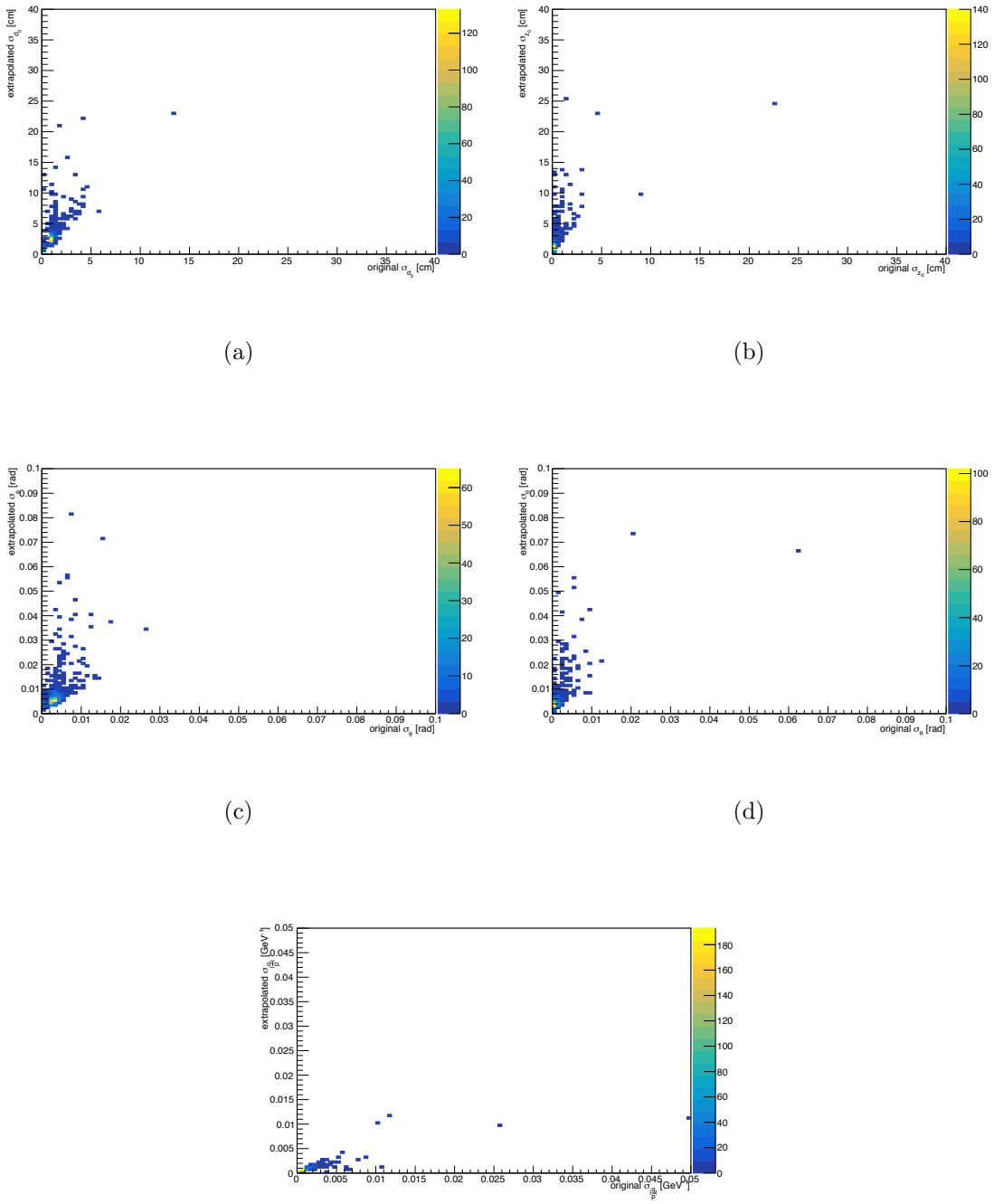

Figure 12.5: The two dimensional distributions of (a) σ_{d_0}, (b) σ_{z_0}, (c) σ_ϕ, (d) σ_θ, and (e) $\sigma_{\frac{q}{|P|}}$ are shown for tracks in the barrel with the unextrapolated value on the x-axis and the extrapolated value on the y-axis. The distributions are derived from Z+jets events.

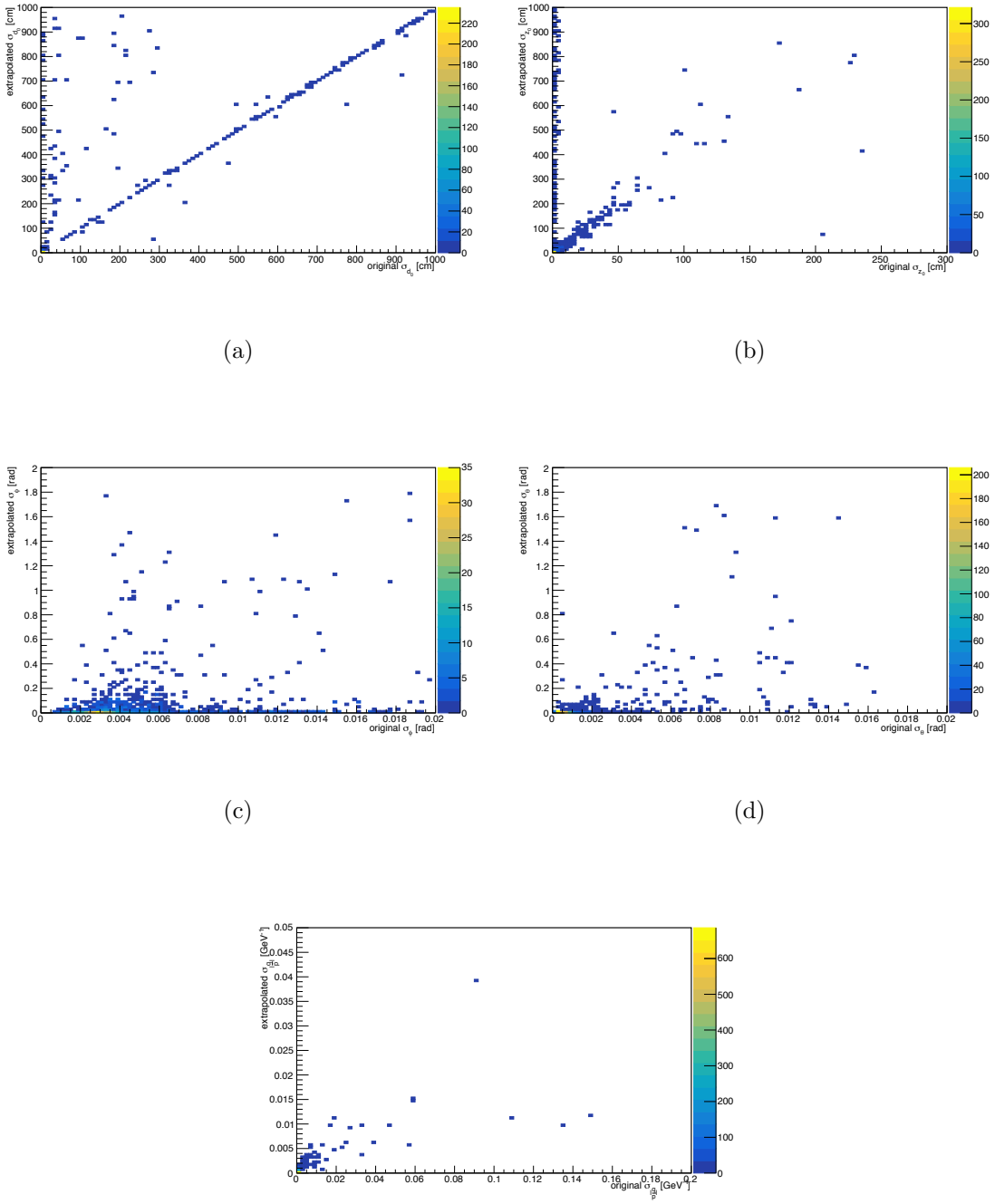

(a) (b)

(c) (d)

(e)

Figure 12.6: The two dimensional distributions of (a) σ_{d_0}, (b) σ_{z_0}, (c) σ_ϕ, (d) σ_θ, and (e) $\sigma_{\frac{q}{|P|}}$ are shown for tracks in the endcap with the unextrapolated value on the x-axis and the extrapolated value on the y-axis. The distributions are derived from Z+jets events.

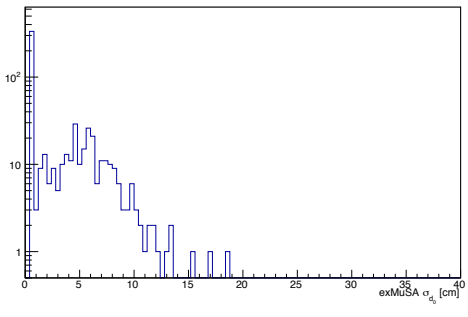

(a)

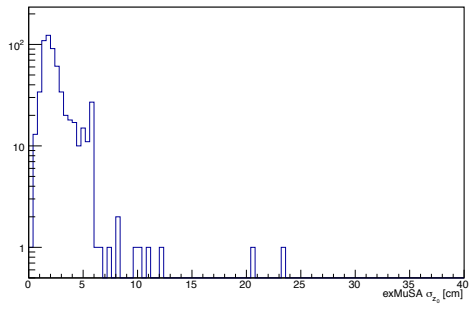

(b)

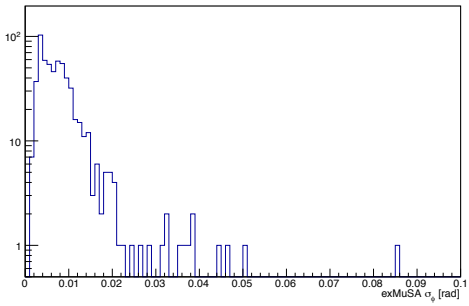

(c)

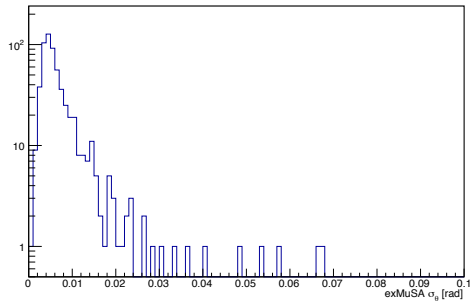

(d)

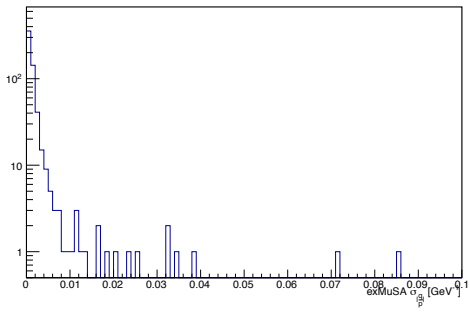

(e)

Figure 12.7: Distributions of (a) σ_{d_0}, (b) σ_{z_0}, (c) σ_{ϕ}, (d) σ_{θ}, and (e) $\sigma_{\frac{q}{|P|}}$ are shown for exMuSA tracks in the barrel. The distributions are derived from Z+jets events.

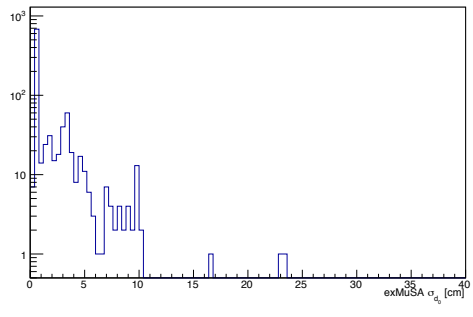

(a)

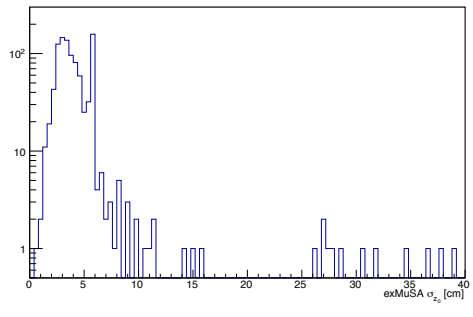

(b)

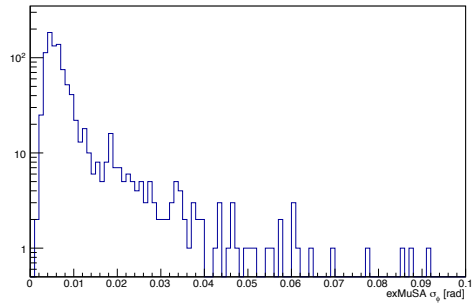

(c)

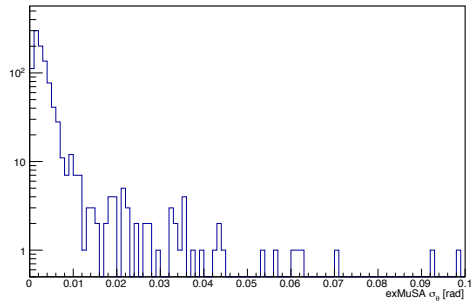

(d)

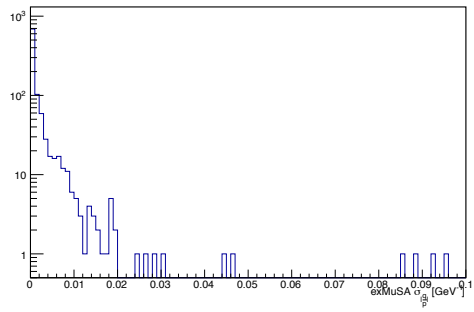

(e)

Figure 12.8: Distributions of (a) σ_{d_0}, (b) σ_{z_0}, (c) σ_{ϕ}, (d) σ_{θ}, and (e) $\sigma_{\frac{q}{|P|}}$ are shown for exMuSA tracks in the endcap. The distributions are derived from Z+jets events.

BIBLIOGRAPHY

[1] ATLAS Collaboration.
"The ATLAS Experiment at the CERN Large Hadron Collider".
In: *JINST* 3 (2008), S08003. DOI: 10.1088/1748-0221/3/08/S08003.

[2] CMS Collaboration. "The CMS Experiment at the CERN LHC".
In: *JINST* 3 (2008), S08004.

[3] S. L. Glashow. "Partial Symmetries of Weak Interactions".
In: *Nucl. Phys.* 22 (1961), p. 579.

[4] S. Weinberg. "A Model of Leptons". In: *Phys. Rev. Lett.* 19 (1967), p. 1264.

[5] A. Salam. "Elementary Particle Theory".
In: *Phys. Rev. Lett.* 19 (1967), p. 1264.

[6] ATLAS Collaboration. "Observation of a new particle in the search for the Standard Model Higgs boson with the ATLAS detector at the LHC".
In: *Phys. Lett. B* 716 (2012), p. 1. arXiv: 1207.7214 [hep-ex].

[7] CMS Collaboration. "Observation of a new boson with mass near 125 GeV in pp collisions at $\sqrt{s} = 7 and 8$ TeV". In: *JHEP* 06 (2013), p. 081.
arXiv: 1303.4571 [hep-ex].

[8] J. Ellis. "The Physics Landscape after the Higgs Discovery at the LHC".
In: *Nucl. Part. Phys. Proc.* 267-269 (2015), pp. 3–14.
arXiv: 1504.03654 [hep-ph].

[9] S. Martin. "A Supersymmetry Primer". In: ().
DOI: 10.1142/9789812839657_0001. arXiv: 9709356 [hep-ph].

[10] G. Polesello and D. Tovey.
"Constraining SUSY Dark Matter with the ATLAS detector at the LHC".
In: *JHEP* 05 (2004).

[11] ATLAS Collaboration.
"Search for the electroweak production of supersymmetric particles in $\sqrt{s} = 8$ TeV pp collisions with the ATLAS detector".
In: *Phys. Rev. D* 92 (2015), p. 012010. arXiv: 1504.03634 [hep-ex].

[12] ATLAS Collaboration. "Summary of the searches for squarks and gluinos using $\sqrt{s} = 8$ TeV pp collisions with the ATLAS experiment at the LHC". In: *JHEP* 10 (2015), p. 054. arXiv: 1507.05525 [hep-ex].

[13] M. Fairbairn, et al. "Stable massive particles at colliders". In: *Phys. Rept.* 438 (2007), pp. 1–63. DOI: 10.1016/j.physrep.2006.10.002. arXiv: 0611040 [hep-ph].

[14] D. Curtin, et al. "Exotic decays of the 125 GeV Higgs Boson". In: *Phys. Rev. D* 90 (2014). DOI: 10.1103/PhysRevD.90.075004. arXiv: 1312.4992 [hep-ph].

[15] D. Curtin, et al. "Illuminating dark photons with high-energy colliders". In: *J. High Energ. Phys.* 157 (2015). DOI: 10.1007/JHEP02(2015)157. arXiv: 1412.0018 [hep-ph].

[16] T. Han, Z. Si, K. M. Zurek, and M. J. Strassler. "Phenomenology of Hidden Valleys at Hadron Colliders". In: *JHEP* 07 (2008), p. 008. arXiv: 0712.2041 [hep-ph].

[17] J. Fan, M. Reece, and J. T. Ruderman. "Stealth Supersymmetry". In: *JHEP* 11 (2011), p. 012. arXiv: 1105.5135 [hep-ph].

[18] P. Meade, M. Reece, and D. Shih. "Long-lived neutralino NLSPs". In: *J. High Energ. Phys.* 67 (2010). DOI: 10.1007/JHEP10(2010)067. arXiv: 1006.4575 [hep-ph].

[19] R. Barbier, et al. "R-parity violating supersymmetry". In: *Phys. Rept.* 420 (2005), p. 1. arXiv: 0406039 [hep-ph].

[20] J. L. Hewett, B. Lillie, M. Masip, and T. G. Rizzo. "Signatures of long-lived gluinos in split supersymmetry". In: *JHEP* 09 (2004), p. 070. arXiv: 0408248 [hep-ph].

[21] ATLAS Collaboration. "Alignment Performance of the ATLAS Inner Detector Tracking System in 7 TeV proton–proton collisions at the LHC". In: (2010). URL: https://cds.cern.ch/record/1281342.

[22] ATLAS Collaboration. "Performance of primary vertex reconstruction in proton–proton collisions at $\sqrt{s} = 7$ TeV in the ATLAS experiment". In: (2010). URL: https://cds.cern.ch/record/1281344.

[23] ATLAS Collaboration. "Performance of the ATLAS Inner Detector Track and Vertex Reconstruction in High Pile-Up LHC Environment". In: (2012). URL: https://cds.cern.ch/record/1435196.

[24] ATLAS Collaboration. "Search for long-lived, weakly interacting particles that decay to displaced hadronic jets in proton-proton collisions at $\sqrt{s} = 8$ TeV with the ATLAS detector". In: *Phys. Rev. D* 92 (2015), p. 012010. arXiv: 1504.03634 [hep-ex].

[25] ATLAS Collaboration. "Search for massive, long-lived particles using multitrack displaced vertices or displaced lepton pairs in pp collisions at $\sqrt{s} = 8$ TeV with the ATLAS detector". In: *Phys. Rev. D* 92 (2015), p. 072004. arXiv: 1504.05162 [hep-ex].

[26] ATLAS Collaboration. "Search for long-lived neutral particles decaying into lepton jets in proton-proton collisions at $\sqrt{s} = 8$ TeV with the ATLAS detector". In: *JHEP* 11 (2014), p. 088. arXiv: 1409.0746 [hep-ex].

[27] ATLAS Collaboration. "Performance of the reconstruction of large impact parameter tracks in the inner detector of ATLAS". In: (2017). URL: http://cds.cern.ch/record/2275635.

[28] ATLAS Collaboration. "Performance of the ATLAS Trigger System in 2015". In: *Eur. Phys. J. C* 77 (2017), p. 317. DOI: 10.1140/epjc/s10052-017-4852-3. arXiv: 1611.09661 [hep-ex].

[29] F. Englert and R. Brout. "Broken symmetry and the mass of gauge vector mesons". In: *Phys. Rev. Lett.* 13 (1964), p. 321. DOI: 10.1103/PhysRevLett.13.321.

[30] P. Higgs. "Broken symmetries and the masses of gauge bosons". In: *Phys. Rev. Lett.* 13 (1964), p. 508. DOI: 10.1103/PhysRevLett.13.508.

[31] G. S. Guralnik, C. R. Hagen, and T. W. B. Kibble. "Global conservation laws and massless particles". In: *Phys. Rev. Lett.* 13 (1964), p. 585. DOI: 10.1103/PhysRevLett.13.585.

[32] S. Dawson. "Introduction to electroweak symmetry breaking". In: ().

[33] C. Englert, T. Plehn, D. Zerwas, and P. M. Zerwas. "Exploring the Higgs portal". In: *Phys. Lett. B* 703 (2011), pp. 298–305. DOI: 10.1016/j.physletb.2011.08.002. arXiv: 1106.3097 [hep-ph].

[34] K. A. Meissner, H. P. Nilles, M. Olechowski. "Supersymmetry breakdown at distant branes: the super Higgs mechanism". In: *Nucl. Phys. B* 561 (1999), pp. 30–42. DOI: 10.1016/S0550-3213(99)00552-0. arXiv: 9905139 [hep-th].

[35] L. Evans, P. Bryant. "LHC Machine". In: *JINST* 3 (2008), S08001. DOI: 10.1088/1748-0221/3/08/S08001.

[36] ATLAS Collaboration.
"ATLAS detector and physics performance: Technical Design Report, 1".
In: Technical Design Report ATLAS (1999).
URL: https://cds.cern.ch/record/391176.

[37] ATLAS Collaboration.
"Studies of the performance of the ATLAS detector using cosmic-ray muons".
In: *Eur. Phys. J. C* 71 (2011), p. 1593.
DOI: 10.1140/epjc/s10052-011-1593-6. arXiv: 1011.6665 [hep-ex].

[38] ATLAS Collaboration.
"The ATLAS Inner Detector commissioning and calibration".
In: *Eur. Phys. J. C* 70 (2010), p. 787.
DOI: 10.1140/epjc/s10052-010-1366-7. arXiv: 1004.5293 [hep-ex].

[39] ATLAS Collaboration.
"Performance of the ATLAS detector using first collision data".
In: *JHEP* 09 (2010), p. 056. DOI: 10.1007/JHEP09(2010)056.
arXiv: 1005.5254 [hep-ex].

[40] ATLAS Collaboration. "ATLAS inner detector: Technical Design Report, 1".
In: Technical Design Report ATLAS (1997).
URL: https://cds.cern.ch/record/331063.

[41] ATLAS Collaboration. "ATLAS inner detector: Technical Design Report, 2".
In: Technical Design Report ATLAS (1997).
URL: https://cds.cern.ch/record/331064.

[42] ATLAS Collaboration. "ATLAS central solenoid: Technical Design Report".
In: Technical Design Report ATLAS (1997).
URL: https://cds.cern.ch/record/331067.

[43] ATLAS Collaboration. "ATLAS pixel detector: Technical Design Report".
In: Technical Design Report ATLAS (1998).
URL: https://cds.cern.ch/record/381263.

[44] ATLAS Collaboration. "ATLAS pixel detector electronics and sensors".
In: *JINST* 3 (2008), P07007. DOI: 10.1088/1748-0221/3/07/P07007.

[45] ATLAS Collaboration.
"The ATLAS insertable B-layer: from construction to operation".
In: *JINST* 11 (2016), p. C12036. arXiv: 1610.01994 [physics.ins-det].

[46] ATLAS Collaboration. “Silicon microstrip detectors for the ATLAS SCT”. In: *Nucl. Instrum. Meth.* A485 (2002), pp. 84–88.

[47] ATLAS Collaboration. “The ATLAS semiconductor tracker end-cap module”. In: *Nucl. Instrum. Meth.* A575 (2007), pp. 353–389.

[48] ATLAS Collaboration. “The silicon microstrip sensors of the ATLAS semiconductor tracker”. In: *Nucl. Instrum. Meth.* A578 (2007), pp. 98–118.

[49] ATLAS TRT Collaboration. “The ATLAS TRT barrel detector”. In: *JINST* 3 (2008), P02014.

[50] ATLAS TRT Collaboration. “The ATLAS TRT end-cap detectors”. In: *JINST* 3 (2008), P10003.

[51] ATLAS TRT Collaboration. “The ATLAS Transition Radiation Tracker (TRT) proportional drift tube: design and performance”. In: *JINST* 3 (2008), P02013.

[52] ATLAS Collaboration. “ATLAS calorimeter performance: Technical Design Report”. In: Technical Design Report ATLAS (1996). URL: https://cds.cern.ch/record/331059.

[53] ATLAS Collaboration. “ATLAS liquid-argon calorimeter: Technical Design Report”. In: Technical Design Report ATLAS (1996). URL: https://cds.cern.ch/record/331061.

[54] ATLAS Collaboration. “ATLAS tile calorimeter: Technical Design Report”. In: Technical Design Report ATLAS (1996). URL: https://cds.cern.ch/record/331062.

[55] ATLAS Collaboration. “ATLAS muon spectrometer: Technical Design Report”. In: Technical Design Report ATLAS (1997). URL: https://cds.cern.ch/record/331068.

[56] ATLAS Collaboration. “ATLAS barrel toroid: Technical Design Report”. In: Technical Design Report ATLAS (1997). URL: https://cds.cern.ch/record/331065.

[57] ATLAS Collaboration. “ATLAS end-cap toroids: Technical Design Report”. In: Technical Design Report ATLAS (1997).
URL: https://cds.cern.ch/record/331066.

[58] F. Bauer, et al. “Construction and test of MDT chambers for the ATLAS muon spectrometer”. In: *Nucl. Instrum. Meth.* A461 (2001), pp. 17–20.

[59] T. Argyropoulos, et al. “Cathode strip chambers in ATLAS: installation, commissioning and in-situ performance”.
In: *IEEE Trans. Nucl. Sci.* 56 (2009), pp. 1568–1574.

[60] G. Aielli, et al.
“The RPC first level muon trigger in the barrel of the ATLAS experiment”.
In: *Nucl. Phys. Proc. Suppl.* 158 (2006), pp. 11–15.

[61] S. Majewski, et al.
“A thin multiwire chamber operating in the high multiplication mode”.
In: *Nucl. Instrum. Meth.* 217 (1983), pp. 265–271.

[62] ATLAS Collaboration. “ATLAS high-level trigger, data-acquisition and controls: Technical Design Report”.
In: Technical Design Report ATLAS (2003).
URL: https://cds.cern.ch/record/616089.

[63] ATLAS Collaboration. “Luminosity Determination in pp Collisions at $\sqrt{s} = 8$ TeV using the ATLAS Detector at the LHC”.
In: *Eur. Phys. J. C* 76 (2016), p. 653.
DOI: 10.1140/epjc/s10052-016-4466-1. arXiv: 1608.03953 [hep-ex].

[64] ATLAS Collaboration. “The ATLAS simulation infrastructure”.
In: *Eur. Phys. J. C* 70 (2010), pp. 823–874.
arXiv: 1005.4568 [physics.ins-det].

[65] S. Agostinelli, et al. “GEANT4: A simulation toolkit”.
In: *Nucl. Instrum. Meth.* A506 (2003), p. 250.

[66] T. Sjöstrand, et al. “An Introduction to PYTHIA 8.2”.
In: *Comput. Phys. Commun.* 191 (2015), p. 159.
DOI: 10.1016/j.cpc.2015.01.024. arXiv: 1410.3012 [hep-ph].

[67] “Summary of ATLAS Pythia 8 tunes”. In: ATL-PHYS-PUB-2012-003 (2012).
URL: https://cds.cern.ch/record/1474107.

[68] A. D. Martin, W. J. Stirling, R. S. Thorne, and G. Watt.
"Parton distributions for the LHC".
In: *Eur. Phys. J.* C63 (2009), pp. 189–285. arXiv: 0901.0002 [hep-ph].

[69] J. Alwall, et al.
"The automated computation of tree-level and next-to-leading order differential cross sections, and their matching to parton shower simulations".
In: *JHEP* 07 (2014), p. 079. DOI: 10.1007/JHEP07(2014)079.
arXiv: 1405.0301 [hep-ph].

[70] D. J. Lange. "The EvtGen particle decay simulation package".
In: *Nucl. Instrum. Meth. A* 462 (2001), p. 152.
DOI: 10.1016/S0168-9002(01)00089-4.

[71] P. N. S. Frixione and C. Oleari. "Matching NLO QCD computations with Parton Shower simulations: the POWHEG method".
In: *JHEP* 11 (2007), p. 070. DOI: 10.1088/1126-6708/2007/11/070.
arXiv: 0709.2092 [hep-ph].

[72] e. a. T. Gleisberg. "Event generation with SHERPA 1.1".
In: *JHEP* 02 (2009), p. 007. DOI: 10.1088/1126-6708/2009/02/007.
arXiv: 0811.4622 [hep-ph].

[73] T. Sjöstrand. "PYTHIA 6.4 Physics and Manual".
In: *JHEP* 05 (2006), p. 026. DOI: 10.1088/1126-6708/2006/05/026.
arXiv: hep-ph/0603175.

[74] S. Todorova, et al. "The ATLAS tracking geometry description".
In: ATL-SOFT-PUB-2007-004 (2007).
URL: https://cds.cern.ch/record/1038098.

[75] E. Lund, et al. "Track parameter propagation through the application of a new adaptive Runge-Kutta-Nystrom method in the ATLAS experiment".
In: ATL-SOFT-PUB-2009-001 (2009).
URL: https://cds.cern.ch/record/1113528.

[76] R. Fruhwirth, et al.
"Application of Kalman Filtering to track and vertex fitting".
In: *Nucl. Instrum. Meth.* A262 (1987), p. 444.

[77] T. G. Cornelissen, et al. "The global χ^2 track fitter in ATLAS".
In: *J. Phys. Conf. Ser.* 119 (2007).

[78] ATLAS Collaboration. "Early Inner Detector tracking performance in the 2015 data at $\sqrt{s} = 13$ TeV". In: ATL-PHYS-PUB-2015-051 (2015). URL: https://cds.cern.ch/record/2110140.

[79] A. Salzburger, et al. "The ATLAS track extrapolation package". In: ATL-SOFT-PUB-2007-005 (2007). URL: https://cds.cern.ch/record/1038100.

[80] ATLAS Collaboration. "Muon identification algorithms in ATLAS". In: *PoS EPS-HEP* (2009), p. 431.

[81] ATLAS Collaboration. "A muon identification and combined reconstruction procedure for the ATLAS detector at the LHC using the (MUONBOY, STACO, MuTag) reconstruction packages". In: *Nucl. Instrum. Meth.* A572 (2007), pp. 77–79.

[82] ATLAS Collaboration. "Muon reconstruction performance of the ATLAS detector in proton-proton collision data at $\sqrt{s} = 13$ TeV". In: *Eur. Phys. J. C* 76 (2016), p. 292. DOI: 10.1140/epjc/s10052-016-4120-y. arXiv: 1603.05598 [hep-ex].

[83] M. Cacciari, G. P. Salam, and G. Soyez. "The anti-k(t) jet clustering algorithm". In: *JHEP* 04 (2008), p. 063. arXiv: 0802.1189 [hep-ph].

[84] ATLAS Collaboration. "The Run-2 ATLAS Trigger System". In: ATL-DAQ-PROC-2016-003 (2016).

[85] ATLAS Collaboration. "Characterisation and mitigation of beam-induced backgrounds observed in the ATLAS detector during the 2011 proton-proton run". In: *JINST* 8 (2013), P07004. arXiv: 1303.0223 [hep-ex].

[86] M. Aaboud, et al. "Measurement of the Inelastic Proton-Proton Cross Section at $\sqrt{s} = 13$ TeV with the ATLAS Detector at the LHC". In: *Phys. Rev. Lett.* 117.18 (2016), p. 182002. DOI: 10.1103/PhysRevLett.117.182002. arXiv: 1606.02625 [hep-ex].

[87] A. L. Read. "Modified frequentist analysis of search results (the CL_s method". In: *1st Wkshop on Conf. Lim.* 005 (2000), pp. 81–101. DOI: 10.5170/CERN-2000-005.81.

[88] E. Gross. "LHC statistics for pedestrians". In: *PHYSTAT-LHC proc.* 27 (2008), p. 218.

[89] W. A. Rolke, et al.
"Limits and confidence intervals in the presence of nuisance parameters".
In: *Nucl. Instrum. Meth.* A551 (2005), pp. 493–503.
DOI: 10.1016/j.nima.2005.05.068. arXiv: 0403059 [physics.data-an].

[90] R. A. Fisher. "Theory of statistical estimation".
In: *Proc. Camb. Phil. Soc.* 22 (1925), pp. 710–711.

[91] ATLAS Collaboration. "COnstraints on new phenomena via Higgs boson couplings and invisible decays with the ATLAS detector".
In: *JHEP* 11 (2015), p. 206. DOI: 10.1007/JHEP11(2015)206.
arXiv: 1509.00672 [hep-ex].

[92] CMS Collaboration. "Searches for invisible decays of the Higgs boson in pp collisions at $\sqrt{s} = 7, 8$, and 13 TeV". In: *JHEP* 02 (2017), p. 135.
DOI: 10.1007/JHEP02(2017)135. arXiv: 1610.09218 [hep-ex].